

¹ A Search in the Two-Photon Final State for
² Evidence of New Particle Production in pp
³ Collisions at $\sqrt{s} = 7$ TeV

⁴ Rachel P. Yohay
University of Virginia
`rpy3y@virginia.edu`

⁵ June 5, 2012

Contents

7	1	The Supersymmetric Extension to the Standard Model	3
8	1.1	Supermultiplet Representation	3
9	1.2	The Unbroken SUSY Lagrangian	4
10	1.3	Soft SUSY Breaking	10
11	1.4	Gauge-Mediated SUSY Breaking	12
12	1.5	Phenomenology of General Gauge Mediation	15
13	1.6	Experimental Status of SUSY	19
14	2	The Compact Muon Solenoid Experiment	23
15	2.1	The Detectors and Their Operating Principles	27
16	2.1.1	Tracking System	27
17	2.1.2	Electromagnetic Calorimeter	36
18	2.1.3	Hadronic Calorimeter	41
19	2.1.4	Muon System	45
20	2.2	Triggering, Data Acquisition, and Data Transfer	50
21	2.2.1	Level 1 and High Level Trigger Systems	50
22	2.2.2	Data Acquisition System	54
23	2.2.3	Data Processing and Transfer to Computing Centers	57
24	3	Event Selection	60
25	3.1	Object Reconstruction	61

26	3.1.1	Photons	61
27	3.1.2	Electrons	72
28	3.1.3	Jets and Missing Transverse Energy	72
29	3.2	HLT	78
30	3.3	Event Quality	81
31	3.4	Photon Identification Efficiency	84
32	3.4.1	Tag and Probe Method	85
33	3.4.2	Photon Efficiency Scale Factor $\epsilon_e^{\text{data}}/\epsilon_e^{\text{MC}}$	88
34	4	Data Analysis	93
35	4.1	Modeling the QCD Background	97
36	4.1.1	Outline of the Procedure	97
37	4.1.2	Reweighting	98
38	4.1.3	Normalization	109
39	4.2	Modeling the Electroweak Background	109
40	4.3	Errors on the Background Prediction	115
41	4.4	Results	121
42	5	Interpretation of Results in Terms of GMSB Models	127
43	5.1	Simplified Models	127
44	5.2	Upper Limit Calculation and Model Exclusion	129
45	5.2.1	Signal Acceptance \times Efficiency	129
46	5.2.2	CL_s and the Profile Likelihood Test Statistic	133
47	5.3	Cross Section Upper Limits	140
48	5.4	Exclusion Contours	141
49	A	Monte Carlo Samples	146
50	A.0.1	List of Samples	146
51	A.0.2	Explanation of Naming Conventions	147

⁵² **Chapter 1**

⁵³ **The Supersymmetric Extension to
⁵⁴ the Standard Model**

⁵⁵ The following introduction to SUSY focuses primarily on the aspects of the formalism that are relevant to phenomenology. In particular, most of the details of SUSY breaking (about which there is little theoretical consensus) are omitted, except where they are relevant to experiment. The notation is similar to that used in refs. [5] and [6], and much of the information presented is culled from those references.

⁶⁰ **1.1 Supermultiplet Representation**

⁶¹ The Standard Model is extended to include supersymmetry by the introduction of a supersymmetry transformation that takes fermionic states to bosonic states and vice versa. The resulting model is called the *minimal supersymmetric Standard Model* (MSSM). In analogy with the known symmetries of the Standard Model, the SUSY transformation has associated generators that obey defining commutation and anti-commutation relations, and a fundamental representation. All SM particles and their superpartners fall into one of two *supermultiplet* representations. Using the property that

$$n_F = n_B, \quad (1.1)$$

69 where n_F is the number of fermionic degrees of freedom per supermultiplet and n_B is
 70 the number of bosonic degrees of freedom, the two types of supermultiplets are

- 71 1. *Chiral supermultiplets*: one Weyl fermion (two helicity states $\Rightarrow n_F = 2$) and
 72 one complex scalar field (with two real components $\Rightarrow n_B = 2$)

 73 2. *Gauge supermultiplets*: One spin-1 vector boson (two helicity states $\Rightarrow n_B = 2$)
 74 and one Weyl fermion (two helicity states $\Rightarrow n_F = 2$)

75 In the gauge supermultiplet, the vector boson is assumed massless (i.e. before
 76 EWSB generates a mass for it). Since the superpartners to the SM particles have not
 77 yet been discovered, they must be significantly heavier than their SM counterparts.
 78 Unbroken SUSY predicts that the SM particles and their superpartners must have
 79 exactly the same mass, so ultimately a mechanism for SUSY breaking must be intro-
 80 duced to generate masses for the superpartners (see Sec. 1.3). Tables 1.1 and 1.2 show
 81 the chiral and gauge supermultiplets of the MSSM, respectively. Note that the scalar
 82 partners to the SM fermions are denoted by placing an “s” in front of their names,
 83 while the chiral fermion partners to the SM gauge bosons are denoted by appending
 84 “ino” to their names.

85 1.2 The Unbroken SUSY Lagrangian

86 The first piece of the full unbroken SUSY Lagrangian density consists of the kinetic
 87 and interacting terms related to the chiral supermultiplets. As explained in Sec. 1.1,
 88 a chiral supermultiplet consists of a Weyl fermion ψ (the ordinary fermion) and a
 89 complex scalar ϕ (the sfermion). For a collection of such chiral supermultiplets, the
 90 Lagrangian is

Table 1.1: Chiral supermultiplets of the supersymmetric Standard Model. Adapted from Table 1.1 of ref. [6].

Type of supermultiplet	Notation	Spin-0 component	Spin-1/2 component	Representation under $SU(3)_C \otimes SU(2)_L \otimes U(1)_Y$
Left-handed quark/squark doublet ($\times 3$ families)	Q	$(\tilde{u}_L \tilde{d}_L)$	$(u_L d_L)$	$(\mathbf{3}, \mathbf{2}, \frac{1}{6})$
Right-handed up-type quark/squark singlet ($\times 3$ families)	\bar{u}	\tilde{u}_R^*	u_R^\dagger	$(\bar{\mathbf{3}}, \mathbf{1}, -\frac{2}{3})$
Right-handed down-type quark/squark singlet ($\times 3$ families)	\bar{d}	\tilde{d}_R^*	d_R^\dagger	$(\bar{\mathbf{3}}, \mathbf{1}, \frac{1}{3})$
Left-handed lepton/slepton doublet ($\times 3$ families)	L	$(\tilde{\nu}_{eL} \tilde{e}_L)$	$(\bar{\nu}_{eL} e_L)$	$(\mathbf{1}, \mathbf{2}, -\frac{1}{2})$
Right-handed lepton/slepton singlet ($\times 3$ families)	\bar{e}	\tilde{e}_R^*	e_R^\dagger	$(\bar{\mathbf{1}}, \mathbf{1}, 1)$
Up-type Higgs/Higgsino doublet	H_u	$(H_u^+ H_u^0)$	$(\tilde{H}_u^+ \tilde{H}_u^0)$	$(\mathbf{1}, \mathbf{2}, \frac{1}{2})$
Down-type Higgs/Higgsino doublet	H_d	$(H_d^0 H_d^-)$	$(\tilde{H}_d^0 \tilde{H}_d^-)$	$(\mathbf{1}, \mathbf{2}, -\frac{1}{2})$

Table 1.2: Gauge supermultiplets of the supersymmetric Standard Model. Adapted from Table 1.2 of ref. [6].

Type of supermultiplet	Spin-1/2 component	Spin-1 component	Representation under $SU(3)_C \otimes SU(2)_L \otimes U(1)_Y$
Gluon/gluino	\tilde{g}	g	$(\mathbf{8}, \mathbf{1}, 0)$
W/wino	$\tilde{W}^\pm \tilde{W}^0$	$W^\pm W^0$	$(\mathbf{1}, \mathbf{3}, 0)$
B/bino	\tilde{B}^0	B^0	$(\mathbf{1}, \mathbf{1}, 0)$

$$\begin{aligned}\mathcal{L}_{\text{chiral}} = & -\partial^\mu \phi^{*i} \partial_\mu \phi_i - V_{\text{chiral}}(\phi, \phi^*) - i\psi^{\dagger i} \bar{\sigma}^\mu \partial_\mu \psi_i - \frac{1}{2} M^{ij} \psi_i \psi_j \\ & - \frac{1}{2} M_{ij}^* \psi^{\dagger i} \psi^{\dagger j} - \frac{1}{2} y^{ijk} \phi_i \psi_j \psi_k - \frac{1}{2} y_{ijk}^* \phi^{*i} \psi^{\dagger j} \psi^{\dagger k}\end{aligned}\quad (1.2)$$

where i runs over all supermultiplets in Table 1.1, $\bar{\sigma}^\mu$ are $-1 \times$ the Pauli matrices (except for $\sigma^0 = \bar{\sigma}^0$), M^{ij} is a mass matrix for the fermions, y^{ijk} are the Yukawa couplings between one scalar and two spinor fields, and $V_{\text{chiral}}(\phi, \phi^*)$ is the scalar potential

$$\begin{aligned}V_{\text{chiral}}(\phi, \phi^*) = & M_{ik}^* M^{kj} \phi^{*i} \phi_j + \frac{1}{2} M^{in} y_{jkn}^* \phi_i \phi^{*j} \phi^{*k} \\ & + \frac{1}{2} M_{in}^* y^{jkn} \phi^{*i} \phi_j \phi_k + \frac{1}{4} y^{ijn} y_{klm}^* \phi_i \phi_j \phi^{*k} \phi^{*l}.\end{aligned}\quad (1.3)$$

The Lagrangian can also be written as the kinetic terms plus derivatives of the *superpotential* W :

$$\begin{aligned}\mathcal{L}_{\text{chiral}} = & -\partial^\mu \phi^{*i} \partial_\mu \phi_i - i\psi^{\dagger i} \bar{\sigma}^\mu \partial_\mu \psi_i \\ & - \frac{1}{2} \left(\frac{\delta^2 W}{\delta \phi^i \delta \phi^j} \psi_i \psi_j + \frac{\delta^2 W^*}{\delta \phi_i \delta \phi_j} \psi^{\dagger i} \psi^{\dagger j} \right) - \frac{\delta W}{\delta \phi^i} \frac{\delta W^*}{\delta \phi_i}\end{aligned}\quad (1.4)$$

where

$$W = M^{ij} \phi_i \phi_j + \frac{1}{6} y^{ijk} \phi_i \phi_j \phi_k. \quad (1.5)$$

The second part of the Lagrangian involves the gauge supermultiplets. In terms of the spin-1 ordinary gauge boson A_μ^a and the spin-1/2 Weyl spinor gaugino λ^a of

¹⁰⁰ the gauge supermultiplet, where a runs over the number of generators for the SM
¹⁰¹ subgroup (i.e. 1-8 for $SU(3)_C$, 1-3 for $SU(2)_L$, and 1 for $U(1)_Y$), this part of the
¹⁰² Lagrangian is

$$\mathcal{L}_{\text{gauge}} = -\frac{1}{4}F_{\mu\nu}^a F^{\mu\nu a} - i\lambda^{\dagger a}\bar{\sigma}^\mu D_\mu \lambda^a + \frac{1}{2}D^a D^a \quad (1.6)$$

¹⁰³ where

$$F_{\mu\nu}^a = \partial_\mu A_\nu^a - \partial_\nu A_\mu^a + g f^{abc} A_\mu^b A_\nu^c \quad (1.7)$$

¹⁰⁴ (g is the coupling constant and f^{abc} are the structure constants for the particular SM
¹⁰⁵ gauge group),

$$D_\mu \lambda^a = \partial_\mu \lambda^a + g f^{abc} A_\mu^b \lambda^c, \quad (1.8)$$

¹⁰⁶ and D^a is an auxiliary field that does not propagate (in the literature, it is used as a
¹⁰⁷ bookkeeping tool and can be removed via its algebraic equation of motion).

¹⁰⁸ To build a fully supersymmetric and gauge-invariant Lagrangian, the ordinary
¹⁰⁹ derivatives in $\mathcal{L}_{\text{chiral}}$ (Eq. 1.2) must be replaced by covariant derivatives

$$D_\mu \phi_i = \partial_\mu \phi_i - ig A_\mu^a (T^a \phi)_i \quad (1.9)$$

$$D_\mu \phi^{*i} = \partial_\mu \phi^{*i} + ig A_\mu^a (\phi^* T^a)^i \quad (1.10)$$

$$D_\mu \psi_i = \partial_\mu \psi_i - ig A_\mu^a (T^a \psi)_i. \quad (1.11)$$

¹¹⁰ This leads to the full Lagrangian

$$\begin{aligned}
\mathcal{L} &= \mathcal{L}_{\text{chiral}} + \mathcal{L}_{\text{gauge}} \\
&\quad - \sqrt{2}g(\phi^{*i}T^a\psi_i)\lambda^a - \sqrt{2}g\lambda^{\dagger a}(\psi^{\dagger i}T^a\phi_i) + g(\phi^{*i}T^a\phi_i)D^a \\
&= -\partial^\mu\phi^{*i}\partial_\mu\phi_i - i\psi^{\dagger i}\bar{\sigma}^\mu\partial_\mu\psi_i + ig\partial^\mu\phi^{*i}A_\mu^a(T^a\phi)_i - ig\partial_\mu\phi_iA^{\mu a}(\phi^*T^a)^i \\
&\quad - g^2A^{\mu a}(\phi^*T^a)^iA_\mu^a(T^a\phi)_i - g\psi^{\dagger i}\bar{\sigma}^\mu A_\mu^a(T^a\psi)_i - V_{\text{chiral}}(\phi, \phi^*) \\
&\quad - \frac{1}{2}M^{ij}\psi_i\psi_j - \frac{1}{2}M_{ij}^*\psi^{\dagger i}\psi^{\dagger j} - \frac{1}{2}y^{ijk}\phi_i\psi_j\psi_k - \frac{1}{2}y_{ijk}^*\phi^{*i}\psi^{\dagger j}\psi^{\dagger k} \\
&\quad - \frac{1}{4}F_{\mu\nu}^aF^{\mu\nu a} - i\lambda^{\dagger a}\bar{\sigma}^\mu\partial_\mu\lambda^a - ig\lambda^{\dagger a}\bar{\sigma}^\mu f^{abc}A_\mu^b\lambda^c + \frac{1}{2}D^aD^a \\
&\quad - \sqrt{2}g(\phi^{*i}T^a\psi_i)\lambda^a - \sqrt{2}g\lambda^{\dagger a}(\psi^{\dagger i}T^a\phi_i) + g(\phi^{*i}T^a\phi_i)D^a. \tag{1.12}
\end{aligned}$$

¹¹¹ Writing out $F_{\mu\nu}^a$ and $V_{\text{chiral}}(\phi, \phi^*)$ explicitly combining the D^a terms using the equation

¹¹² of motion $D^a = -g\phi^{*i}T^a\phi_i$, and rearranging some terms, the final unbroken SUSY

¹¹³ Lagrangian is

$$\begin{aligned}
\mathcal{L} = & -\partial^\mu \phi^{*i} \partial_\mu \phi_i - i\psi^{\dagger i} \bar{\sigma}^\mu \partial_\mu \psi_i \\
& - \frac{1}{4} (\partial_\mu A_\nu^a - \partial_\nu A_\mu^a) (\partial^\mu A^{\nu a} - \partial^\nu A^{\mu a}) - i\lambda^{\dagger a} \bar{\sigma}^\mu \partial_\mu \lambda^a \\
& - M_{ik}^* M^{kj} \phi^{*i} \phi_j - \frac{1}{2} M^{ij} \psi_i \psi_j - \frac{1}{2} M_{ij}^* \psi^{\dagger i} \psi^{\dagger j} \\
& + ig \partial^\mu \phi^{*i} A_\mu^a (T^a \phi)_i - ig \partial_\mu \phi_i A^{\mu a} (\phi^* T^a)^i - g \psi^{\dagger i} \bar{\sigma}^\mu A_\mu^a (T^a \psi)_i \\
& - ig \lambda^{\dagger a} \bar{\sigma}^\mu f^{abc} A_\mu^b \lambda^c \\
& - \frac{1}{4} g f^{abc} [(\partial_\mu A_\nu^a - \partial_\nu A_\mu^a) A^{\mu b} A^{\nu c} + A_\mu^b A_\nu^c (\partial^\mu A^{\nu a} - \partial^\nu A^{\mu a})] \\
& - \frac{1}{2} M_{in}^* y^{jkn} \phi^{*i} \phi_j \phi_k - \frac{1}{2} M^{in} y_{jkn}^* \phi_i \phi^{*j} \phi^{*k} \\
& - \frac{1}{2} y^{ijk} \phi_i \psi_j \psi_k - \frac{1}{2} y_{ijk}^* \phi^{*i} \psi^{\dagger j} \psi^{\dagger k} \\
& - \sqrt{2} g (\phi^{*i} T^a \psi_i) \lambda^a - \sqrt{2} g \lambda^{\dagger a} (\psi^{\dagger i} T^a \phi_i) \\
& - g^2 A^{\mu a} (\phi^* T^a)^i A_\mu^a (T^a \phi)_i - \frac{1}{4} g^2 f^{abc} A_\mu^b A_\nu^c f^{abc} A^{\mu b} A^{\nu c} \\
& - \frac{1}{4} y^{ijn} y_{kln}^* \phi_i \phi_j \phi^{*k} \phi^{*l} - \frac{1}{2} g^2 (\phi^{*i} T^a \phi_i)^2.
\end{aligned} \tag{1.13}$$

¹¹⁴ The above Lagrangian applies to chiral supermultiplets interacting with one kind
¹¹⁵ of gauge supermultiplet (i.e. one SM gauge group). In the general case, there are
¹¹⁶ additional terms corresponding to interactions with all three SM gauge groups.

¹¹⁷ The following list gives a description of the terms in Eq. 1.13:

- ¹¹⁸ • First two lines: kinetic terms for the four types of fields ϕ_i , ψ_i , A_μ^a , and λ^a
- ¹¹⁹ • Third line: mass terms for the ϕ_i and ψ_i (see Figs. 1.1(a) and 1.1(b))
- ¹²⁰ • Fourth and fifth lines: cubic couplings in which ϕ_i , ψ_i , or λ^a radiates an A_μ^a (see
¹²¹ Figs. 1.1(c), 1.1(d), and 1.1(e))
- ¹²² • Sixth line: triple gauge boson couplings (see Fig. 1.1(f))
- ¹²³ • Seventh line: triple sfermion couplings (see Fig. 1.1(g))

- ¹²⁴ • Eighth line: cubic couplings in which ψ_i radiates a ϕ_i (see Fig. 1.1(h))
- ¹²⁵ • Ninth line: ϕ_i - ψ_i - λ^a vertices (see Fig. 1.1(i))
- ¹²⁶ • 10th line: A_μ^a - A_μ^a - ϕ_i - ϕ_i and quadruple gauge boson couplings (see Figs. 1.1(j)
¹²⁷ and 1.1(k))
- ¹²⁸ • 11th line: ϕ_i^4 vertices (see Figs. 1.1(l) and 1.1(m))

¹²⁹ 1.3 Soft SUSY Breaking

¹³⁰ Since quadratic divergences in sfermion masses vanish to all orders in perturbation
¹³¹ theory in plain unbroken SUSY [6] due to the presence of gauge and Yukawa interac-
¹³² tions with the necessary relationships between coupling constants, it is desirable that
¹³³ the terms that break SUSY not disturb this property. In addition, SUSY should be
¹³⁴ broken spontaneously, as electroweak symmetry is broken in the Standard Model, so
¹³⁵ that it is only made manifest at high energies. To satisfy these constraints, SUSY-
¹³⁶ breaking terms are simply added to the unbroken SUSY Lagrangian in Eq. 1.13 such
¹³⁷ that $\mathcal{L}_{\text{total}} = \mathcal{L}_{\text{unbroken}} + \mathcal{L}_{\text{breaking}}$. The coefficients of terms in $\mathcal{L}_{\text{breaking}}$ must have
¹³⁸ positive mass dimension in order not to contribute quadratically divergent loop cor-
¹³⁹ rections to the scalar masses (like the Higgs mass).¹ This form of SUSY breaking is
¹⁴⁰ called *soft*, and all coefficients of soft SUSY breaking terms are expected to be of
¹⁴¹ order m_{soft} or m_{soft}^2 .

¹This point can be argued via dimensional analysis. Radiative corrections take the form Δm_S^2 , where m_S is the mass of the scalar particle in question. The dimensions of Δm_S^2 are mass². Δm_S^2 is proportional to some coupling constant or mass coefficient k multiplied by a function of Λ_{UV} , the high energy cutoff scale. The function of Λ_{UV} is determined by a loop integral, and thus typically takes the form Λ_{UV}^2 (quadratically divergent) or $\ln \frac{\Lambda_{\text{UV}}}{m_{\text{low}}}$ (logarithmically divergent, where m_{low} is some other lower-mass scale in the problem). Now, if k already contributes at least one power of mass to Δm_S^2 , then the high-energy behavior—the function of Λ_{UV} —can only contribute at most one power of the dimensionful parameter Λ_{UV} . However, there are typically no loop integrals that diverge linearly in Λ_{UV} , so by forcing k to have positive mass dimension, the form of the radiative corrections contributed by SUSY-breaking terms is limited to $\Delta m_S^2 \sim m_{\text{low}}^2 \ln \frac{\Lambda_{\text{UV}}}{m_{\text{low}}}$. In effect, the possibility of dangerous corrections proportional to Λ_{UV}^2 is excluded by dimensional analysis if the requirement that k contribute at least one power of mass is enforced.

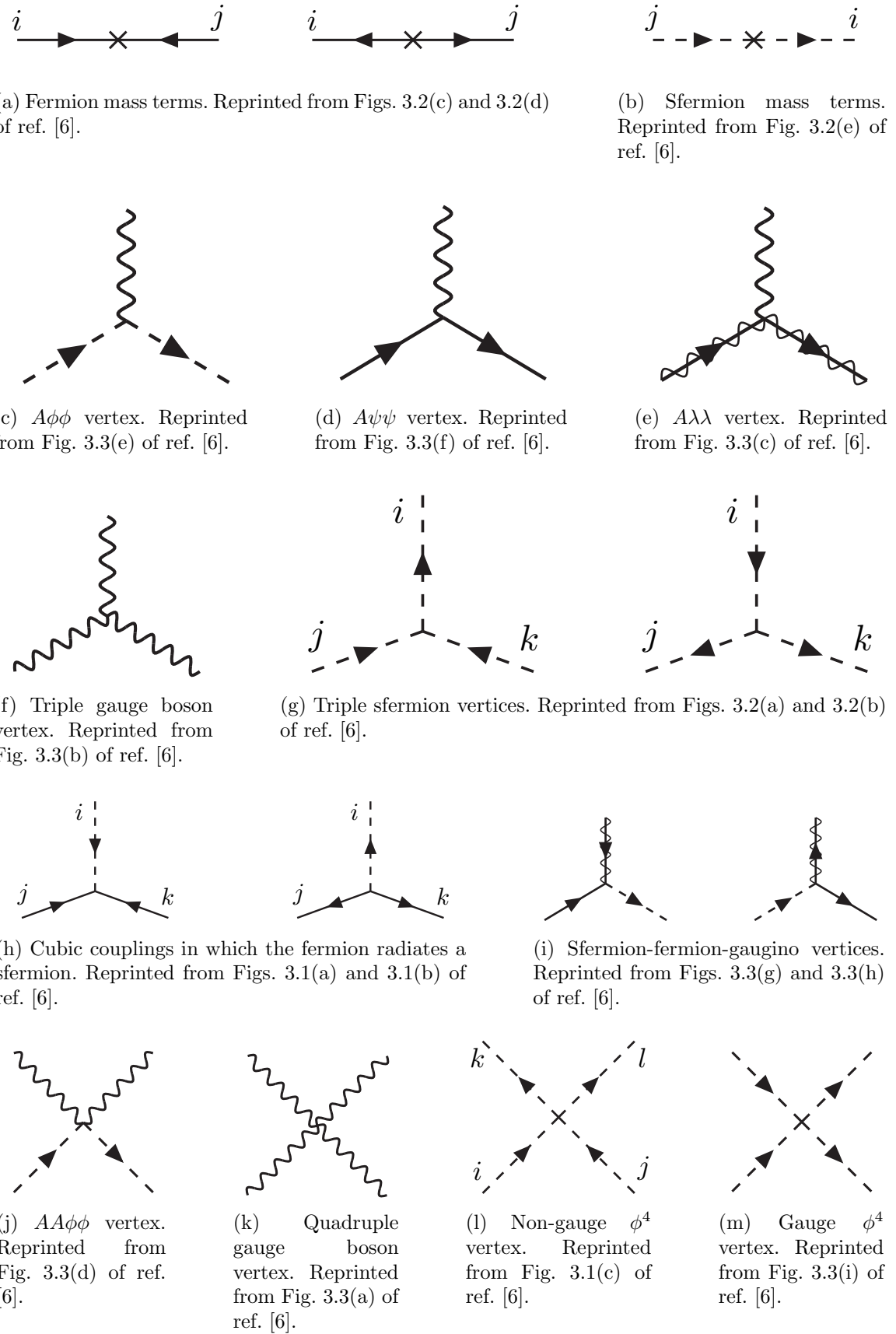


Figure 1.1: Interactions in the unbroken SUSY Lagrangian.

¹⁴² Soft SUSY breaking terms give masses to the sfermions and gauginos and introduce
¹⁴³ a cubic sfermion vertex. The soft terms are given by

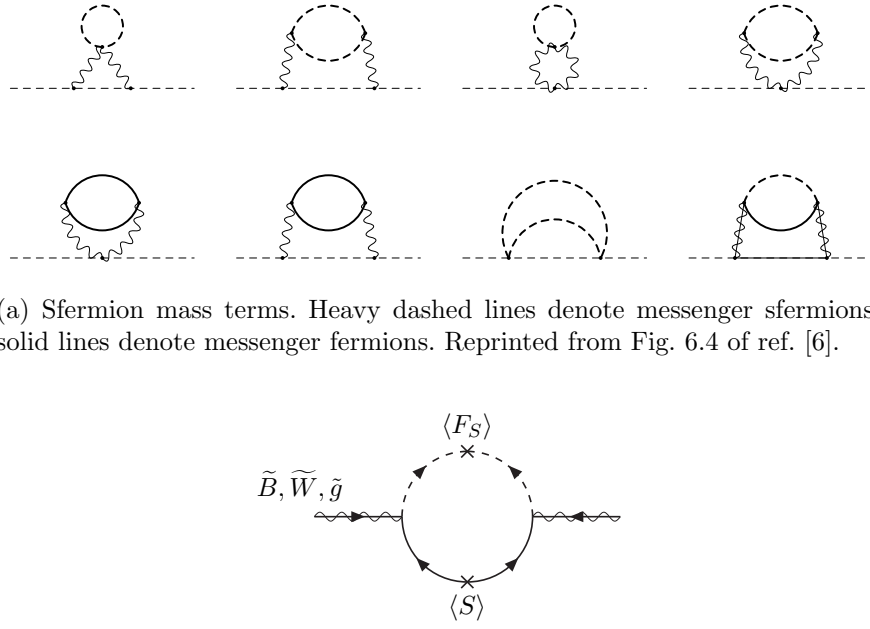
$$\begin{aligned}
\mathcal{L}_{\text{soft}} = & -\frac{1}{2}(M_3 \tilde{g}^a \tilde{g}^a + M_2 \tilde{W}^a \tilde{W}^a + M_1 \tilde{B} \tilde{B} + \text{h.c.}) \\
& - (a_u^{ij} \tilde{u}_{Ri}^* \tilde{Q}_j H_u - a_d^{ij} \tilde{d}_{Ri}^* \tilde{Q}_j H_d - a_e^{ij} \tilde{e}_{Ri}^* \tilde{L}_j H_d + \text{h.c.}) \\
& - m_{\tilde{Q}_{ij}}^2 \tilde{Q}_i^\dagger \tilde{Q}_j - m_{\tilde{L}_{ij}}^2 \tilde{L}_i^\dagger \tilde{L}_j \\
& - m_{\tilde{u}_{ij}}^2 \tilde{u}_{Ri} \tilde{u}_{Rj}^* - m_{\tilde{d}_{ij}}^2 \tilde{d}_{Ri} \tilde{d}_{Rj}^* - m_{\tilde{e}_{ij}}^2 \tilde{e}_{Ri} \tilde{e}_{Rj}^* \\
& - m_{H_u}^2 H_u^* H_u - m_{H_d}^2 H_d^* H_d - (b H_u H_d + \text{h.c.})
\end{aligned} \tag{1.14}$$

¹⁴⁴ where a runs from 1-8 for \tilde{g}^a and from 1-3 for \tilde{W}^a , and i, j run over the three families.
¹⁴⁵ The color indices are not shown. The first line of Eq. 1.14 contains the gaugino mass
¹⁴⁶ terms. The second line contains cubic scalar couplings that contribute to mixing
¹⁴⁷ between the left- and right-handed third generation sfermions (it is assumed in the
¹⁴⁸ supersymmetric Standard Model that the a_u^{ij} , a_d^{ij} , and a_e^{ij} are negligible unless $i =$
¹⁴⁹ $j = 3$). The third and fourth lines of Eq. 1.14 contain squark and slepton mass terms,
¹⁵⁰ and finally the last line contains the Higgs mass terms.

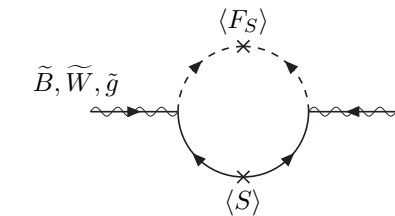
¹⁵¹ Many viable models of achieving soft SUSY breaking have been studied over the
¹⁵² last 30 years. For an overview, see Sec. 6 of ref. [6]. However, this thesis will only cover
¹⁵³ *gauge-mediated SUSY breaking* (GMSB), because the two-photon search performed
¹⁵⁴ is far more sensitive to this model than to other models of SUSY breaking.

¹⁵⁵ 1.4 Gauge-Mediated SUSY Breaking

¹⁵⁶ In gauge-mediated models [7], “hidden” fields spontaneously break the supersymme-
¹⁵⁷ try of very heavy chiral *messenger* supermultiplets. There are a number of compet-
¹⁵⁸ ing models (see ref. [7]) that explain the precise mechanism of spontaneous SUSY



(a) Sfermion mass terms. Heavy dashed lines denote messenger sfermions; solid lines denote messenger fermions. Reprinted from Fig. 6.4 of ref. [6].



(b) Gaugino mass term. The $\langle S \rangle$ part of the loop is a messenger fermion contribution; the $\langle F_S \rangle$ part is a messenger sfermion contribution. Reprinted from Fig. 6.3 of ref. [6].

Figure 1.2: Contributions to sfermion and gaugino masses from loop interactions with messenger particles in the GMSB framework.

159 breaking, but fortunately the details of those models mostly decouple from the phe-
 160 nomenology of GMSB. The messengers then communicate the SUSY breaking to the
 161 sparticles via loop diagrams of gauge interaction strength (i.e. via vertices like those
 162 shown in Figs. 1.1(c), 1.1(d), 1.1(i), 1.1(j), and 1.1(m), which are proportional to
 163 the SM gauge couplings constants). Feynman diagrams corresponding to gaugino and
 164 sfermion mass terms are shown in Figure 1.2.

165 Historically, GMSB and gravity-mediated SUSY breaking, or mSUGRA [8], have
 166 been the two most thoroughly experimentally studied scenarios of SUSY breaking.
 167 One advantage of GMSB over mSUGRA is that it naturally suppresses flavor vio-
 168 lation, a generic prediction of supersymmetry. Flavor violation is introduced in the
 169 scalar³ couplings and sfermion mass terms of $\mathcal{L}_{\text{soft}}$ (second, third, and fourth lines of

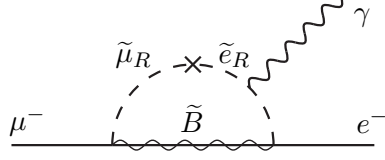


Figure 1.3: Possible contribution to $\mu \rightarrow e\gamma$ from $m_{\tilde{e}ij}$ soft term. Reprinted from Fig. 5.6(a) of ref. [6].

Eq. 1.14). Since a_u^{ij} , a_d^{ij} , a_e^{ij} , $m_{\tilde{Q}ij}$, $m_{\tilde{L}ij}$, $m_{\tilde{u}ij}$, $m_{\tilde{d}ij}$, and $m_{\tilde{e}ij}$ are matrices in family space, any nonzero off-diagonal elements will lead to mixing between sfermions of different families. This can lead, for example, to contributions to the diagram $\mu \rightarrow e\gamma$ (Figure 1.3) exceeding the experimental bounds. To avoid this disaster, *universality* conditions are assumed:

$$\mathbf{m}_{\tilde{\mathbf{Q}}}^2 = m_{\tilde{Q}}^2 \mathbf{1}, \mathbf{m}_{\tilde{\mathbf{L}}}^2 = m_{\tilde{L}}^2 \mathbf{1}, \mathbf{m}_{\tilde{\mathbf{u}}}^2 = m_{\tilde{u}}^2 \mathbf{1}, \mathbf{m}_{\tilde{\mathbf{d}}}^2 = m_{\tilde{d}}^2 \mathbf{1}, \mathbf{m}_{\tilde{\mathbf{e}}}^2 = m_{\tilde{e}}^2 \mathbf{1} \quad (1.15)$$

i.e. all sfermion mass matrices arising from the soft terms are assumed to be proportional to the unit matrix $\mathbf{1}$, such that there can be no flavor mixing from these terms and contributions to flavor-changing processes are drastically reduced.² In mSUGRA models, universality is assumed from the beginning, while in GMSB it is a natural consequence of the fact that the sparticle-messenger vertices are flavor-blind.

In minimal GMSB (mGMSB), there are four messenger supermultiplets q, \bar{q}, l, \bar{l} providing the messenger (s)quarks and (s)leptons. There is one breaking scale Λ . The gaugino masses computed from diagrams like Fig. 1.2(b) are given by

$$M_a = \frac{\alpha_a}{4\pi} \Lambda \quad (1.16)$$

²Universality also includes some assumptions about the form of $a_{u_{ij}}$, $a_{d_{ij}}$, and $a_{e_{ij}}$ and the stipulation that the soft terms not introduce any CP-violating phases.

¹⁸³ where a runs from 1-3 and the α_a are the SM gauge coupling constants. The sfermion
¹⁸⁴ masses computed from diagrams like Fig. 1.2(a) are given by

$$m_{\phi_i}^2 = 2\Lambda^2 \sum_{a=1}^3 \left(\frac{\alpha_a}{4\pi}\right)^2 C_a(i) \quad (1.17)$$

¹⁸⁵ where $C_a(i)$ are group theory factors that are identical for all particles residing in
¹⁸⁶ the same type of supermultiplet (e.g. for all left-handed (s)quarks or left-handed
¹⁸⁷ (s)leptons). As explained in the previous paragraph, the gaugino and sfermion masses
¹⁸⁸ do not depend on fermion family.

¹⁸⁹ In recent years, much theoretical progress has been made in unifying models of
¹⁹⁰ gauge mediation and developing less restrictive models than mGMSB. *General gauge*
¹⁹¹ *mediation* (GGM) [9] retains the essential features of mGMSB, such as flavor de-
¹⁹² generacy and communication of SUSY breaking via messengers, but does not make
¹⁹³ assumptions about the specific messenger sector or SUSY breaking scale. Many dif-
¹⁹⁴ ferent collider final states can be interpreted in terms of GGM, and conversely, GGM
¹⁹⁵ implies a wealth of signatures, only a small fraction of which have been searched for
¹⁹⁶ at colliders [10, 11, 12]. The following section discusses the aspects of GGM collider
¹⁹⁷ phenomenology relevant to this thesis.

¹⁹⁸ 1.5 Phenomenology of General Gauge Mediation

¹⁹⁹ The main distinguishing feature of all GMSB phenomenology is that the gravitino \tilde{G} is
²⁰⁰ very light (eV-keV). In general, the gravitino mass is proportional to $\langle F \rangle / M_P$, where
²⁰¹ $\langle F \rangle$ is the vacuum expectation value (VEV) of a field F that spontaneously breaks
²⁰² SUSY in the vacuum state and M_P is the Planck mass. In GGM models, $\langle F \rangle \sim 10^8$
²⁰³ GeV, leading to a very light gravitino. In contrast, mSUGRA predicts $\langle F \rangle \sim 10^{20}$
²⁰⁴ GeV. The fact that the gravitino is so much lighter than any other particles in the

205 supersymmetric Standard Model, and that it interacts only gravitationally (and thus
206 extremely feebly), leads to two important phenomenological consequences:

- 207 1. All sparticle decay chains end with the production of a gravitino.
- 208 2. The gravitino escapes 4π , hermetic collider detectors without interacting, leav-
209 ing a signature of “missing” momentum transverse to the beam direction.

210 Even if the gravitino were lighter than any other sparticle, but heavier than an
211 ordinary SM particle, it still could not decay to the SM particle due to *R-parity*. R-
212 parity is a conserved quantity of the supersymmetric Standard Model that enforces
213 baryon and lepton number conservation, which would otherwise be generically allowed
214 at levels in conflict with experiment (e.g. the non-observation of baryon- and lepton-
215 number-violating proton decay). All sparticles have R-parity -1, while all ordinary SM
216 particles have R-parity +1, and R-parity conservation dictates that at any vertex, the
217 product of the R-parities of each leg must be +1. This leads to two more important
218 consequences:

- 219 1. Since conservation of energy only allows it to decay to ordinary SM particles,
220 but R-parity prevents a sparticle-particle-particle vertex, the *lightest supersym-
221 metric particle* (LSP) must be absolutely stable. All sparticle decays proceed
222 through the *next-to-lightest supersymmetric particle* (NLSP), which in turn de-
223 cays to the LSP. The fact that it is stable and only gravitationally interacting
224 makes the gravitino a candidate dark matter particle (see Sec. 1.6).
- 225 2. In colliders, sparticles are produced in pairs (particle + particle \rightarrow sparticle +
226 sparticle).

227 In GMSB, then, the gravitino is the LSP. If the NLSP is a gaugino,³ then the
228 possible decays depend on mixing among the gauginos. Due to the effects of EWSB,

³In principle, the NLSP could be anything, but in most popular GGM models, it is either a gaugino or a stau. The stau NLSP search is not the subject of this thesis, so it will not be considered in this section.

²²⁹ the four neutral gauginos \tilde{H}_u^0 , \tilde{H}_d^0 , \tilde{B} , \tilde{W}^0 mix into four *neutralino* mass eigenstates
²³⁰ $\tilde{\chi}_1^0, \tilde{\chi}_2^0, \tilde{\chi}_3^0, \tilde{\chi}_4^0$, and the four charged gauginos $\tilde{H}_u^+, \tilde{H}_d^-, \tilde{W}^+, \tilde{W}^-$ mix into two *chargino*
²³¹ mass eigenstates $\tilde{\chi}_1^\pm, \tilde{\chi}_2^\pm$ (two mass eigenstates each with two possible charges = four
²³² particles). In the limit that EWSB effects are small, the neutralino and chargino
²³³ masses can be written as the gauge eigenstate masses plus a small perturbation:

$$m_{\tilde{\chi}_1^0} = M_1 - \frac{m_Z^2 \sin^2 \theta_W (M_1 + \mu \sin 2\beta)}{\mu^2 - M_1^2} + \dots \quad (1.18)$$

$$m_{\tilde{\chi}_2^0} = M_2 - \frac{m_W^2 (M_2 + \mu \sin 2\beta)}{\mu^2 - M_2^2} + \dots \quad (1.19)$$

$$m_{\tilde{\chi}_3^0} = |\mu| + \frac{m_Z^2 (\text{sgn}(\mu) - \sin 2\beta)(\mu + M_1 \cos^2 \theta_W + M_2 \sin^2 \theta_W)}{2(\mu + M_1)(\mu + M_2)} + \dots \quad (1.20)$$

$$m_{\tilde{\chi}_4^0} = |\mu| + \frac{m_Z^2 (\text{sgn}(\mu) + \sin 2\beta)(\mu - M_1 \cos^2 \theta_W - M_2 \sin^2 \theta_W)}{2(\mu - M_1)(\mu - M_2)} + \dots \quad (1.21)$$

$$m_{\tilde{\chi}_1^\pm} = M_2 - \frac{m_W^2 (M_2 + \mu \sin 2\beta)}{\mu^2 - M_2^2} + \dots \quad (1.22)$$

$$m_{\tilde{\chi}_2^\pm} = |\mu| + \frac{m_W^2 \text{sgn}(\mu)(\mu + M_2 \sin 2\beta)}{\mu^2 - M_2^2} + \dots \quad (1.23)$$

²³⁴ where $\tan \beta = \langle H_u^0 \rangle / \langle H_d^0 \rangle$.

²³⁵ The two scenarios studied in ref. [12] are the following:

²³⁶ • **Bino NLSP:** $M_1 \sim$ few hundred GeV, $M_2, |\mu| \gg M_1$. All but the lightest
²³⁷ neutralino are effectively inaccessible at the LHC due to their large masses. The
²³⁸ NLSP can always decay to $\gamma + \tilde{G}$, and if it is heavy enough, to $Z + \tilde{G}$ or $H + \tilde{G}$.

²³⁹ • **Wino NLSP:** $M_2 \sim$ few hundred GeV, $M_1, |\mu| \gg M_2$. The lightest neutralino
²⁴⁰ and the lightest chargino are nearly degenerate in mass, and are the only two
²⁴¹ particles to play a role at the LHC. The decays described in the previous bullet
²⁴² point can happen, as well as chargino decays to $W + \tilde{G}$.

²⁴³ The subject of this thesis is the classic bino NLSP decay $\gamma + \tilde{G}$.

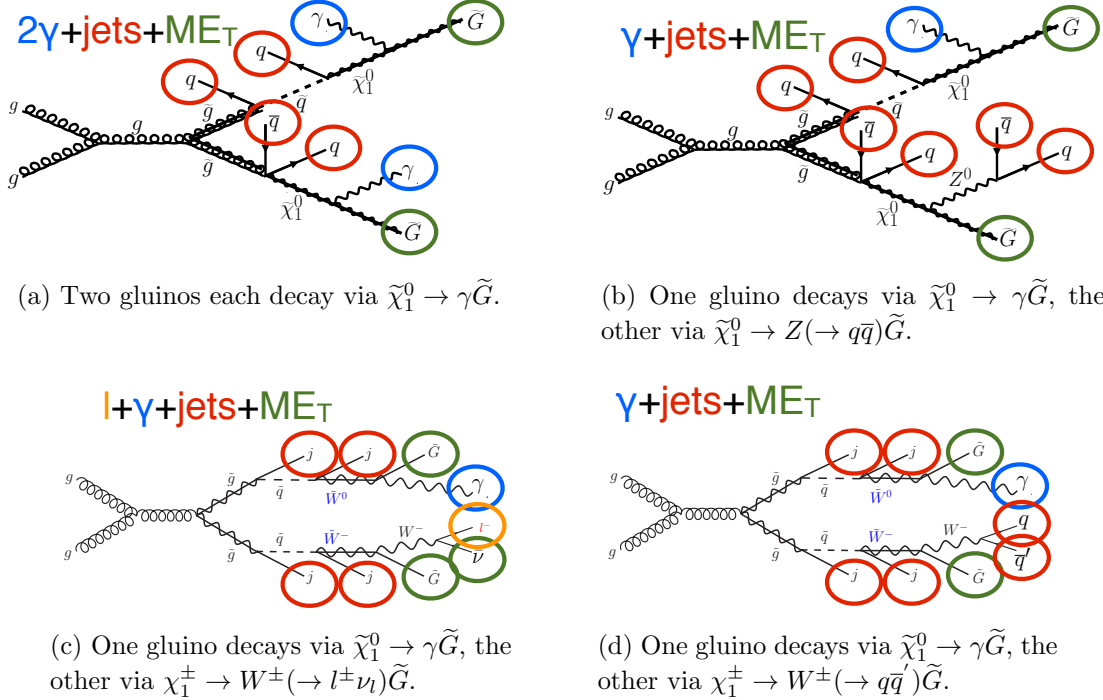


Figure 1.4: Typical LHC signatures of the bino and wino NLSP scenarios.

244 Since strong production of SUSY particles dominates over electroweak production
245 at the LHC due to the enhanced gg parton luminosity over the $q\bar{q}$ parton luminosity,
246 early LHC searches are particularly sensitive to light squarks and gluinos. General
247 gauge mediation makes no a priori restrictions on the mass splitting between the
248 strongly interacting sparticles and the weakly interacting sparticles, so models with
249 light squarks and gluinos are viable. In fact, such models could not be probed as
250 well at the Tevatron⁴ as they are at the LHC due to the aforementioned parton
251 luminosities.

252 Typical LHC signatures of the bino and wino NLSP scenarios are shown in Fig-
253 ure 1.4.

⁴Located on the Fermilab site in Batavia, Illinois, the Tevatron was a proton-antiproton collider operating at 1.96 TeV center-of-mass energy. The Tevatron ran from 1987 to 2011 [13].

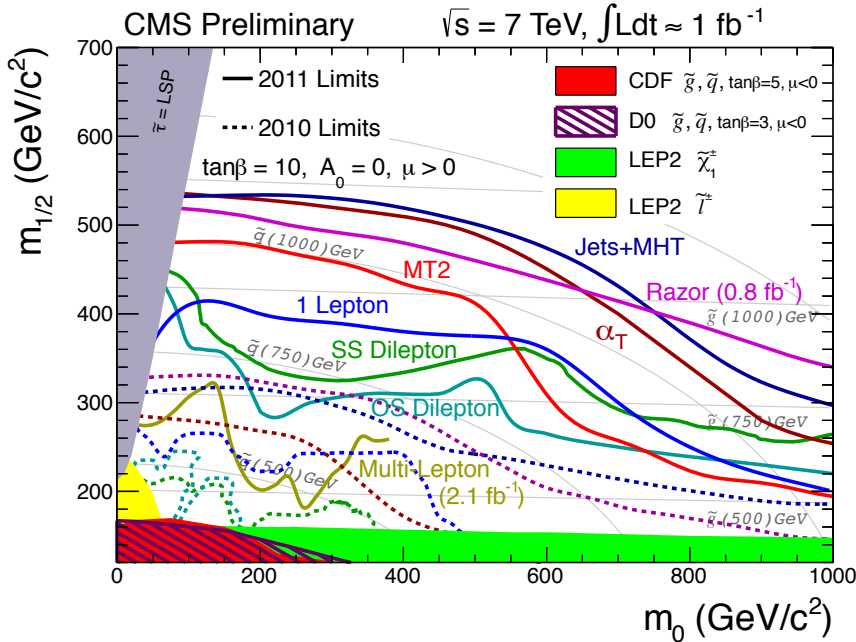


Figure 1.5: CMS limits on mSUGRA with $\tan \beta = 10$. The limits set by individual searches are shown as separate colored lines. Solid lines refer to 2011 searches (i.e. using an integrated luminosity of $\sim 1 \text{ fb}^{-1}$), while dashed lines refer to 2010 searches ($\sim 36 \text{ pb}^{-1}$). Reprinted from ref. [16].

254 1.6 Experimental Status of SUSY

255 Collider searches for evidence of supersymmetry began in earnest in the 1980s [14]
 256 and continue to this day. Most recently, the LHC and Tevatron experiments have set
 257 the strictest limits on a variety of SUSY breaking scenarios, including GMSB and
 258 mSUGRA.

259 Figure 1.5 shows the current limits set by the CMS experiment on the mSUGRA
 260 model (with $\tan \beta = 10$) in the m_0 - $m_{1/2}$ plane. (Note that although the plot is trun-
 261 cated at $m_0 = 1000 \text{ GeV}/c^2$, some searches are sensitive out to $m_0 \sim 2000 \text{ GeV}/c^2$.)
 262 Although the LHC has pushed m_0 above $\sim 1 \text{ TeV}/c^2$ for $m_{1/2}$ up to $\sim 400 \text{ GeV}/c^2$,
 263 casting some doubt onto the theory's prospects for solving the hierarchy problem,
 264 there is still a sizable chunk of mSUGRA parameter space that is not ruled out by
 265 collider experiments. Furthermore, parts of the CMS unexplored regions overlap with
 266 areas allowed by astrophysics experiments [15].

Removed

CMS

Moriond

result

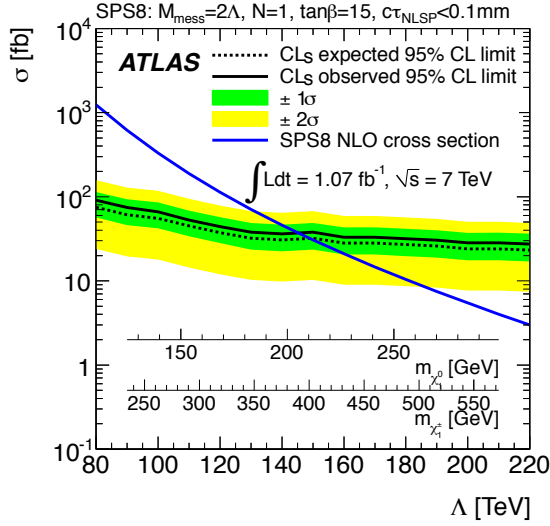


Figure 1.6: ATLAS cross section upper limit on the SPS8 [18] model of mGMSB as a function of SUSY breaking scale Λ , lightest neutralino mass $m_{\tilde{\chi}_1^0}$, or lightest chargino mass $m_{\tilde{\chi}_1^\pm}$. Values of Λ , $m_{\tilde{\chi}_1^0}$, or $m_{\tilde{\chi}_1^\pm}$ below the intersection point between the blue (predicted SPS8 cross section) and black (observed cross section upper limit) curves are excluded. The model parameters listed above the plot are defined in Secs. 1.4 and 1.5, except for τ_{NLSP} , which is the neutralino lifetime. Reprinted from ref. [10].

267 Figure 1.6 shows the most up-to-date limit (using 1 fb^{-1} of integrated luminos-
268 ity collected by the ATLAS experiment [17] at the LHC) on the Snowmass Points
269 and Slopes (SPS) model of mGMSB, dubbed SPS8 [18]. In general, the lifetime of
270 the lightest neutralino in GMSB models can take on any value between hundreds of
271 nanometers to a few kilometers depending on the mass of the lightest neutralino and
272 the SUSY breaking scale [6]. The search published in ref. [10] (from which Figs. 1.6
273 and ?? are culled) considers only *prompt* neutralino variants, i.e. with neutralino life-
274 time short enough that the distance traveled by the neutralino before decay cannot be
275 resolved by the detector. The most recent limits on non-prompt SPS8-style neutralino
276 models were set by the Collider Detector at Fermilab (CDF) collaboration with 570
277 pb^{-1} , and are shown in Figure 1.7 [11].

278 Finally, if the gravitino is to make up some or all of the dark matter, constraints
279 on the form of gauge mediation must come from cosmological considerations and
280 astronomical observations. The gravitino in gauge mediation models is usually very

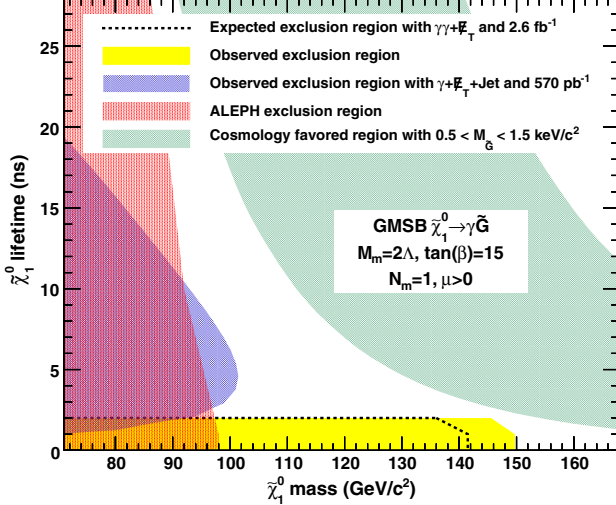


Figure 1.7: CDF exclusion contour in the $\tau_{\tilde{\chi}_1^0}$ - $m_{\tilde{\chi}_1^0}$ plane, where $\tau_{\tilde{\chi}_1^0}$ is the lifetime of the neutralino. Reprinted from ref. [11].

281 light ($\mathcal{O}(\text{eV-MeV})$) because it is proportional to the SUSY breaking scale divided by
 282 the Planck mass, and in GMSB the breaking scale is typically only of order a few
 283 hundred TeV ([6] and Sec. 1.5). A light, highly relativistic dark matter particle might
 284 have been produced, for instance, in the early, radiation-dominated period of the
 285 universe [20]. This *warm dark matter* (WDM) may be responsible for all of the dark
 286 matter needed to account for galactic structure, or it may share the duties with *cold*
 287 *dark matter* (CDM, weakly interacting particles with masses in the GeV range). In
 288 any viable model, the predicted relic density of the dark matter species must match
 289 the observed value of $\Omega h^2 \sim 0.1$ [21]. For many GMSB models, this measurement
 290 constrains the gravitino mass to the keV range [22]. This constraint, however, does
 291 not translate into a very strong bound on the lifetime of the lightest neutralino. Using
 292 the following equation (taken from [22]):

$$\tau_{\tilde{\chi}_1^0} \sim 130 \left(\frac{100 \text{ GeV}}{m_{\tilde{\chi}_1^0}} \right)^5 \left(\frac{\sqrt{\langle F \rangle}}{100 \text{ TeV}} \right)^4 \mu\text{m} \quad (1.24)$$

293 and applying the gravitino mass constraint $\sqrt{\langle F \rangle} \lesssim 3000 \text{ TeV}$ (cf. the first paragraph
 294 of Sec. 1.5 with $m_{\tilde{G}} \sim \text{keV}$) and $m_{\tilde{\chi}_1^0} = 100 \text{ GeV}$, the upper bound on the neutralino

295 lifetime is 100 meters. For $\sqrt{\langle F \rangle} \sim 100$ TeV, the neutralino lifetime is detectable on
296 collider time scales.

297 Recently, a lower bound on the WDM particle mass in either pure warm or mixed
298 warm and cold dark matter scenarios was set using observations of the Lyman- α for-
299 est. For pure WDM, $m_{\text{WDM}} > 8$ keV, while for some mixed WDM-CDM scenarios,
300 $m_{\text{WDM}} > 1.1\text{-}1.5$ keV [20, 23]. These bounds and others have motivated the develop-
301 ment of more complicated gauge mediation models [23]. However, rather than focus
302 on a specific GMSB model, of which there are many, the search detailed here is in-
303 terpreted in a minimally model dependent way. With this approach, the results can
304 be applied to many competing models. The remainder of this thesis is devoted to the
305 experimental details of the search, analysis strategy, and presentation of the results.
306 The work described in this thesis forms the basis for the CMS public result “Search
307 for Supersymmetry in Events with Photons and Missing Energy” [19], published in
308 April 2012.

309 **Chapter 2**

310 **The Compact Muon Solenoid**
311 **Experiment**

312 The Compact Muon Solenoid (CMS) detector sits at point 5 of the LHC ring, diamet-
313 rically opposite the ATLAS detector at point 1. It is a 4π hermetic general purpose
314 detector, meaning that it has the capability to detect charged and neutral hadrons,
315 photons, electrons, muons, taus, neutrinos, and non-Standard-Model particles pre-
316 dicted to escape the detector with good efficiency over a large range of rapidity.
317 Its main distinguishing feature is a superconducting solenoid that provides a 3.8T
318 magnetic field parallel to the beam line. This strong magnetic field allows precise de-
319 termination of the momentum and charge of muons and electrons up to a momentum
320 of ~ 1 TeV.

321 The origin of the CMS coordinate system is at the nominal interaction point. The
322 y -axis points skyward, the x -axis points towards the center of the LHC ring, and
323 the z -axis points counterclockwise along the LHC ring. r denotes radial distances
324 from the beam line, ϕ is the azimuthal angle measured with respect to the positive
325 x -axis, and θ is the polar angle measured with respect to the positive z -axis. The
326 *pseudorapidity* η is defined as $\eta = -\ln \tan(\theta/2)$, and is a good approximation to

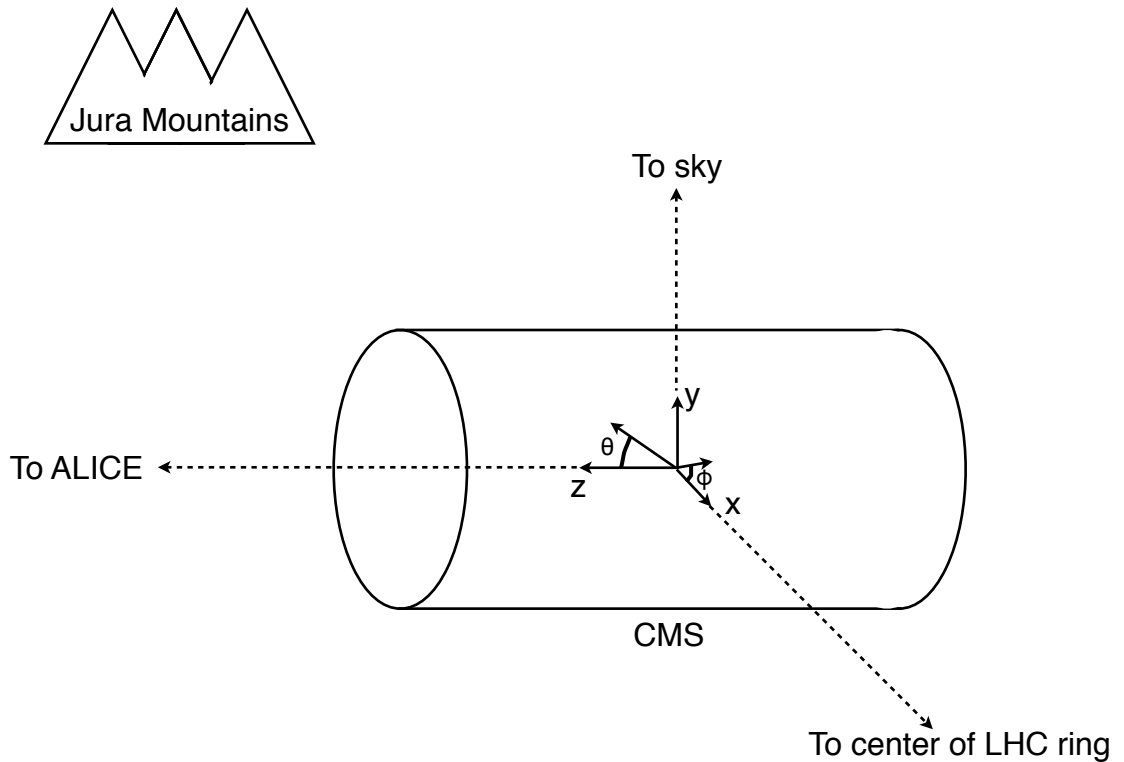


Figure 2.1: CMS coordinate system.

327 rapidity $y = (1/2) \ln((E + p_z c)/(E - p_z c))$ for relativistic particles. The transverse
 328 momentum and energy (p_T and E_T) of a particle are defined as $p_T = p \cos \phi$ and
 329 $E_T = E \cos \phi$, where p and E are the magnitude of the particle's momentum vector
 330 and the particle's total energy, respectively. A depiction of the CMS coordinate system
 331 is shown in Figure 2.1.

332 The CMS sub-detectors are arranged in concentric cylindrical layers, plus “end-
 333 caps,” around the beam line, as shown in Figure 2.2. Closest to the beam line are
 334 three layers of silicon pixel detectors, with the innermost at radius 4.4 cm and out-
 335 ermost at radius 10.2 cm [24]. Including the pixel endcaps, the total pixel coverage

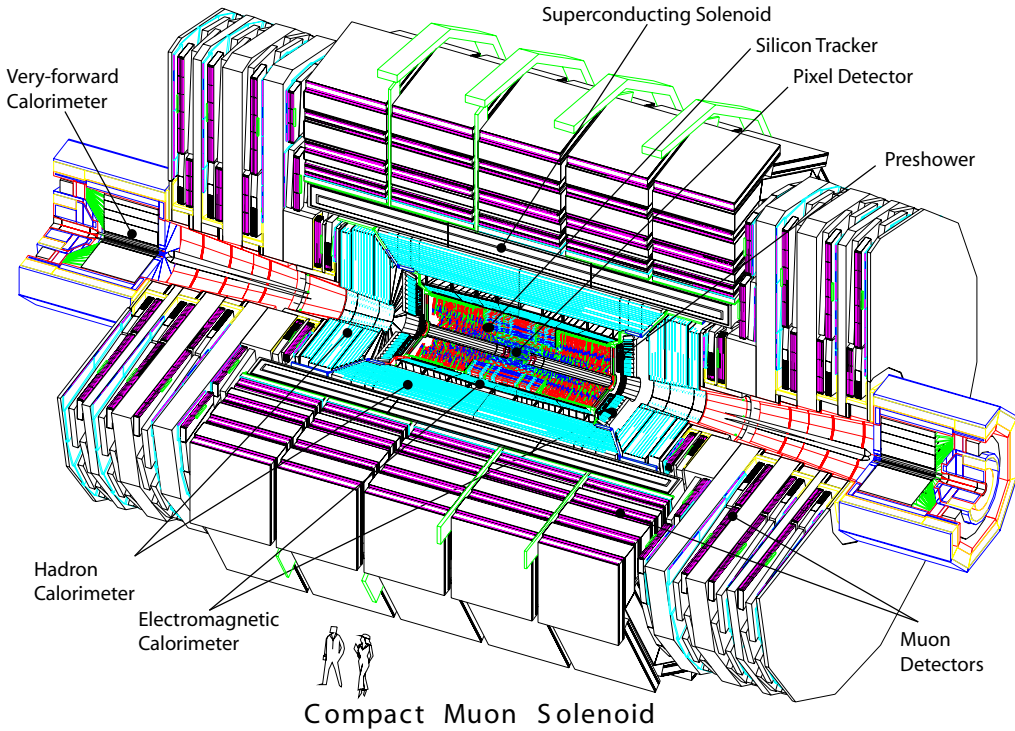


Figure 2.2: Cutaway view of CMS. Reprinted from Fig. 1.1 of ref. [24].

336 extends to $\eta = 2.5$ [24]. The pixel detector plays an important role in determining the
 337 proton-proton interaction position (*beam spot*) and the impact parameters of charged
 338 particle trajectories, and is critical for the measurement of decay positions some dis-
 339 tance from the beam spot (*displaced vertices*), such as those due to the showering and
 340 hadronization of a b quark.

341 The 10 next layers of CMS are comprised of silicon microstrip detectors, with the
 342 outermost layer at a radius of 1.3 m from the beam line [24]. As for the pixel detectors,
 343 the silicon strip endcaps extend tracking coverage to $\eta = 2.5$. The silicon microstrip
 344 layers are the workhorse of the CMS tracking system, and provide excellent charged
 345 particle momentum resolution and track finding efficiency.

346 Outside the tracking detectors are the calorimeters, starting with the single-layer
 347 lead tungstate crystal electromagnetic calorimeter at a radius of 1.3 m from the beam
 348 line (location of crystal front faces) [24]. Each crystal is 23 cm long, corresponding

349 to 25.8 radiation lengths (X_0) [24]. The crystal dimensions are such that most of one
 350 electromagnetic shower, and no more, can be contained in a single crystal, leading to
 351 excellent energy resolution for photons and electrons. The electromagnetic calorime-
 352 ter radial and endcap layers cover a pseudorapidity range up to 3.0. A lead/silicon
 353 sampling calorimeter sits in front of the crystal endcaps to provide better rejection
 354 of neutral pions.

355 The last layer of calorimetry inside the solenoid is the brass/scintillator sampling
 356 hadronic calorimeter, which has a radial extent from 1.77-2.95 m [24]. The hadronic
 357 barrel and endcap calorimeters cover up to $|\eta| = 3.0$, while the iron/quartz-fiber for-
 358 ward hadronic calorimeter covers the region $3.0 \leq |\eta| \leq 5.2$.¹ There is one more
 359 layer of hadronic calorimetry outside the solenoid in $|\eta| < 1.3$ which, together with
 360 the layers inside the solenoid, provides approximately 12 hadronic interaction lengths
 361 of instrumented absorber. Because of its large $|\eta|$ coverage and depth, the hadronic
 362 calorimeter provides good missing transverse energy resolution and accurate measure-
 363 ments of high energy jets.

364 The iron return yoke of the solenoidal magnetic field is interleaved with muon
 365 detectors from 4.1-7.4 m in r and 6.6-10.6 m in z , providing muon detection up to
 366 $|\eta| = 2.4$ [24]. In the barrel region of $|\eta| < 1.2$, drift tubes are used to read out the
 367 muon tracks, while in the endcaps cathode strip chambers are used. Due to their
 368 speed, resistive plate chambers are used throughout the muon system to provide
 369 an independent trigger and timing measurement. Combining the tracker and muon
 370 system hits, the momenta and charge of muons up to $p_T = 1$ TeV can be precisely
 371 reconstructed.

372 A longitudinal quarter cross-sectional view of CMS is shown in Figure 2.3. The
 373 remainder of this chapter is devoted to explaining the CMS subdetectors and readout

¹The Centauro and Strange Object Research (CASTOR) and Zero Degree Calorimeter (ZDC) detectors provide additional calorimetry beyond $|\eta| = 5.2$. However, they are mainly used in the heavy ion and diffractive physics programs of CMS, and play no role in the detection of heavy SUSY particles. Therefore, they will not be discussed here.

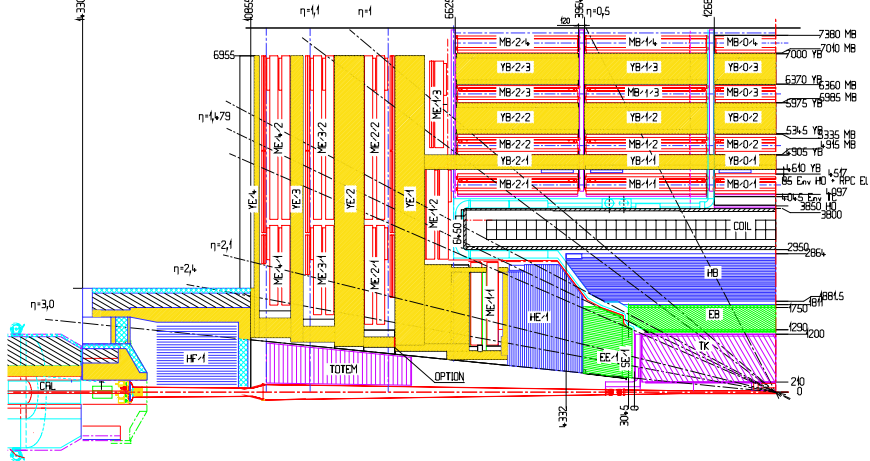


Figure 2.3: Longitudinal quarter cross-sectional view of CMS. The nominal interaction point is at the lower right-hand corner of the drawing. The tracker is shown in purple diagonal hashing, the electromagnetic calorimeter in green, the hadronic calorimeter in blue, and the muon stations in red. The solenoid is shown in black and white and labeled COIL, and the magnet return yoke is shown in yellow. Radial and longitudinal distances are measured in millimeters. Reprinted from Fig. CP 1 of ref. [25].

systems. Section 2.1 describes the subdetector technologies and performance benchmarks, while Section 2.2 details the CMS trigger and data acquisition systems and framework for promptly reconstructing and transferring data worldwide. For a thorough description of CMS, see ref. [24]. Unless otherwise noted, all information in this chapter comes from ref. [24].

379 2.1 The Detectors and Their Operating Principles

380 2.1.1 Tracking System

Given the LHC design instantaneous luminosity, efficient reconstruction of charged particle tracks from transverse momenta of 1 GeV up to 1 TeV can only be achieved with a low occupancy tracker. For $r < 10$ cm, the hit rate density is highest, leading to the choice of $100 \mu\text{m} \times 150 \mu\text{m}$ silicon pixel sensors for hit detection. For $20 \text{ cm} < r < 110 \text{ cm}$, the lower hit rate allows the use of silicon strips, with length along z of

³⁸⁶ order centimeters and length along the $r \cdot \phi$ curve of order hundreds of microns. This
³⁸⁷ design leads to a pixel hit occupancy of $\sim 10^{-4}$ /pixel/BX and a strip hit occupancy
³⁸⁸ of $\sim 10^{-2}$ /pixel/BX, where BX refers to 1 LHC bunch crossing.

³⁸⁹ As radiation dose from hadrons accumulates over the lifetime of the tracker, silicon
³⁹⁰ leakage current through the semiconductor junctions increases, heating up the sensors.
³⁹¹ Since the leakage current itself depends on temperature, this can lead to *thermal*
³⁹² *runaway* that damages the detector. To avoid this, the tracker must be cooled to
³⁹³ approximately -10°C . Operating at this temperature, the signal:noise ratio in the
³⁹⁴ silicon sensors is 10:1, and should remain at that level over the 10-year lifetime of the
³⁹⁵ tracker.

³⁹⁶ At its thickest ($|\eta| \sim 1.5$), the tracker depth (including services) is $\sim 1.8X_0$,
³⁹⁷ and the depth falls off to $\sim 1X_0$ in thinner areas. Unfortunately, the large mass of
³⁹⁸ the tracker degrades somewhat the performance of the electromagnetic calorimeter
³⁹⁹ behind it, as $\sim 50\%$ of photons will convert to e^+e^- pairs in the tracker.

⁴⁰⁰ Pixel Detector

⁴⁰¹ A longitudinal quarter view of the three barrel pixel (BPix) layers and two forward
⁴⁰² pixel (FPix) disks is shown in Figure 2.4. There are 768 BPix modules in total.
⁴⁰³ Each BPix layer is divided into 32 ϕ -wedges, with eight modules per wedge arranged
⁴⁰⁴ end-to-end in z . The ϕ -wedges operate nearly independently in terms of clock and
⁴⁰⁵ readout. Each FPix disk consists of 24 ϕ -wedges, with pie-shaped modules attached
⁴⁰⁶ to the front and back of the disk, for a total of 192 modules. The front- and back-side
⁴⁰⁷ modules of the FPix disks are constructed of different sized *plaquettes*, or multi-pixel
⁴⁰⁸ sensor chips, such that the gaps in the front-side module are covered by plaquette
⁴⁰⁹ area in the back-side module and vice versa. An illustration of the BPix and FPix
⁴¹⁰ mechanical layouts is given in Figure 2.5.

⁴¹¹ Since the electric field in the depletion region of the BPix sensors is perpendicular

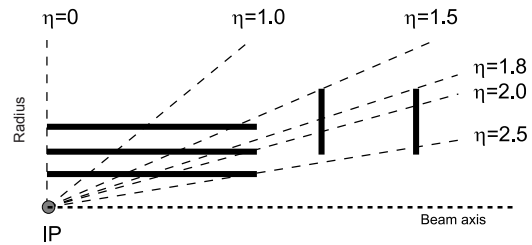


Figure 2.4: Longitudinal quarter view of the pixel detector. Reprinted from Fig. 3.6 of ref. [24].

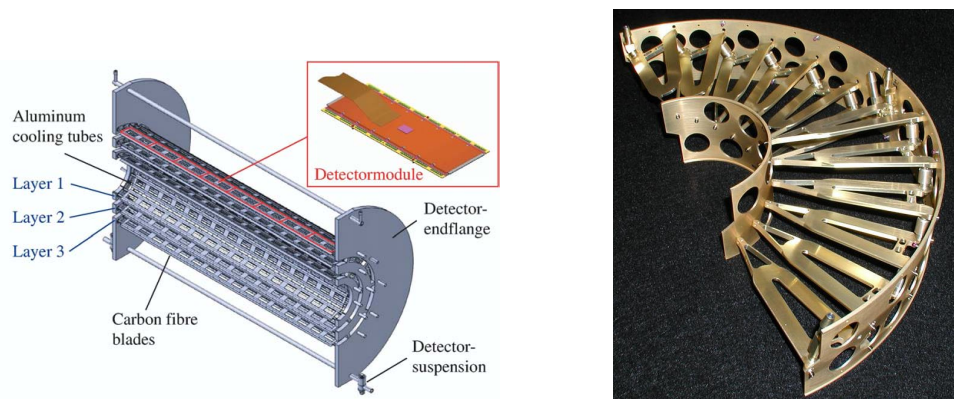


Figure 2.5: BPix and FPix mechanical structures.

412 (i.e. pointing along r) to the magnetic field of CMS (i.e. pointing along z), the charge
 413 carriers in the silicon experience a Lorentz drift along ϕ . The multi-pixel sensor pitch
 414 is such that this causes the charge from one particle hit to be shared among multiple
 415 pixels. Particle hits are reconstructed reading out the analog pixel signal and inter-
 416 polating between signals in multiple pixels. This method achieves a $15\text{-}20 \mu\text{m}$ spatial
 417 resolution, which is comparable to the sensor pitch. To induce this effect in FPix,
 418 the sensor wedges are tilted by the approximate BPix Lorentz angle of 20° [26] with
 419 respect to the y -axis.

420 Each multi-pixel sensor consists of an array of 52×80 n-type pixels implanted
 421 onto an n-type substrate with $320 \mu\text{m}$ thickness. The other face of the substrate is
 422 covered with a thin layer of p-type semiconductor. Except for the outer edges, which
 423 are held at ground potential to prevent sparking between the sensor edges and the
 424 connected readout chip [27], the p-side is reverse biased at a few hundred volts. The
 425 pixels are held at ground potential. A particle entering through the p-side will cause
 426 a burst of current to flow across the p-n junction. The charge will be collected by the
 427 pixels, which are bump-bonded to the readout. The BPix and FPix sensors employ
 428 slightly different technologies for electrically isolating the individual pixels, but both
 429 rely on the idea of surrounding the pixels with a p-type material to provide a p-n
 430 junction that acts as a barrier to current flow.

431 Each 52×80 pixel sensor is bump bonded to a readout chip (ROC). The ROCs
 432 provide zero suppression and amplify, buffer, and communicate the signals from the
 433 sensors. A single token bit manager (TBM) controls ~ 16 ROCs in the barrel or ~ 24
 434 ROCs in the endcaps. Its purpose is to distribute the clock and trigger to the ROCs
 435 (the latter initiates a transmission of the signal further upstream to be assembled
 436 into the full event readout of CMS). The clock and trigger are supplied by the pixel
 437 front end controller (pFEC), which interfaces to the central clock and data acquisition
 438 systems. Analog signals that are collected from the pixel front ends are digitized by

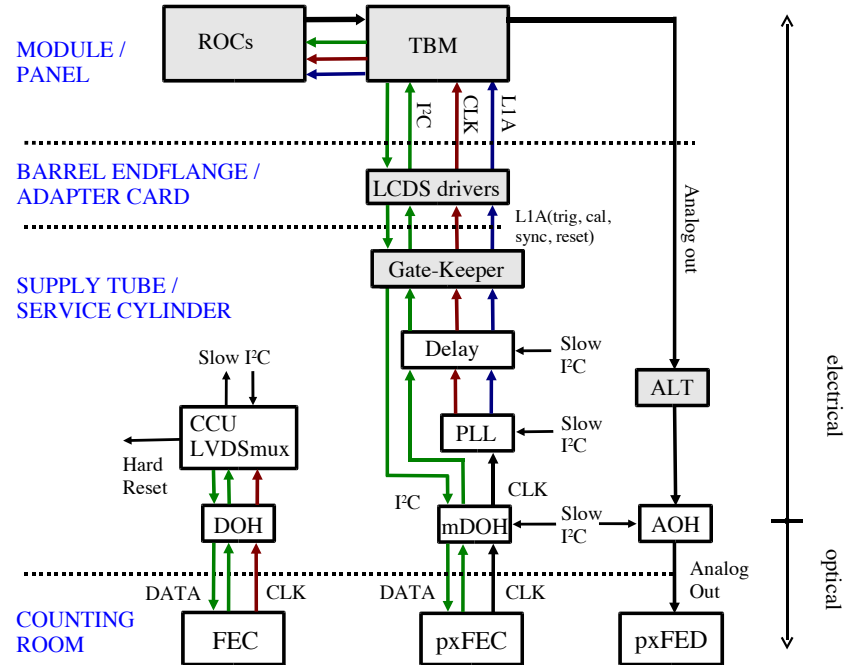


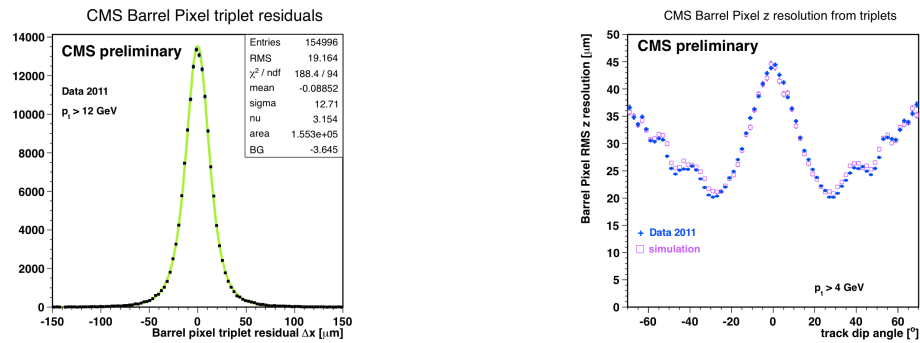
Figure 2.6: Pixel control and readout system. Reprinted from Fig. 3.9 of ref. [24].

439 the pixel front end digitizer (pxFED). A diagram of the readout system is shown in
 440 Figure 2.6.

441 Figure 2.7 shows some results highlighting the performance of the pixel detector.

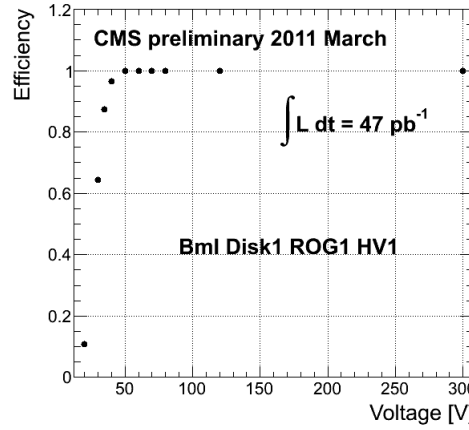
442 Silicon Strip Tracker

443 The silicon strip tracker is divided into four parts: the inner barrel (TIB) and inner
 444 disks (TID), covering the radial extent $20 \text{ cm} < r < 55 \text{ cm}$ and z extent $80 \text{ cm} <$
 445 $|z| < 90 \text{ cm}$; and the outer barrel (TOB) and endcap (TEC), covering the radial
 446 extent $61 \text{ cm} < r < 108 \text{ cm}$ and z extent $124 \text{ cm} < |z| < 282 \text{ cm}$. A number of the
 447 tracker layers and endcaps hold double-sided strip modules (shown as double lines
 448 in Figure 2.8), with the rear module tilted at an angle of 100 mrad with respect to
 449 the front module, to provide a measurement in two coordinates. There are a total of
 450 15,148 modules in the tracker, arranged as shown in the longitudinal cross-sectional
 451 view of Fig. 2.8. For the TIB and TOB, the modules are arranged in straight rows



(a) BPix hit resolution in the $r \cdot \phi$ coordinate [28].

(b) BPix hit resolution in the z coordinate vs. track dip angle, showing the effect of charge sharing on resolution [29].



(c) Pixel reconstruction efficiency vs. bias voltage for a group of three wedges in FPix [30].

Figure 2.7: Pixel detector performance highlights.

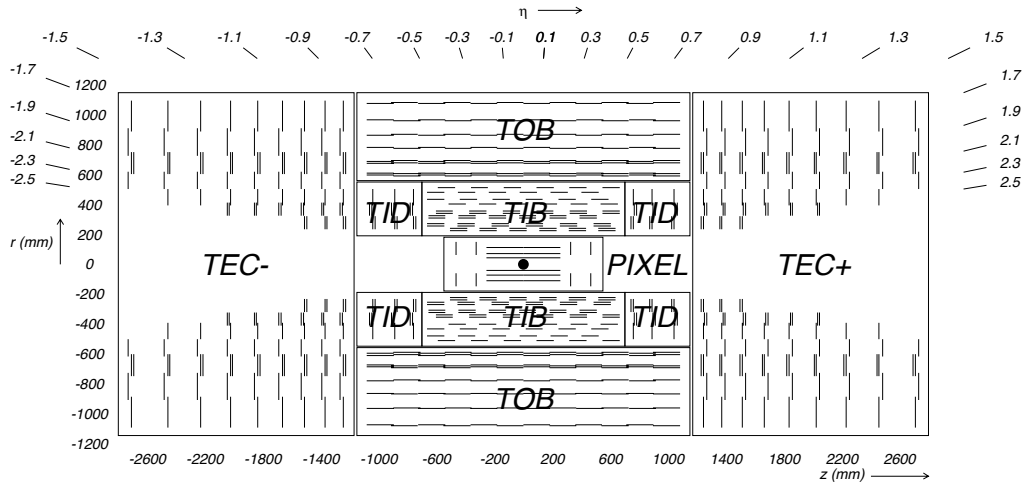


Figure 2.8: Longitudinal cross section of the silicon strip detector. Reprinted from Fig. 3.1 of ref. [24].

452 end-to-end along z , with repeating rows covering the full 2π extent in ϕ . In each of the
 453 TID disks, the modules are arranged into three concentric circular rings of increasing
 454 r . In the TEC, the modules are affixed to ϕ -wedges called *petals*. One side of the TEC
 455 and its petal structure is shown in Figure 2.9.

456 Like the pixels, the strip sensors generate a signal when current flows across a
 457 p-n junction in response to interaction with a charged particle. Whereas the pixels
 458 are n-type implants on an n-type substrate, with a solid p-type rear layer to which
 459 the high voltage is connected, the strips are p-type implants on an n-type substrate,
 460 with a solid n-type rear layer connecting to the high voltage. The p-n junction in the
 461 strip sensors is at the strip-substrate boundary, whereas in the pixel sensors it is at
 462 the boundary between the rear layer and the substrate. Each sensor has either 512
 463 or 768 electrically isolated strips, with pitch varying from 80-205 μm depending on
 464 location. Strip lengths in z range from ~ 10 to ~ 25 cm. Thin (320 μm) sensors are
 465 used in the TIB, TID, and inner four rings of the TEC, while thick (500 μm) sensors
 466 are used in the TOB and the outer rings of the TEC. The thicker sensors compensate
 467 for the increased strip capacitance (and hence electronics noise) of the longer strips
 468 in the outer layers/disk of the tracker such that strip signal:noise is maintained above

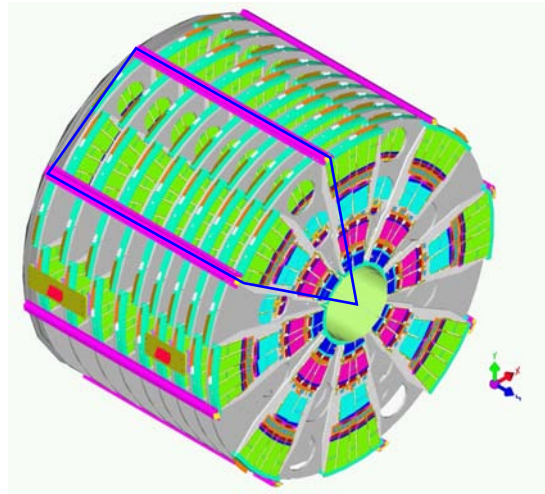


Figure 2.9: View of one tracker endcap, with the outline of a petal shown in blue. There are nine petals per wedge-shaped sector (one per TEC disk). Reprinted from Fig. 3.30 of ref. [24].

469 10 everywhere.

470 The strips are wire bonded to a front end readout chip called the APV25. The
 471 APV25 amplifies and shapes the strip signals before sending the full analog pulse
 472 information to an APVMUX, which multiplexes the output of two APV25s. Then,
 473 the electrical signal from the APVMUX is sent differentially a few centimeters to an
 474 optical driver, where it is converted to an optical signal and sent to one of the 450
 475 front end drivers (FEDs). The FEDs convert the signal back to an electrical pulse
 476 and digitize it for use in the global event assembly. As for the pixels, analog readout
 477 is used on detector so that hit reconstruction may benefit from charge sharing.

478 Clock, trigger, and control signals are sent from the front end controllers (FECs)
 479 to phase locked loop (PLL) chips on the front ends. The FECs interface to the global
 480 clock and trigger system. Four or six APV25s, an APVMUX, and a PLL chip all sit on
 481 a *hybrid*, two which one thin or two thick sensors are also affixed. The sensor-hybrid
 482 combination and its frame form a module. Figure 2.10 shows a diagram of a module,
 483 while Figure 2.11 shows a block diagram of the strip readout architecture.

484 As an example of the strip capabilities, strip hit resolution and signal:noise mea-

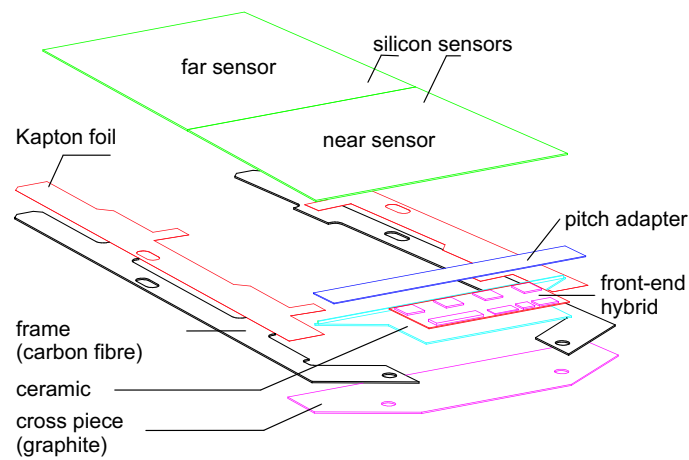


Figure 2.10: Exploded view of a strip module with two sensors. Reprinted from Fig. 3.22 of ref. [24].

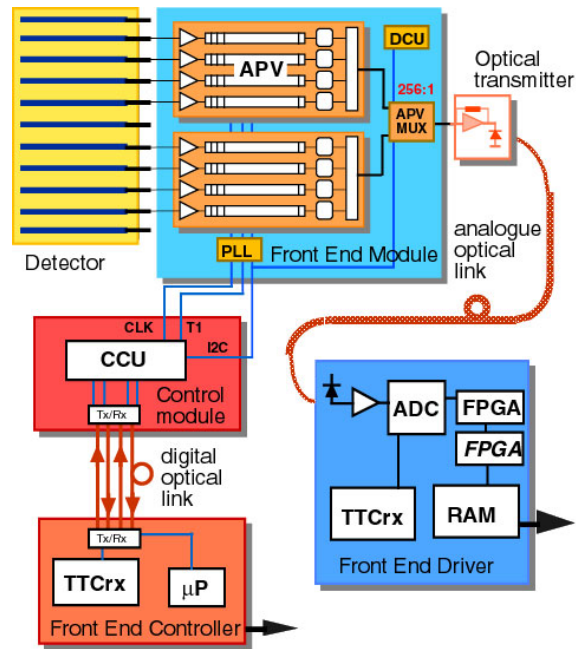


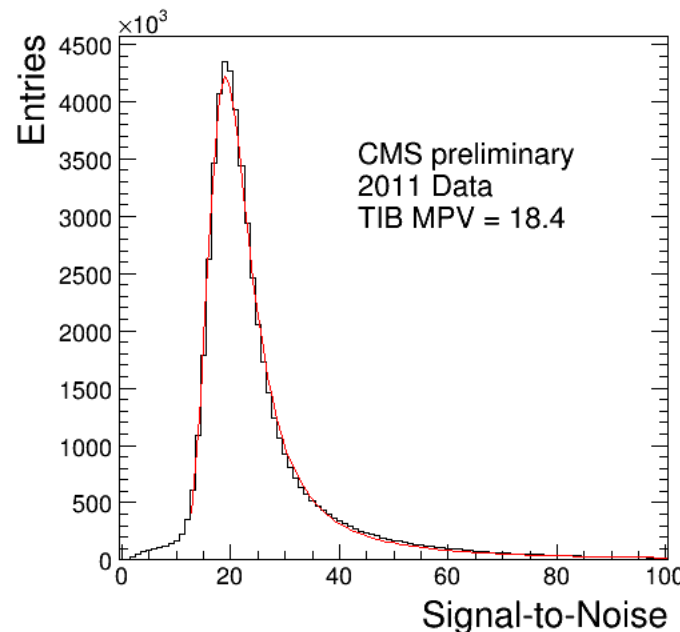
Figure 2.11: Block diagram of the strip readout architecture. Reprinted from Fig. 3.20 of ref. [24].

surements are shown in Figure 2.12. The entire pixel + strip tracker has been used successfully in the reconstruction of primary and secondary vertices, electrons, muons, tau decays, and charm and bottom hadron decays. In addition, the superior performance of the tracker over the hadronic calorimeter for low energy charged hadrons has been exploited in the the particle flow jet and \cancel{E}_T reconstruction technique (see Sec. 3.1.3). The CMS silicon strips, as well as the pixels, are well aligned and operating at close to design performance.

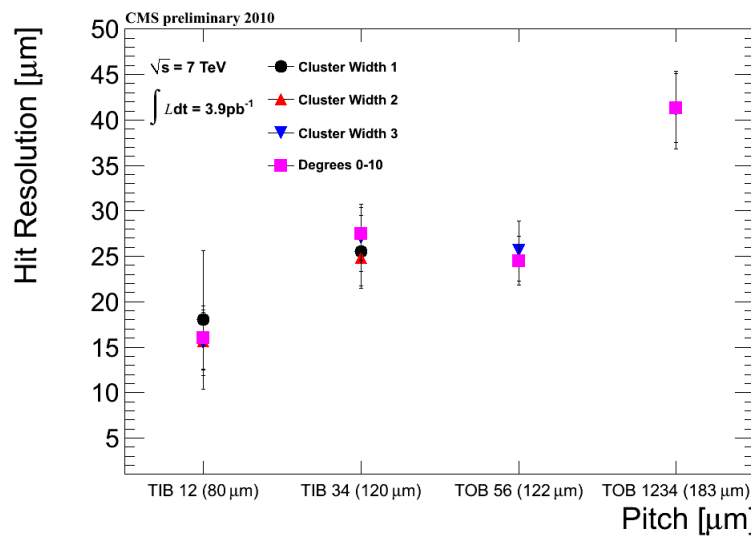
2.1.2 Electromagnetic Calorimeter

The electromagnetic calorimeter (ECAL) is composed of 68,524 lead tungstate (PbWO_4) crystals, divided into one barrel (EB) layer and two endcap (EE) disks. In EB, there are 1700 crystals per *supermodule* (SM), arranged in a 20×85 grid in $\phi \times \eta$. Two SMs are laid out end-to-end to form one row at fixed ϕ , with a total of 18 rows needed to cover the entire 2π extent in ϕ . The SMs may be operated independently. In EE, the independent unit is a wedge-shaped sector, with nine sectors covering each endcap side. The 7,324 EE crystals are divided approximately evenly between the 18 EE sectors. A two-layer preshower detector is placed in front of the EE disks, each layer consisting of a lead absorber followed by 1.9 mm pitch silicon strip detectors (the strips in the first layer are rotated 90° with respect to the second layer). The ECAL layout is shown in Figure 2.13.

The electromagnetic energy resolution can be parametrized as $(\sigma/E)^2 = (S/\sqrt{E})^2 + (N/E)^2 + (C)^2$, where S characterizes the size of photostatistical fluctuations, N characterizes the contribution from electronics noise, and C is a constant accounting for imperfect intercalibration between crystals, non-uniformity of crystal performance, and incomplete shower containment within one crystal. The design goal of the ECAL is to achieve $C = 0.5\%$. Therefore, fast, dense, and relatively radiation hard PbWO_4 was chosen as the crystal material. When a photon or electron strikes the crystal, it



(a) TIB signal:noise [31].



(b) TIB and TOB hit resolution as a function of strip pitch [32].

Figure 2.12: Strip detector performance highlights.

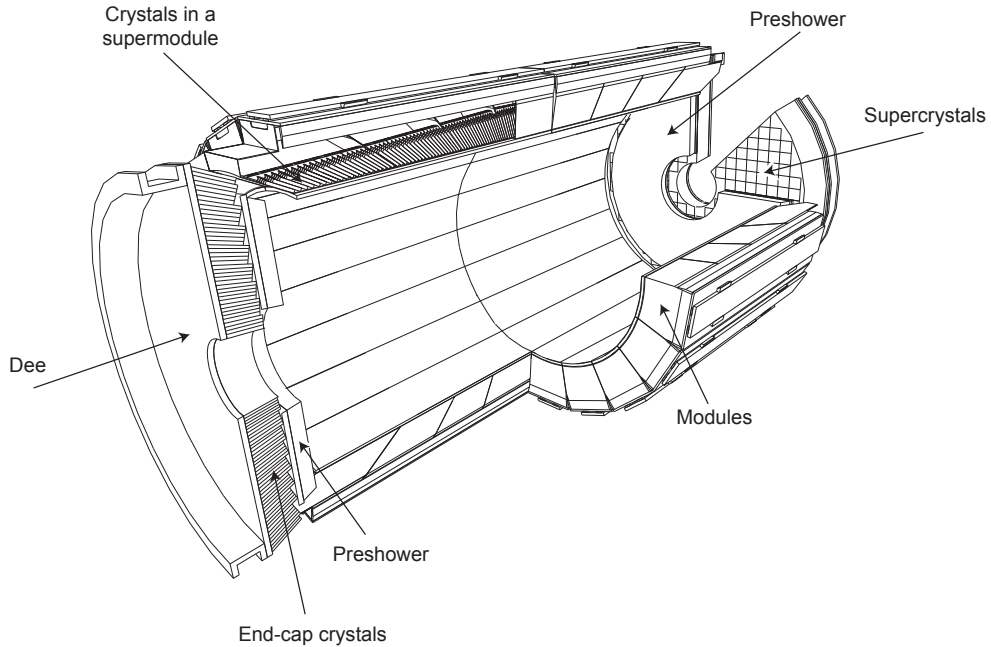


Figure 2.13: Layout of the ECAL detector. Reprinted from Fig. 4.5 of ref. [24].

511 initiates an electromagnetic (EM) shower. Due to the density, short radiation length,
 512 and small Molière radius of PbWO_4 , nearly the entirety of an EM shower can be
 513 contained in a single 23-cm long crystal with front face dimensions $2.2 \text{ cm} \times 2.2 \text{ cm}$.
 514 The crystals scintillate in the blue-green part of the spectrum, emitting $\sim 80\%$ of the
 515 scintillation light within 25 ns. Light is transmitted along the length of the crystals
 516 and collected at the rear with avalanche photodiodes (semiconductor diodes) in EB or
 517 vacuum phototriodes (conventional photomultipliers) in EE. Since the light output is
 518 low and varies with temperature, the crystals must be kept precisely at 18°C . The EB
 519 and EE crystals, which are slightly tapered to match the lateral shower development,
 520 are shown in Figure 2.14.

521 For each trigger, 10 samples, each separated by 25 ns, are read out. The 10-sample
 522 pulse is amplified and shaped by a multi-gain preamplifier (MGPA) residing on a very
 523 front end (VFE) card serving five crystals. The MGPA can switch between gains 1,
 524 6, and 12 to avoid saturation of the electronics, and affords a dynamic range up to

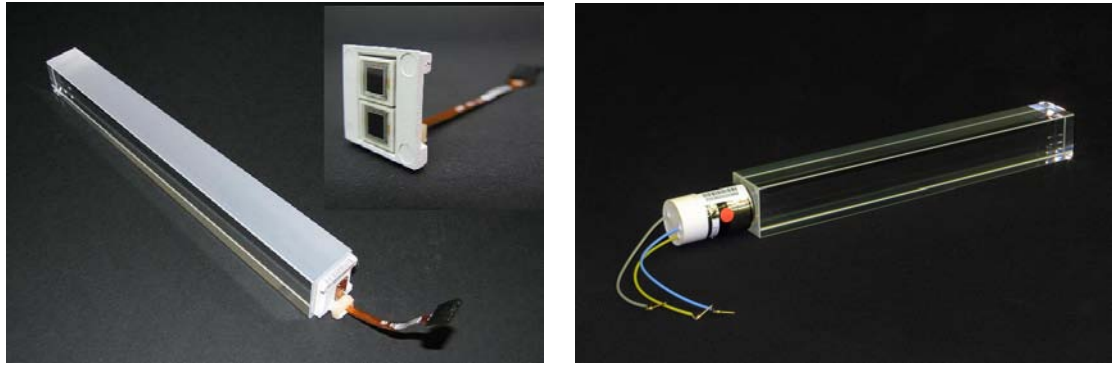


Figure 2.14: Left: EB crystal with attached APD. Right: EE crystal with attached VPT. Reprinted from Fig. 4.2 of ref. [24].

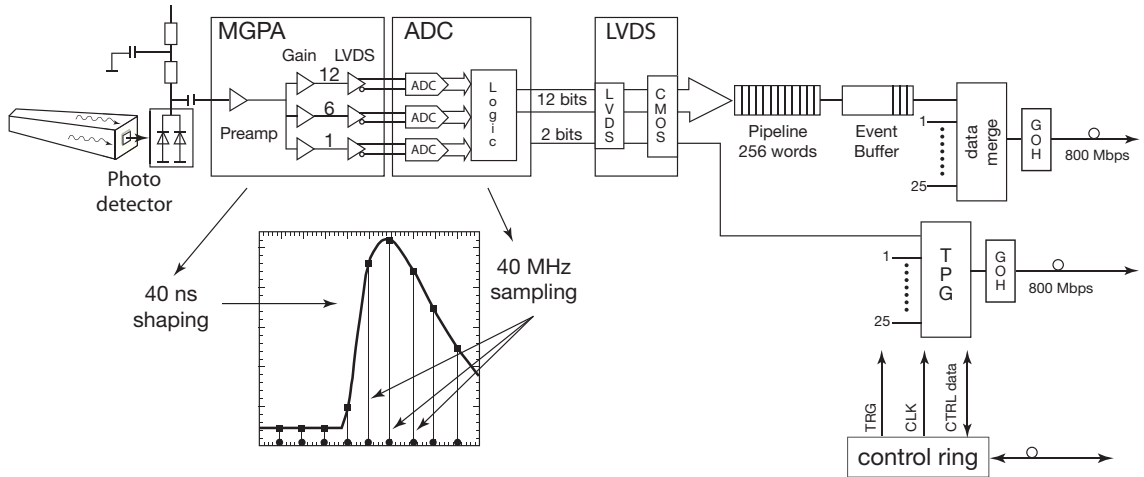


Figure 2.15: Flow chart of the crystal readout, showing the 10-sample pulse shape. Reprinted from Fig. 4.9 of ref. [24].

525 3 TeV. The samples are digitized on the VFE card, then sent to the front end (FE)
 526 card serving five VFEs. Digitized samples are buffered in the FE card until receipt
 527 of a trigger, when they are sent over an optical link to the data concentrator card
 528 (DCC) that interfaces to the global DAQ. The DCC interfaces to the *selective readout*
 529 processor, which decides whether a crystal should be read out with or without zero
 530 suppression based on its proximity to a high-energy hit. The clock is transmitted to
 531 the FE cards from the Clock and Control System (CCS) boards. A flow chart of the
 532 crystal readout is given in Figure 2.15.

533 At each bunch crossing, the trigger concentrator cards (TCC) of the ECAL com-
 534 pute *trigger primitives* from 5×5 non-overlapping transverse energy sums (in the
 535 endcaps the geometry is not always 5×5). This information, along with a special
 536 bit in EB only characterizing the transverse shower profile that is used for rejection
 537 of anomalous APD hits (see Sec. 3.1.1), is transmitted from the TCCs to the syn-
 538 chronization and link boards (SLBs), and then on to the global trigger system. The
 539 trigger decision is communicated to the DCCs, which request the buffered data from
 540 the front ends if the decision is affirmative.

541 Despite the radiation hardness of lead tungstate relative to other types of crystals,
 542 it still suffers from transparency loss due to radiation-induced lattice damage, as
 543 shown in Figure 2.16. In addition, any unforeseen change in the gains of the MGPAs
 544 and VPTs, or in the pedestal levels, will degrade the energy resolution. For this
 545 reason, a continuously running calibration system is installed with the ECAL. The
 546 system makes use of the LHC abort gaps to read out the pedestal levels, test pulses
 547 fired into the MGPAs, and laser (EB and EE) or LED (EE only) pulses fired into the
 548 crystals at regular intervals. Laser and LED events are used to compute corrections
 549 to the crystal gains for transparency loss, while the other types of calibration events
 550 serve to monitor changes in the electronics performance due to magnetic field or high
 551 voltage cycling. The mean time between transparency measurements is ~ 40 minutes.
 552 Figure 2.17 shows the architecture of the laser monitoring system.

553 The current ECAL energy resolution is somewhat worse than the design goal of
 554 0.5%. An incomplete understanding of (a) the transparency loss and (b) the photon
 555 conversion and electron bremsstrahlung processes in the $\sim 1X_0$ of tracker material in
 556 front of the ECAL are the main limiting factors in improving the resolution. However,
 557 as more data accumulate, more refined models of transparency loss and EM interac-
 558 tions in the tracker can be built, leading to better resolution. Energy resolution vs.
 559 $|\eta|$ can be seen in Figure 2.18.

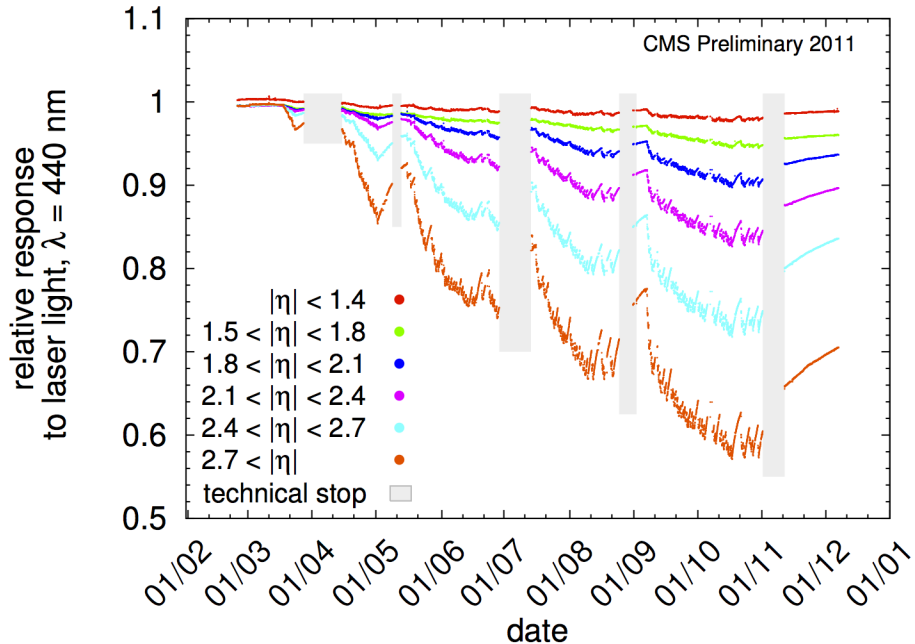


Figure 2.16: Relative response of the crystals to blue laser pulses from February 1, 2011 to January 1, 2012 [33]. Technical stops, during which the LHC is turned off for maintenance and development, are shown in gray. These periods of inactivity correspond to growth in the crystal response, as radiation damage recovery occurs.

560 The 10-sample readout coupled with the fast scintillation time of lead tungstate
 561 allows for a very precise reconstruction of the time of ECAL hits. ECAL timing is used
 562 for searches for long-lived particles that decay to photons or jets, such as long-lived
 563 neutralinos in GMSB [?]. Figure 2.19 shows the timing resolution in EE.

564 2.1.3 Hadronic Calorimeter

565 The CMS hadronic calorimeter (HCAL) has four parts: HCAL barrel (HB), HCAL
 566 endcap (HE), and HCAL outer (HO), which all utilize the same brass absorber /
 567 plastic scintillator sandwich technology; and HCAL forward (HF), which is a Čerenkov
 568 detector made of quartz fibers. A quarter longitudinal cross-sectional view of HCAL
 569 is shown in Figure 2.20. Like EB, HB is formed of 36 ϕ -wedges (18 cover 2π in positive
 570 η , 18 cover 2π in negative η). Each wedge is divided into 16 along η and four along
 571 ϕ , for a total of 64 readout towers per wedge (compare 1700 individually read out

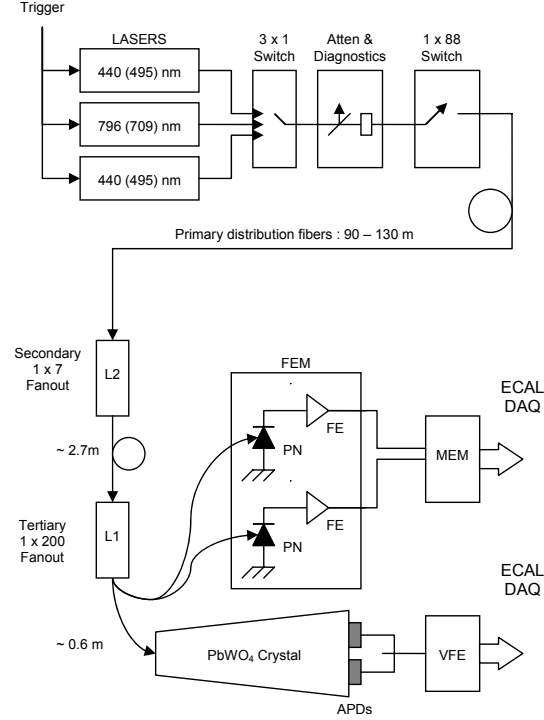


Figure 2.17: Architecture of the laser monitoring system. Reprinted from Fig. 4.16 of ref. [24].

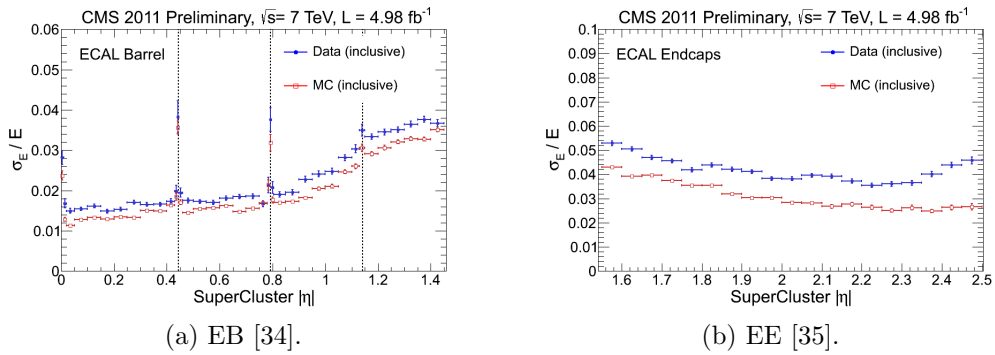


Figure 2.18: Energy resolution vs. $|\eta|$ for Z decay electrons for data (filled blue circles) and MC (empty red squares). The dotted lines show the locations of module gaps (three per SM).

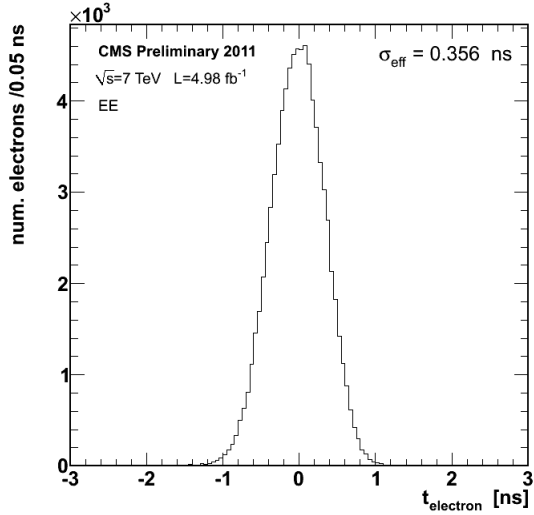


Figure 2.19: Distribution of reconstructed times of Z decay electrons in EE [36].

572 crystals per EB wedge). HE is divided into 36 ϕ -wedges containing 38 readout towers
 573 each. HO consists of five rings around HB and HE distributed symmetrically along z .
 574 There are 72 ϕ -slices per ring, with each ϕ -slice further divided into 5, 6, or 8 along
 575 z depending on ring. The HF fibers are distributed within the steel absorber. HF is
 576 divided into 18 ϕ -wedges per endcap side, each containing 24 readout towers. All HB
 577 towers have a single readout channel except for the two in each wedge at highest $|\eta|$,
 578 which are segmented into two longitudinal layers for readout. In HE, all towers have
 579 two longitudinal readout layers, except for the three rings of towers closest to the
 580 beam line, which have three. There are also two longitudinal depths of HF fibers.

581 HB, HE, and HO are all sampling calorimeters consisting of alternating layers of
 582 brass absorber and plastic scintillator. The absorber initiates the hadronic shower,
 583 and as shower particles travel through the scintillator the scintillation light is read
 584 out by wavelength-shifting (WLS) fibers connected to the scintillator tiles.² The full
 585 development of the shower is sampled by the layers of instrumented scintillator. The
 586 scintillator tiles are staggered so that there are no cracks in coverage along the direc-

²By contrast, in the ECAL, the crystal material acts as both absorber and scintillator, greatly reducing the contribution to energy resolution from sampling fluctuations.

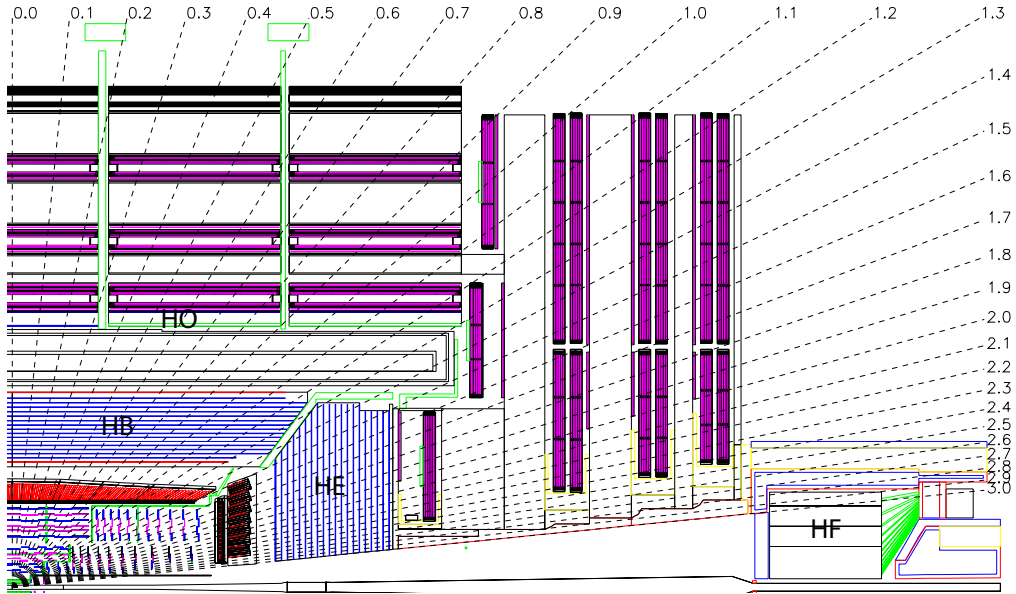


Figure 2.20: Quarter longitudinal cross-sectional view of HCAL (and muon stations in purple). Reprinted from Fig. 5.1 of ref. [24].

tion projected back to the beam spot. Light output from all tiles in a single readout tower is collected via the WLS fibers and merged into a single signal that is amplified by a hybrid photodiode (HPD). A diagram of the optical readout of HB (similar for HE and HO) is shown in Figure 2.21.

Due to the extremely harsh radiation environment near the beam line, HF is constructed of a 1.2-m thick, 1.7-m long ring of steel absorber with radiation hard quartz fibers distributed within the steel and running parallel to the beam line. Hadronic showers develop in the steel and are sampled in the quartz fibers when charged shower particles hit the the fibers and emit Čerenkov light. The light is transmitted by total internal reflection down the fibers to a photomultiplier tube (PMT), where the signals from all fibers in an HF tower are merged into one. Since only relativistic particles emit Čerenkov light in these fibers, it is mostly the EM component of the hadronic shower, consisting of neutral pions decaying to photons that interact electromagnetically with the absorber, that is sampled [37]. The charged hadrons produced in hadronic showers are typically too slow to generate Čerenkov light. Figure 2.22

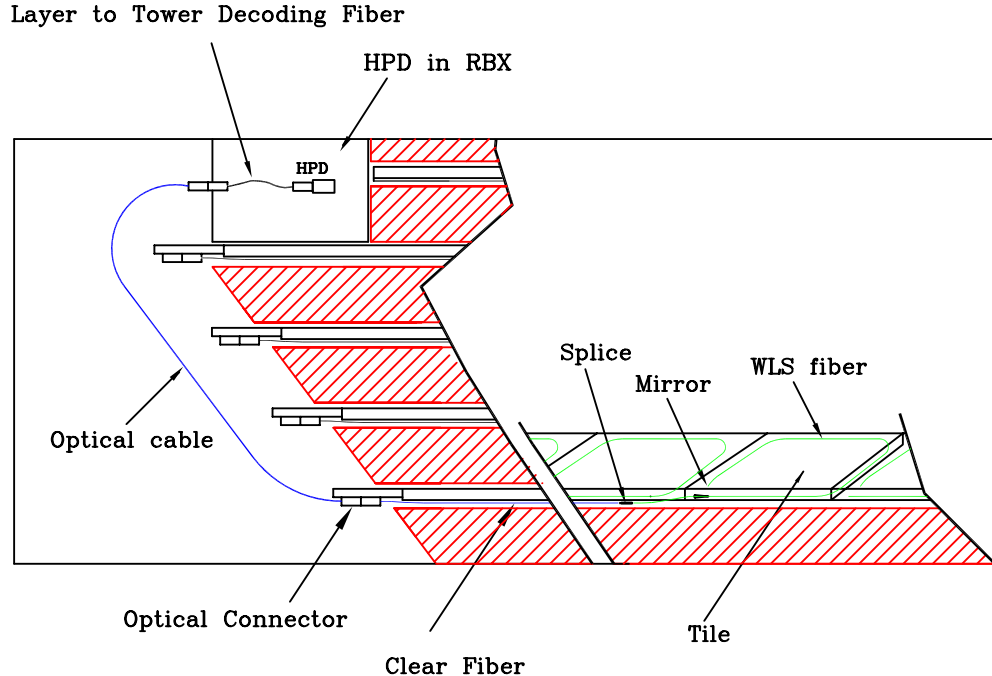


Figure 2.21: Diagram of the optical readout of HB. Reprinted from Fig. 5.7 of ref. [24].

602 shows a cross-sectional view of one side of HF.

603 Electrical signals from either HPDs (HB/HE/HO) or PMTs (HF) are digitized on
 604 the front ends by means of a fast charge-integrating ADC. The digitized signals are
 605 sent off-detector to the HCAL Trigger/Read-Out (HTR) boards, where they await a
 606 trigger decision. If the trigger is accepted, the signals are sent on to the HCAL data
 607 concentrator cards (DCCs), which interface to the global DAQ system. HCAL trigger
 608 primitives, consisting of transverse energy sums over an entire tower, are calculated
 609 in the HTR boards and sent to the global trigger system.

610 Selected HCAL performance results can be seen in Figure 2.23.

611 2.1.4 Muon System

612 Beginning at a radius of ~ 10 interaction lengths from the beam line, where all parti-
 613 cles except muons should have been stopped by the HCAL, are the muon chambers,
 614 interspersed with the iron return yoke of the CMS magnetic field. Three technologies

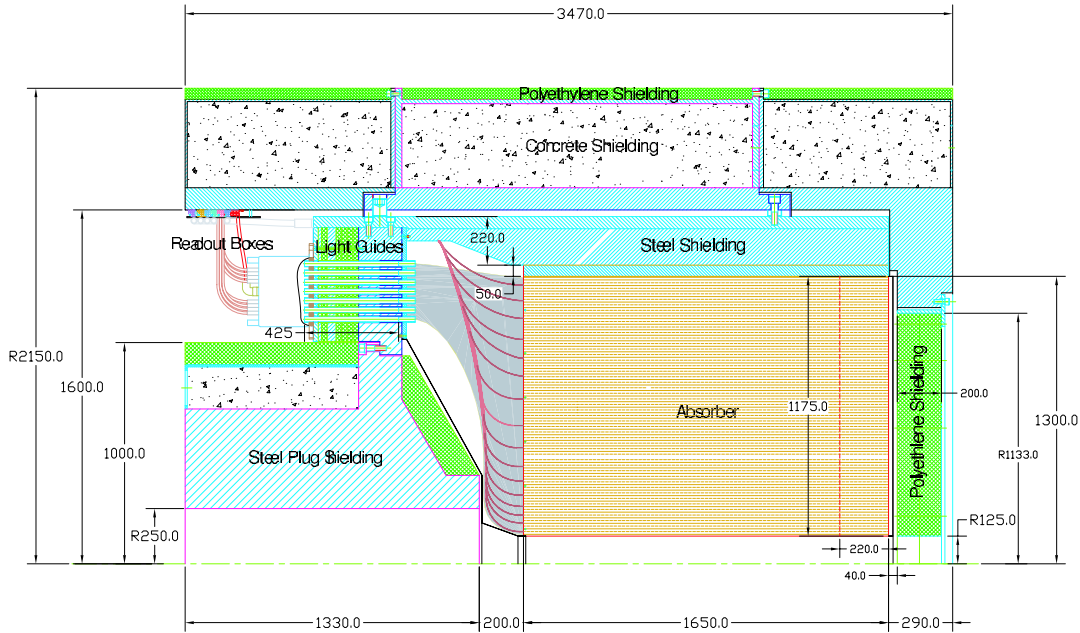
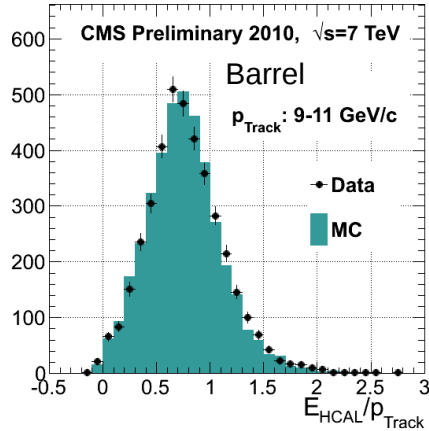


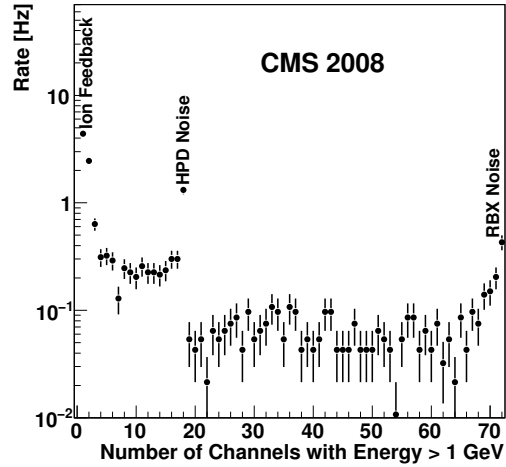
Figure 2.22: Cross-sectional view of one side of HF. The z -axis is horizontal. Reprinted from Fig. 5.28 of ref. [24].

615 are employed: drift tubes in the barrel section (MB), cathode strip chambers (CSCs)
 616 in the endcap section (ME), and resistive plate chambers (RPCs) in both sections to
 617 provide an independent trigger with superior time resolution. There are four barrel
 618 layers of stations extending out to $|\eta| = 1.2$. Each endcap consists of five disks of
 619 stations as shown in Figure 2.24b, covering $1.4 < |\eta| < 2.4$. RPCs populate the barrel
 620 and endcap muon systems alongside the DT chambers and CSCs. Since they have
 621 time resolution much better than a few ns, they are used to assign the bunch crossing
 622 of muon tracks and provide a p_T trigger with sharp turn-on.

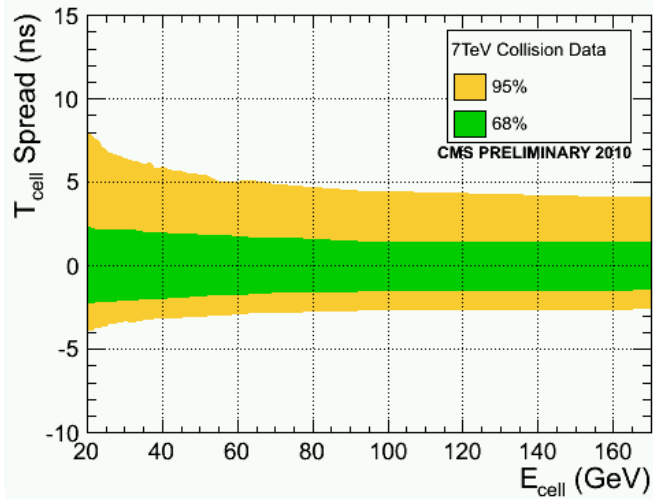
623 Each DT chamber consists of two $r \cdot \phi$ superlayers (SLs) and optionally one z
 624 SL (in all chambers except those in the fourth layer). The SLs contain four rows of
 625 drift tubes, with the rows staggered such that there are no gaps in the coverage. The
 626 $r \cdot \phi$ SLs have the tube axis parallel to the beam line, while the z SL is perpendicular
 627 to the beam line. The tubes are ~ 2.4 m in length and $13 \text{ mm} \times 42 \text{ mm}$ in cross
 628 section. Each chamber therefore records eight $r \cdot \phi$ tracking points and optionally four



(a) Data/MC comparison of HB response to charged tracks of 9-11 GeV/c momentum [38].

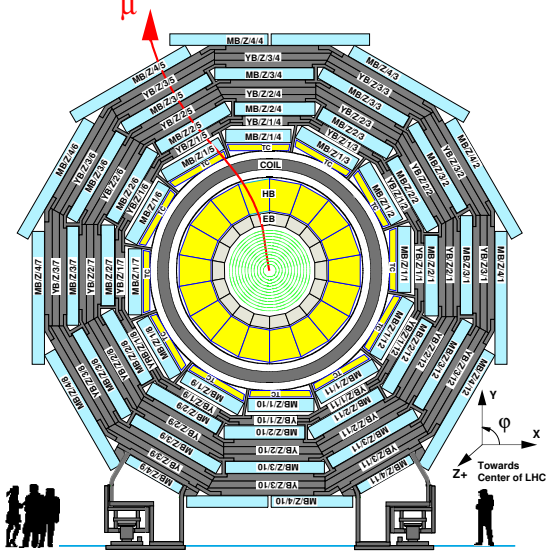


(b) Distribution of tower multiplicity, clearly showing three peaks in rate corresponding to noise sources (see Sec. 3.3) [78].

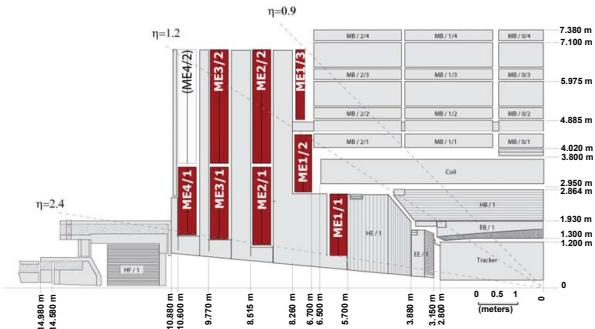


(c) Timing resolution vs. tower energy [38].

Figure 2.23: Selected HCAL performance results.



(a) One of the five wheels of MB, showing the four layers of muon stations. The five wheels are spaced symmetrically in z about $z = 0$. As a muon traverses the muon detectors, its curvature in the transverse plane changes direction and magnitude due to the magnetic field in the return yoke, which is of opposite sign and reduced strength relative to the field within the solenoid volume. Reprinted from Fig. 7.3 of ref. [24].



(b) Quarter longitudinal cross section of CMS highlighting the location of the ME disks. Reprinted from Fig. 7.47 of ref. [24].

Figure 2.24: View of the MB and ME layout in CMS.

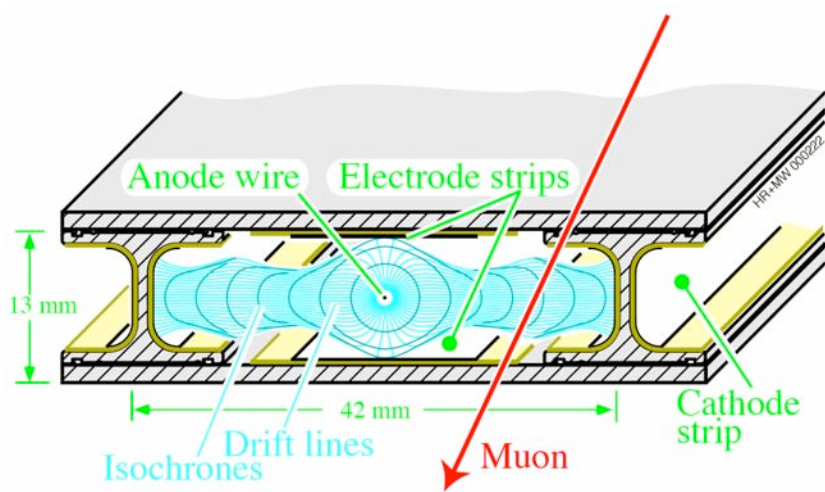


Figure 2.25: Electric field lines within a drift tube as well as the contours of equal drift time. Reprinted from Fig. 7.5 of ref. [24].

629 z tracking points. The tubes are filled with an 85%Ar + 15% CO₂ gas mixture. An
 630 anode wire at 3600 V runs the length of the tube, while the walls are covered with
 631 electrodes held at 1800 V or -1200 V depending on wall. When a muon passes through
 632 the tube, it ionizes the gas atoms. The liberated electrons drift along the electric field
 633 lines created by the electrodes to the anode, which is read out. Figure 2.25 shows
 634 the electric field lines within a drift tube as well as the contours of equal drift time.
 635 The maximum drift time is 380 ns.

636 CSCs consist of alternating layers of cathode strips (four planes oriented along r)
 637 and anode wires (three planes oriented along ϕ). A 40%Ar + 50%CO₂ + 10%CF₄ gas
 638 mixture fills the space between two successive planes, forming six gas gaps. When a
 639 muon ionizes the gas atoms, the positive ions drift toward the anode and are read
 640 out to provide a measurement of r , just as in the DTs. However, an image charge is
 641 induced on the cathode strips, which is also read out to provide a measurement of ϕ .
 642 The wires are spaced 3.2 mm apart. The cathode strips have pitch varying from 8.4
 643 mm at the end closest to the beam line to 16 mm at the other end, and are spaced
 644 0.5 mm apart. A trapezoidal CSC is shown in Figure 2.26.

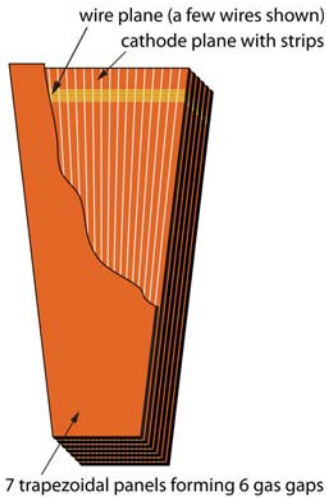


Figure 2.26: CSC wedge, showing the cathode and wire planes. Reprinted from Fig. 7.49 of ref. [24].

645 Track stubs from the muon system are combined with tracks from the tracking
 646 system to form more precise muon tracks than either system could form alone, as
 647 shown in Figure 2.27. This leads to extremely good di-muon invariant mass resolution
 648 (Figure 2.28) over a large p_T range.

649 **2.2 Triggering, Data Acquisition, and Data Trans-** 650 **fer**

651 **2.2.1 Level 1 and High Level Trigger Systems**

652 The Level-1 (L1) trigger system, which encompasses dedicated hardware processors
 653 to construct trigger objects (typically high p_T jets, electrons, photons, taus, and
 654 muons) out of the calorimeter and muon hits, distributes a L1 accept or reject to all
 655 subdetectors at the LHC bunch crossing frequency of 40 MHz. Further data filtering
 656 is performed by the High Level Trigger (HLT) system, a farm of ~ 1000 commercially
 657 available processors running a slimmed down version of the CMS event reconstruction

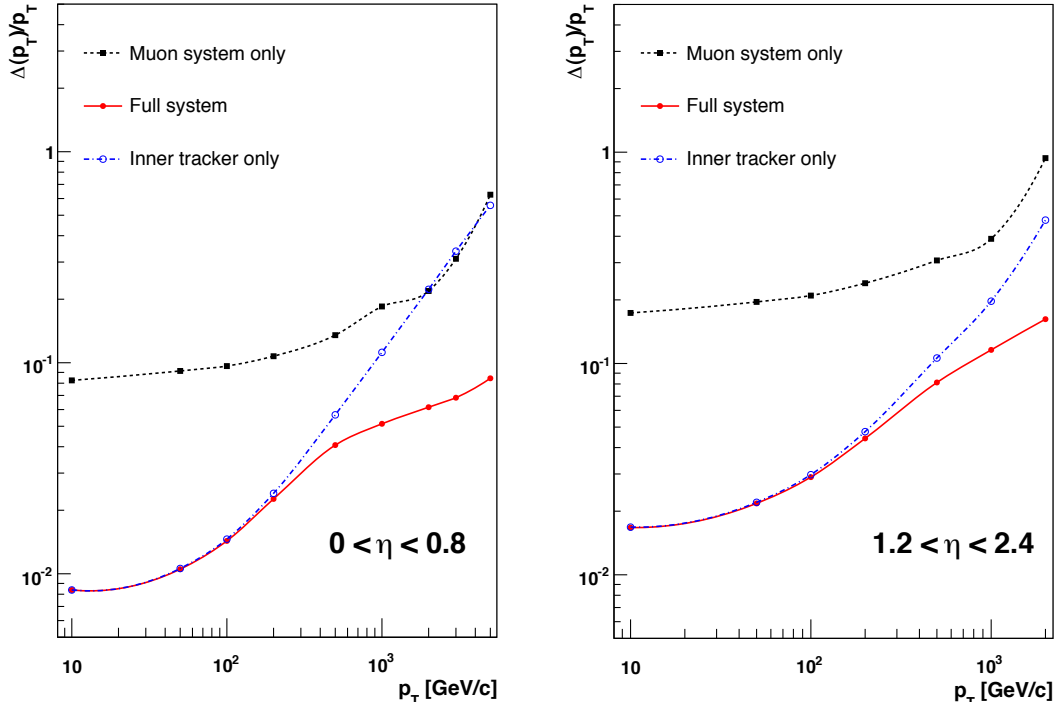


Figure 2.27: Muon p_T resolution as a function of muon p_T for tracker information only (blue), muon information only (black), and both tracker and muon information combined (red). Reprinted from Fig. 1.2 of ref. [24].

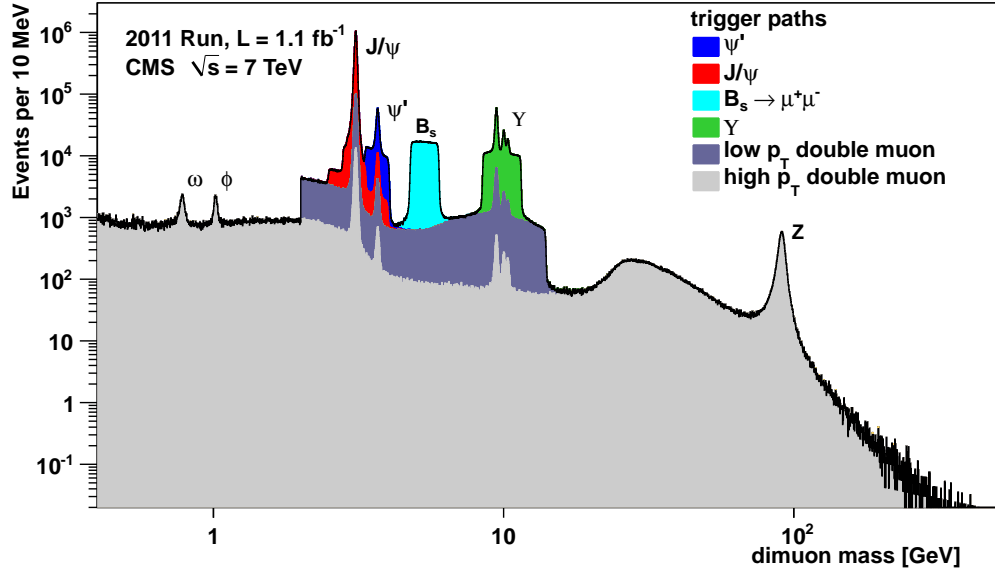


Figure 2.28: Di-muon invariant mass spectrum broken down by trigger path [39]. The light(dark) gray regions show the contribution from high- p_T (low- p_T) di-muon triggers. Note that no $B_s \rightarrow \mu^+\mu^-$ decays have been observed [40]; the light blue region just shows the amount of triggers dedicated to the $B_s \rightarrow \mu^+\mu^-$ search.

software CMSSW. The data rate received by the HLT is ~ 100 kHz; the output rate of events permanently written to disk is ~ 100 Hz. An L1 trigger *latency* (time between the collision and the distribution of the L1 decision to the subdetectors) of $3.2\ \mu\text{s}$ is achieved via the use of fast electronics and sufficiently deep buffers to pipeline trigger primitives waiting to be analyzed. This latency corresponds to the length of the LHC abort gap, so in principle CMS may be operated with zero *dead time* (during which LHC bunches are missed because the L1 system is blocked while processing other triggers).

At the bottom, the L1 trigger consists of trigger primitive generators (TPGs) in the calorimeter and muon systems that send E_T sums or muon track stubs to the regional calorimeter trigger (RCT) or muon track finders, respectively. The RCT, DT track finder (DTTF), and CSC track finder (CSCTF) sort and rank the regional trigger primitives based on p_T and quality. The ranked RCT candidates and muon track stubs are sent to the global calorimeter trigger (GMT) and global muon trigger (GMT), respectively, where high-level objects like isolated and non-isolated muons and EM candidates, jets, taus, and \cancel{E}_T are constructed from all the regional inputs and ranked. Calorimeter isolation sums for muons are also sent from the RCT to the GMT. The highest ranked global objects are sent to the global trigger (GT), which sits at the top of the L1 trigger. The GT issues the final L1 accept or reject to all subdetectors based on a comparison of the GMT and GCT candidates with the requirements of its programmed trigger menu. A block diagram of the L1 trigger is shown in Figure 2.29.

A region in the RCT consists of a matrix of 4×4 trigger towers. A trigger tower in EB/HB is one HCAL tower + the 5×5 matrix of ECAL crystals in front of it; in EE/HE the idea is similar but the counting of crystals and HE towers is slightly more complicated. An EM RCT candidate is built around a high E_T seed tower. The E_T of the candidate is the sum of the tower E_T and the E_T of its highest- E_T

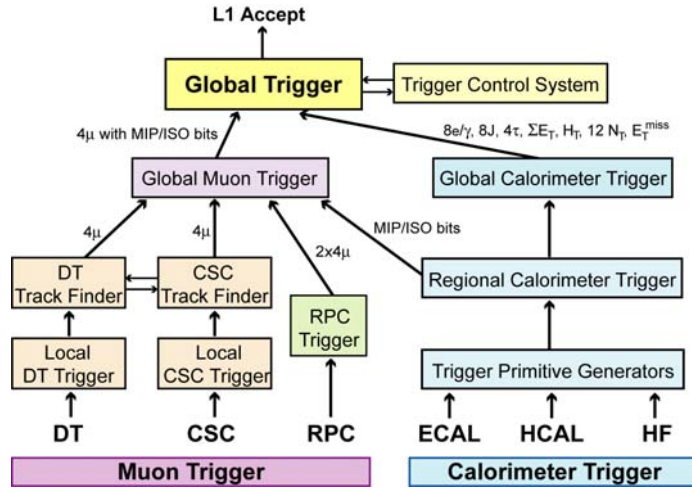


Figure 2.29: Block diagram of the L1 trigger. Reprinted from Fig. 8.1 of ref. [24].

685 broad side neighbor (see Figure 2.30 for a definition of the broad side neighbors). Two
 686 isolation criteria are defined based on (a) the ratio of the EM energy to the HCAL
 687 energy in the tower and (b) the shower shape. For a non-isolated EM candidate, the
 688 highest- E_T broad side neighboring tower must pass these two isolation criteria; for
 689 an isolated EM candidate, all eight neighboring towers must the criteria, and there
 690 must also be at least one quiet corner with the E_T of all five towers in the corner
 691 below some threshold (see Fig. 2.30). The process is repeated until four isolated and
 692 four non-isolated EM candidates are found, starting with the highest- E_T tower in the
 693 region and moving down in tower E_T . An RCT region is flagged as consistent with
 694 tau decay only if the pattern of tower transverse energy sums defines at most a 2×2
 695 matrix of energetic towers within the 4×4 RCT region.

696 From the tower transverse energy sums, eight EM candidates, and tau flag received
 697 from each RCT, the GCT computes the total E_T in the calorimeter (and the total E_T
 698 above some programmable threshold, called H_T), and the \cancel{E}_T . It also classifies the
 699 towers into jets and determines the globally highest ranked isolated and non-isolated
 700 EM candidates. The jet finding uses a clustering algorithm based on the energy of a
 701 sub-cluster with respect to its neighbors [41]. Jets are classified as tau decays if all

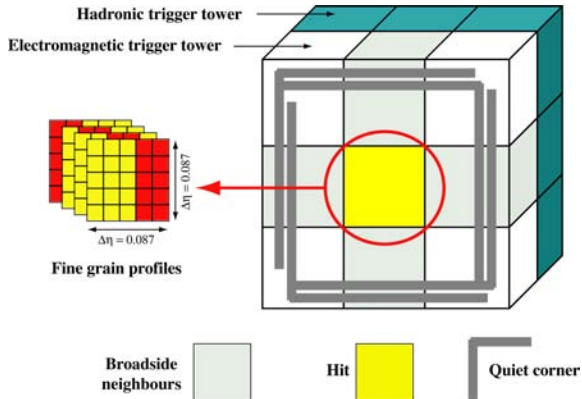


Figure 2.30: Geometry of an EM RCT candidate. Reprinted from Fig. 8.2 of ref. [24].

of the RCT regions participating in the jet clustering had energy patterns consistent with tau decay. Counts of jets above 12 different programmable E_T thresholds are calculated. The jet counts, energy sums, E_T , and highest ranked EM candidates are sent to the GT, where the final L1 decision is taken and transmitted to the subdetectors. The GT can execute a maximum of 128 trigger algorithms in parallel. If any one of these algorithms yields an accept, the event is accepted, and all trigger information is sent on to the HLT for further filtering. The double-photon HLT paths used in this analysis (see Sec. 3.2) require isolated L1 seeds (i.e. EM candidates built by the RCT) with $E_T > 12$ or 20 GeV, depending on path.

No muon triggers are used in the two-photon analysis. A description of the muon trigger system can be found in ref.[24].

2.2.2 Data Acquisition System

The CMS data acquisition (DAQ) system takes event fragments (calorimeter hits, track hits, etc.) from each of the 626 subdetector front end drivers (FEDs), assembles them into a data structure representing the full event, and sends the event on to the HLT for further filtering. The DAQ must operate at an input rate of ~ 100 GB/s, corresponding to an input rate from the L1 trigger of ~ 100 kHz. To facilitate

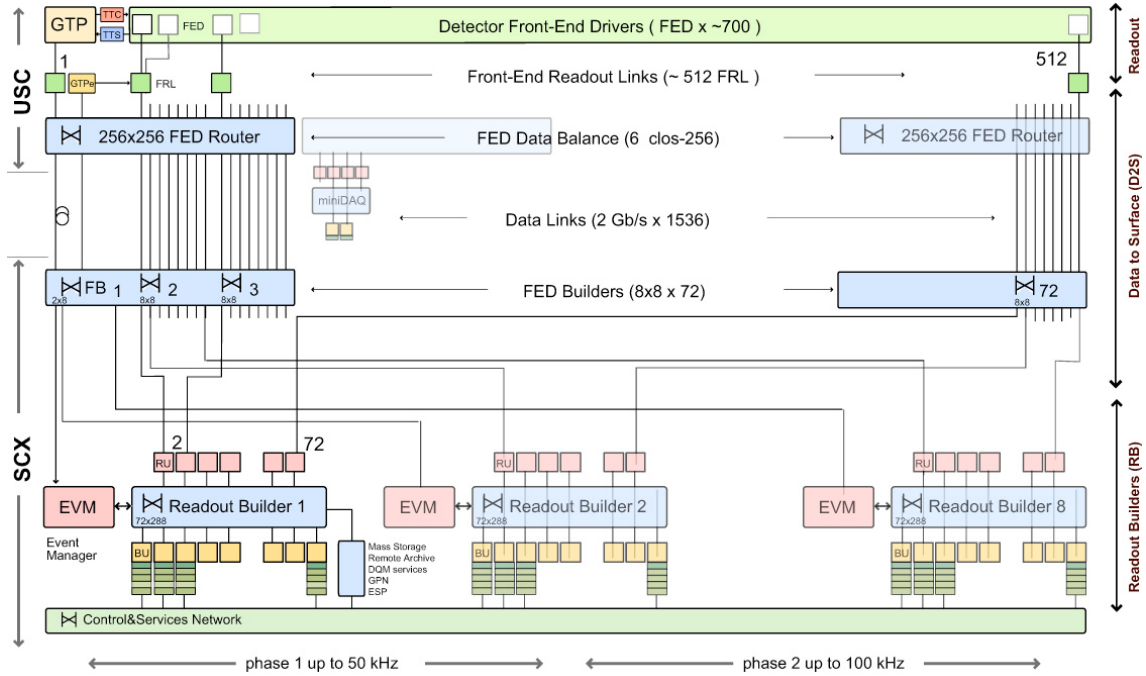


Figure 2.31: Diagram of the DAQ system. The identical event builder systems, shown as inputs and outputs to the boxes labeled “Readout Builder 1”, “Readout Builder 2”, etc., represent the eight slices. Within one slice, data can flow from the detector front ends to the readout systems to the builder network (which assembles the event fragments) to the filter systems (HLT) independently of the other slices. Reprinted from Fig. 9.8 of ref. [24].

719 expansion of the system as the need arises, the DAQ is composed of eight nearly
 720 independent slices. Each slice functions as a smaller version of the whole DAQ that
 721 can handle an input event rate up to ~ 12.5 kHz. A diagram of the DAQ system,
 722 showing schematically the eight slices, is given in Figure 2.31.

723 Data from the front ends is collected by the FEDs and pushed to the front end
 724 readout links (FRLs), which may take inputs from up to two FEDs simultaneously.
 725 The FRLs check for transmission errors, generate event fragments with size ~ 2 kB,
 726 buffer the fragments in 64 kB memories, and finally send them to the FED builders.
 727 The FEDs, FRLs, and FED builders are located in the underground control room.
 728 The 72 FED builders each construct one ~ 16 kB *super-fragment* from the input
 729 event fragments, then send the super-fragment on to a readout unit (RU) located in

730 the surface control room ~ 80 m away. Super-fragments belonging to the same event
 731 are sent to RUs in the same DAQ slice. There are 72 RUs per readout builder, one
 732 for each super-fragment of an event, with each DAQ slice built around one readout
 733 builder (see Fig. 2.31). Each readout builder hosts a number of builder units (BUs)
 734 that perform the final integration of super-fragments into complete events.

735 Resource brokers (RBs) in the HLT filter farm request complete events from the
 736 BUs and distribute those events to the filter units (FUs) for HLT selection. If an
 737 event passes any one of the HLT paths in the predefined menu, it is sent back to
 738 the RB for transfer to the storage manager (SM). The SM nodes transfer accepted
 739 events to the CERN Tier-0 prompt reconstruction facility for unpacking of the raw
 740 data into ROOT [42] files that can be accessed by physicists wishing analyze the data.
 741 The lag time between recording of an event in the DAQ and availability of the fully
 742 reconstructed event for analysis is typically 48 hours.

743 If the buffers of the upstream DAQ elements (the filter farm, readout builders,
 744 FED builders, or FRLs) are full, those elements will not request new events from
 745 downstream. This can lead to a buildup of events in the downstream element buffers,
 746 *back-pressuring* all the way down to the FEDs themselves. The CMS trigger throttling
 747 system (TTS) consists of dedicated lines between the FEDs and the GT for the
 748 purpose of sending predefined signals to the GT about the state of the FED buffers.
 749 If the buffer of a particular FED is getting full, it can alert the GT to reduce the
 750 trigger rate so as to prevent FED buffer overflows and loss of time synchronization
 751 between event fragments. The TTS latency is $\sim 1\mu\text{s}$. Causes of back-pressure (hence
 752 dead time) include: problems with the FED electronics (in this case, the upstream
 753 elements request events but the FEDs have trouble sending them), increases in the
 754 L1 accept rate (perhaps due to a noisy detector channel) beyond what the upstream
 755 DAQ elements can handle, increases in the event size due to high pileup or a poor
 756 quality beam that scrapes against the beam pipe, failures of the DAQ transmission

757 lines or DAQ hardware such that events are not requested from the FEDs fast enough,
 758 or bottlenecks at the SM nodes or filter farm due to hardware failures or large event
 759 sizes.

760 All components of the DAQ, from the FEDs up to the SMs, are controlled by
 761 cross-platform DAQ (XDAQ) [43] processes, or *executives*. The Simple Object Access
 762 Protocol (SOAP) [44] protocol is used to transmit control and monitoring data be-
 763 tween XDAQ-enabled devices and to the end user, who can view the running of a
 764 XDAQ executive via a Web interface called HyperDAQ [45]. The Run Control and
 765 Monitoring System (RCMS) handles the configuration and control of all XDAQ exec-
 766 utives via a hierarchical structure. At the top of the hierarchy is the Level-0 *function*
 767 *manager* (FM), controlling the Level-1 sub-detector FMs, which in turn control their
 768 Level-2 system-specific XDAQ executives. The central DAQ and L1 trigger each have
 769 their own Level-1 FM. A unit of data acquisition, called a *run*, may be configured,
 770 started, and stopped by an end user interacting with the RCMS Web interface.

771 2.2.3 Data Processing and Transfer to Computing Centers

772 Data leaving the filter farm are grouped into datasets based on HLT path, i.e. there
 773 are different datasets for events passing diphoton triggers, jet triggers, muon + elec-
 774 tron triggers, etc. At the Tier-0 facility, the datasets are go through three levels of
 775 processing to create three *data tiers*. The first layer produces RAW data by unpack-
 776 ing the detector byte streams sent from the DAQ and L1 trigger into data structures
 777 holding the ADC counts recorded for each channel of the detector, digitized trigger
 778 primitives, and the L1 decision. A single event has ~ 1.5 MB of RAW data. The next
 779 layer of processing is the reconstruction, which forms channel energies in GeV, ap-
 780 plies calibrations, and creates high-level objects like photons, electrons, muons, taus,
 781 jets, E_T , and charged tracks. The RECO data tier occupies ~ 0.5 MB per event.
 782 Finally, analysis object data (AOD) is a subset of the RECO data, comprising the

783 high-level objects but usually excluding the individual channel hit information if it is
784 not associated to a physics object. This tier occupies ~ 0.1 MB per event. One copy
785 of the RAW data is stored permanently at CERN and another copy is distributed
786 amongst the Tier-1 facilities (see below) for permanent storage. Changes in the re-
787 construction algorithms periodically require reprocessing of the RAW data to form a
788 new RECO tier. In general, only the AOD tier is available to physicists wishing to
789 perform analyses due to the smaller size and faster replication and transfer time of
790 AOD with respect to RAW or RECO.

791 There are three tiers of computing and data storage sites within the Worldwide
792 LHC Computing Grid (WLCG) [46]. The tier closest to CMS is Tier-0, which is
793 located at CERN and performs archiving of the RAW data, prompt reconstruction
794 of the data within ~ 48 hours of its being collected, and transferral of copies of the
795 RECO datasets to Tier-1 facilities. There are a few Tier-1 centers worldwide, hosted
796 by national computing facilities and laboratories. They store parts of the RAW dataset
797 and copies of the RECO datasets, participate in subsequent reconstruction passes
798 after the prompt reconstruction at Tier-0, and ship AOD datasets upon request to the
799 Tier-2 centers. Analysts interact primarily with the Tier-2 centers, which store AOD
800 datasets and run batch processing queues for running analysis jobs over the datasets.
801 Different layers of WLCG software control data transfer between sites, data storage,
802 and batch processing. A diagram of the WLCG tier system is given in Figure 2.32.

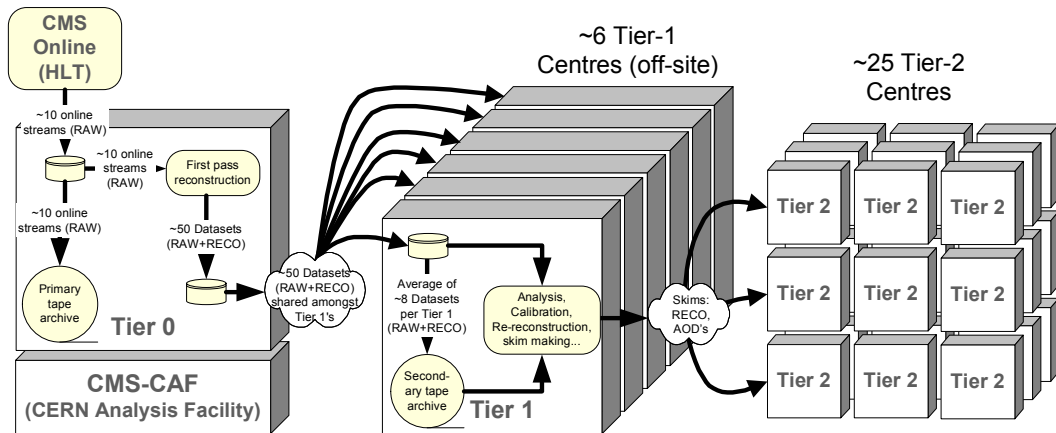


Figure 2.32: Diagram of the WLCG tier system showing data archival and reconstruction at each tier along with data transfer between tiers. Reprinted from Fig. 11.2 of ref. [24].

803 **Chapter 3**

804 **Event Selection**

805 In keeping with the phenomenology described in Sec. 1.5, the candidate GGM events
806 selected in this search consist of two high- E_T photons and a significant momentum
807 imbalance transverse to the beam, indicating the production of an escaping gravitino.
808 This momentum imbalance is usually referred to as *missing transverse energy* and is
809 denoted by the symbol \cancel{E}_T .

810 However, in order to use real CMS data (as opposed to simulation) to derive pre-
811 dictions for the backgrounds to the search, *control samples* distinct from the *candidate*
812 two-photon sample must be collected. These samples consist of different numerical
813 combinations of photons, electrons, and jets, and are explained in more detail in
814 Chapter 4. Since this search is performed in the high- \cancel{E}_T tail of the \cancel{E}_T distribution,
815 where adequate detector simulation is very difficult, it is advantageous to use *data-
816 driven* background estimates, which capture the true detector response, over numbers
817 derived from simulation.

818 In the following sections, the reconstruction of photons, electrons, jets, and \cancel{E}_T
819 is explained. Sec. 3.1 begins with an explanation of the high level reconstruction.
820 It is followed by Sec. 3.2, which describes the triggers used to collect the candidate
821 and control samples. Sec. 3.3 describes event cleaning cuts that are applied to the

822 candidate and control samples. Finally, the chapter concludes with a measurement of
823 the photon identification efficiency in Sec. 3.4.

824 3.1 Object Reconstruction

825 This section describes the *offline* object reconstruction, i.e. the reconstruction of par-
826 ticle objects from events that have already been triggered and written to permanent
827 storage, as opposed to the building of trigger objects explained in Secs. 2.2.1 and 3.2.

828 3.1.1 Photons

829 Uncalibrated EB/EE Hits

830 Photon reconstruction begins with the ADC count value for each of the 10 recorded
831 time samples per ECAL crystal per trigger. To construct an *uncalibrated hit*, the
832 gain (1, 6, or 12; see Sec. 2.1.2) of each sample is determined and the ADC count
833 value scaled appropriately. The pedestal is estimated from the average of the first
834 three samples, which, for a properly timed in hit, should contain no signal. This
835 pedestal value is subtracted from the rest of the samples. Finally, the amplitude of the
836 pulse is reconstructed using a predetermined weight for each sample [47]. The weights
837 correspond to the pulse shape expected from the MGPA and shaping circuit response.
838 The time of the hit is also reconstructed using the ratios between neighboring time
839 samples [48]. A typical ECAL channel pulse shape is shown in Figure 3.1.

840 Calibrated EB/EE Hits

841 In the next phase of the photon reconstruction, calibrations are applied to the un-
842 calibrated hits to form *calibrated hits* with energy measured in GeV. Channels are
843 excluded from seeding calibrated hits if

- 844 • they are excessively noisy,

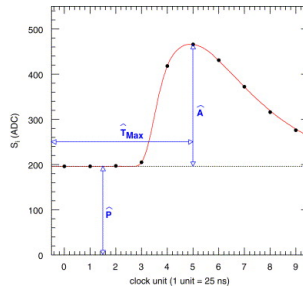


Figure 3.1: Typical ECAL channel pulse shape. \hat{P} is the pedestal value, \hat{A} is the pulse amplitude, and \hat{T}_{\max} is the hit time. The red line is the assumed pulse shape from which the weights are derived. Reprinted from ref. [47].

- 845 • they are stuck in fixed gain (i.e. the MGPA gain does not change properly to
846 avoid saturation),
- 847 • they are totally dead,
- 848 • they have one or more neighboring dead channels, or
- 849 • they do not have good trigger primitives (i.e. trigger primitive is missing, satu-
850 rated, or *spike-like*).

Added

851 *ECAL spikes* are hits in which low energy protons and heavy ions from jets ionize this
852 in the sensitive volume of the EB APD, causing the APD to register a fake large- para-
853 amplitude hit. Because they are not the result of a real electromagnetic shower, spikes graph
854 tend to be isolated. They may also appear to arrive early or late with respect to the and the
855 nominal bunch crossing. Most spikes are reconstructed with a hit time ~ 10 ns earlier next
856 than real EM hits because unlike real hits, whose pulse shapes include the time about
857 constant associated with crystal scintillation, the reconstructed spikes only involve spikes
858 the rise time of the electronics. There also is a long tail of late arriving spikes due to
859 slow neutrons from jets [49].

860 Because of their particular timing and topological characteristics, cuts have been
861 developed to effectively identify and reject spike-like hits. This analysis utilizes both
862 the “Swiss cross” cut $1 - E_4/E_1 > 0.95$, where E_1 is the energy of the spike candidate

863 crystal and E_4 is the sum of the energies in the four crystals whose edges are parallel to
 864 the four edges of the spike candidate crystal, and a timing cut $t \geq 3$ ns, to flag spikes.
 865 More information about these cuts can be found in ref. [49]. A simpler algorithm
 866 using the fine grain veto bit of the L1 TPG is used to reject spikes at the trigger level
 867 **[insert citation]**.

868 In addition to the trigger primitives, no uncalibrated hits that are spike-like are eli-
 869 gible for calibration. The calibrations applied are crystal transparency loss corrections
 870 measured continuously by the laser/LED system, energy intercalibrations (relative en-
 871 ergy calibration between crystals), absolute scale calibrations between ADC counts
 872 and GeV,¹ and time intercalibrations (relative time calibration between crystals).

873 The ECAL crystals were pre-calibrated before installation in CMS using labora-
 874 tory light yield and photodetector gain measurements [51]. In addition, some EB and
 875 EE crystals were intercalibrated using test beams [52], and all EB crystals were inter-
 876 calibrated with cosmic ray muons [53]. EE precalibrations were validated with LHC
 877 *splash events* in 2009 [53, 54], in which the beam was dumped onto a collimator ap-
 878 proximately 150 meters upstream of CMS, causing a spray of muons to enter CMS at
 879 one endcap and exit at the other. Splash events were also used to derive time intercal-
 880ibration constants. Before colliding beam operations commenced, the intercalibration
 881 precision was estimated to be 0.5%-2.2% in EB and 1%-5% in EE [55].

882 Three calibration methods were employed once colliding beam operations began:

- 883 • ϕ symmetry relative calibration between crystals, exploiting the azimuthal sym-
 metry of CMS
- 885 • π^0 and η relative calibration between crystals, using the diphoton decays of
 these particles

¹The ADC-GeV scale factors (one for EB and one for EE) are defined such that the sum of fully calibrated and scaled hits in a particular 5×5 cluster of crystals (plus the associated energy deposited in ES) is 50 GeV for a 50 GeV incident unconverted photon [50].

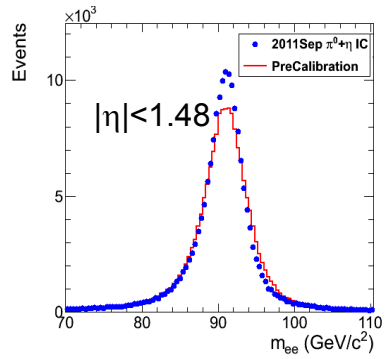


Figure 3.2: Z peak reconstructed using pre-LHC calibration constants (red) or September 2011 π^0/η -derived intercalibration constants (blue). Reprinted from ref. [56].

887 • E/p absolute calibration, comparing the momentum measured in the tracker p
 888 to the energy measured in the ECAL E of a sample of electrons from Z decay

889 By September 2011, the intercalibration precision in EB was measured to be be-
 890 tween 0.3% and 1.1% using the π^0/η method [56]. Figure 3.2 shows the improvement
 891 in Z reconstruction from pre-LHC calibration constants to the latest π^0/η -derived
 892 constants.

893 **Calibrated ES Hits**

Added

894 ES calibrated hits are formed from the three samples read out per sensor. Just as in the paren-
 895 case of EB/EE crystals, ES uncalibrated hits gain-adjusted, pedestal-subtracted, and thetical
 896 reconstructed using weights. To make a calibrated ES hit, intercalibration constants, remark
 897 angle correction constants (for the non-uniformity of sensor angle with respect to the
 898 vertical across ES), and a MIP-GeV absolute scale factor are applied.

899 **Clustering**

900 After calibrated ECAL hits are formed, they must be clustered into shapes that
 901 represent the energy deposit from a single particle. *Basic clusters* are formed around
 902 seed hits, defined as a hit that

- 903 • has calibrated $E_T > 1(0.18)$ GeV in EB(EE),
- 904 • does not originate from a dead channel or one with faulty hardware,
- 905 • is not poorly calibrated,
- 906 • was reconstructed with the standard algorithm (i.e. not a special recovery algo-
- 907 rithm for channels with subpar data integrity),
- 908 • is not saturated,
- 909 • is not spike-like, and
- 910 • is in time (EB).

911 EB basic clusters are formed around the seeds via the *hybrid* algorithm, while EE basic
 912 clusters are formed with the `multi5x5` algorithm [57]. In addition to non-radiating
 913 electrons and unconverted photons, both algorithms are designed to also recover all of
 914 the energy associated with electron bremsstrahlung deposits and photon conversions.
 915 The geometry of the CMS magnetic field means that bremsstrahlung and conversions
 916 will tend to spread the shower out in ϕ , not η . Both algorithms work by forming
 917 basic clusters around seeds, then combining the basic clusters into *superclusters* (SC)
 918 by searching in a window extended in the ϕ direction for all basic clusters consistent
 919 with bremsstrahlung radiation from the primary electron, or with a photon conversion.
 920 Figure 3.3 illustrates the hybrid algorithm in EB. In EE, the energy deposited in ES
 921 must also be added into the total clustered energy sum.

922 Figure 3.4 shows the effect of superclustering on $Z \rightarrow ee$ reconstruction.

923 Supercluster Corrections

924 The total clustered ECAL energy is defined as

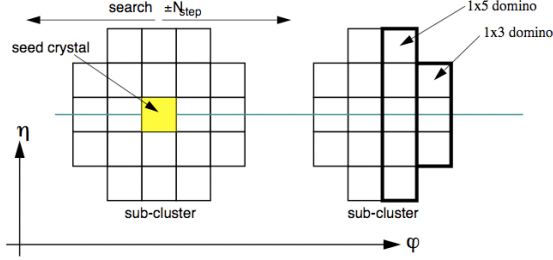


Figure 3.3: Hybrid algorithm in EB. The shower extent is essentially constant in η , but spreads out in φ as the two sub-clusters (or basic clusters) are grouped into the same supercluster. Reprinted from ref. [57].

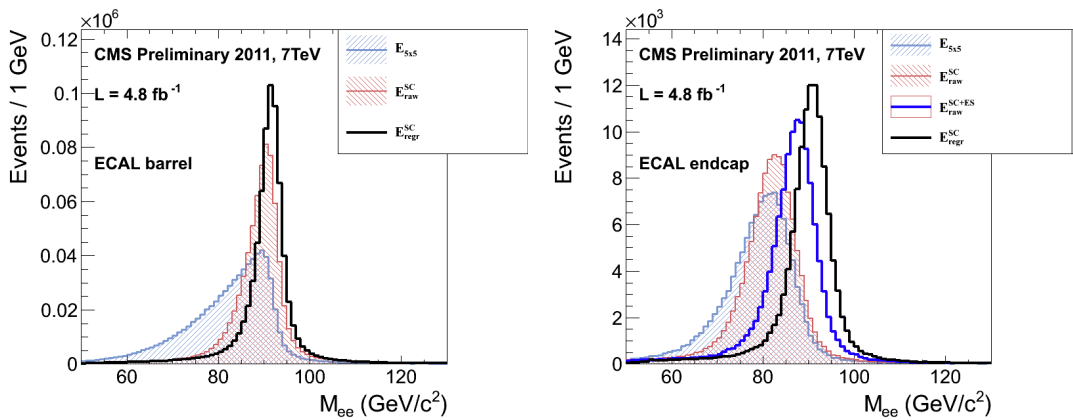


Figure 3.4: Z peak reconstructed in the dielectron channel for different kinds of clustering. The left plot is for EB and the right plot for EE. The constituent hits were calibrated with the best available intercalibrations and laser calibrations as of December 2011. The light blue histogram shows the reconstruction using a 5×5 energy sum, the red histogram shows the reconstruction using the SC energy for crystals only (the dark blue histogram on the right-hand side adds in the energy from ES), and the black histogram shows the reconstruction after the SCs are corrected using a multivariate method [?]. Reprinted from Fig. 30 of ref. [?].

$$E = F \times \sum_{i=1}^{n_{\text{crystal}}} G \times c_i \times A_i \quad (3.1)$$

where G is the ADC-GeV or MIP-GeV scale factor, c_i are the intercalibration constants, A_i is the uncalibrated hit amplitude in ADC counts, and F is a SC correction factor. G and c_i were explained in Sec. 3.1.1. F is a product of three factors for hybrid SCs (two for multi5x5 SCs) [57]:

1. $C_{\text{EB}}(\eta)$, which compensates for lateral energy leakage due to the crystal off-pointing in EB. These corrections are taken from MC simulation [57] and were confirmed in test beams [52].
2. $f(\text{brem})$, which corrects for biases in the clustering algorithms for showers characterized by differing amounts of bremsstrahlung. These corrections are taken from MC simulation [57].
3. Residual correction $f(E_T, \eta)$, due to the variation in η of detector material traversed by a primary electron or photon, and to any residual E_T dependence of the reconstruction. These corrections are determined from MC and validated on $Z \rightarrow ee$ data samples [58].

Changed

As a benchmark of ECAL calibration performance, the extra energy smearing in MC needed to achieve data/MC agreement in the Z width was between $\sim 0.9\%$ (in the central part of EB for electrons with little bremsstrahlung) and $\sim 3.3\%$ (in the outer part of EE for heavily radiating electrons) [59].

From Supercluster to Photon

The CMS photon object is any SC with $E_T > 10$ GeV and $H/E < 0.5$, unless the SC $E_T > 100$ GeV, in which case the H/E requirement is dropped. H/E is defined as the

946 ratio of energy in the HCAL in a 0.15 cone around the SC centroid, directly behind
 947 the SC, to the SC energy. SCs with $R9 > 0.94(0.95)$ in EB(EE), where $R9$ is defined
 948 as the ratio of the energy in the central 3×3 cluster of crystals divided by the SC
 949 energy $E_{3 \times 3}/E_{\text{SC}}$, are the best calibrated and most accurate type of electromagnetic
 950 shower. Therefore, for these objects, the photon energy is defined as the energy sum
 951 of the fully calibrated hits in the central 5×5 cluster around the seed (with $C_{\text{EB}}(\eta)$
 952 applied for EB photons). For all other SCs, the photon energy is equal to the fully
 953 corrected SC energy (cf. Sec. 3.1.1).

Reorganized

954 In this search, candidate photons and *fake photons* (f , “fakes”) are further selected next 3
 955 according to the criteria listed in Table 3.1. Fakes are used in the determination of para-
 956 the QCD background, as explained in Chapter 4. graphs;

edited
Ta-

Table 3.1: Selection criteria for photons and fakes. “Pixel seed,” I_{comb} , and $\sigma_{i\eta i\eta}$ are Ta-

ble 3.1
caption

Variable	Cut (γ)	Cut (f)
SC $ \eta $	< 1.4442	< 1.4442
H/E	< 0.05	< 0.05
$R9$	< 1	< 1
Has pixel seed	No	No
$I_{\text{comb}}, \sigma_{i\eta i\eta}$	$< 6 \text{ GeV} \&\& < 0.011$	$(\geq 6 \&\& < 20 \text{ GeV}) \parallel \geq 0.011$

Updated
effective
area

957 I_{comb} is defined as

$$I_{\text{comb}} = I_{\text{ECAL}} - 0.093\rho + I_{\text{HCAL}} - 0.0281\rho + I_{\text{track}} \quad (3.2)$$

958 where I_{ECAL} , I_{HCAL} , and I_{track} are E_T sums in the annular regions defined in Figure 3.5
 959 and ρ is the average pileup energy density in the calorimeters (per unit $\eta \cdot \phi$) as
 960 measured with the Fastjet algorithm [60, 61]. Note that the ECAL and track isolation
 961 veto strips at constant η ensure that the isolation cuts are similarly efficient for
 962 converted photons, radiating electrons, and unconverted photons.

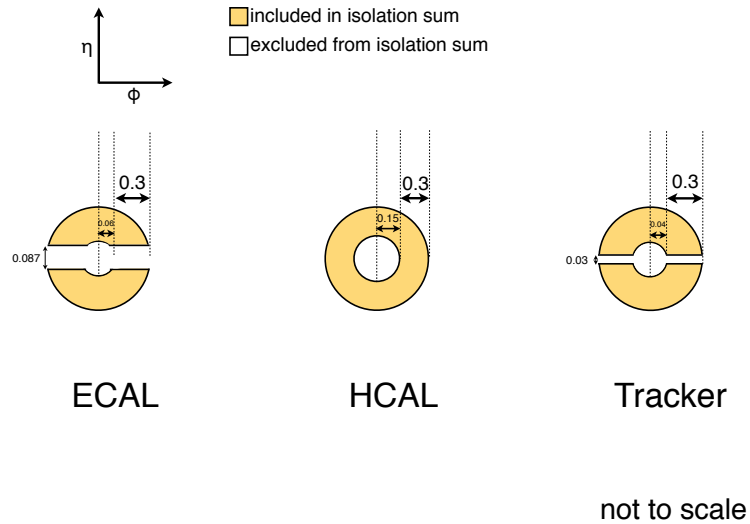


Figure 3.5: ECAL, HCAL, and track Isolation cones.

963 $\sigma_{i\eta i\eta}$ is the log energy weighted extent of the shower in η and is defined as

Added

$\sigma_{i\eta i\eta}$

$$\sigma_{i\eta i\eta} = \frac{\sum_{i=1}^{25} w_i (\eta_i - \bar{\eta})^2}{\sum_{i=1}^{25} w_i} \quad (3.3)$$

defini-
tion

964 where the sums run over the 5×5 matrix of crystals surrounding the seed, $w_i =$
965 $\max(0, 4.7 + \ln(E_i/E))$, E_i is the energy of the i^{th} crystal, E is the total energy in the
966 25 crystals, η_i is the offset in η of the i^{th} crystal from the seed, and $\bar{\eta}$ is the weighted
967 average η of the 25 crystals (using the w_i as weights) [62].

Changed

968 Figure 3.6 shows the ρ distribution for a sample of two-photon events, with at least one 40 GeV and one 25 GeV photon, passing the selection requirements in Table 3.1 and the trigger requirements in Table 3.3. This sample represents the full 2011 dataset of 4.7 fb^{-1} . Since the average ρ is $\sim 7.5 \text{ GeV}$, and there is a long tail above this average value, it is necessary to subtract pileup energy from the ECAL and HCAL isolation cones to recover otherwise clean photons in events with large pileup. The ECAL and HCAL *effective areas* of 0.093 and 0.0281, respectively, are

average

ρ ; up-

dated

fig. 3.6

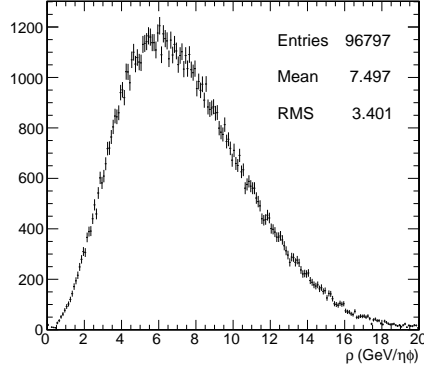


Figure 3.6: ρ distribution for a sample of two-photon events, with at least one 40 GeV and one 25 GeV photon, passing the selection requirements in Table 3.1 and the trigger requirements in Table 3.3. This sample covers the full 2011 dataset of 4.7 fb^{-1} .

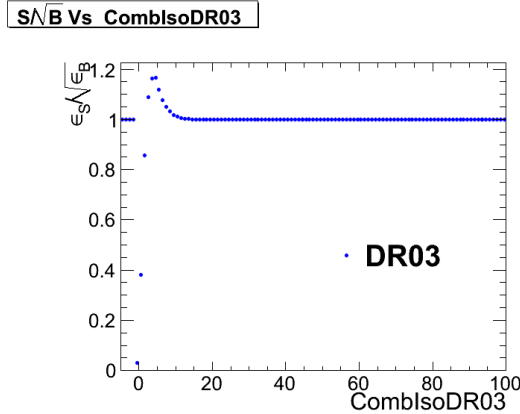


Figure 3.7: S/\sqrt{B} (S and B defined in the text) vs. combined isolation. Reprinted from Fig. 7 of ref. [63].

975 calculated by fitting the average ECAL or HCAL isolation energy vs. ρ in a sample
 976 of $Z \rightarrow ee$ events to a straight line. The slope of the line—which has the units of $\eta \cdot \phi$,
 977 or area—is the effective area.

New

978 The cut on combined isolation of 6 GeV (Table 3.1) is the result of an S/\sqrt{B}
 979 optimization procedure [63]. S is a sample of photons in simulated GGM events that
 980 are products of neutralino decay, while B is a sample of photons matched to generated
 981 hadronic jets in simulated QCD events. Figure 3.7 shows the value of S/\sqrt{B} vs.
 982 combined isolation, in particular the pronounced peak around 6 GeV.

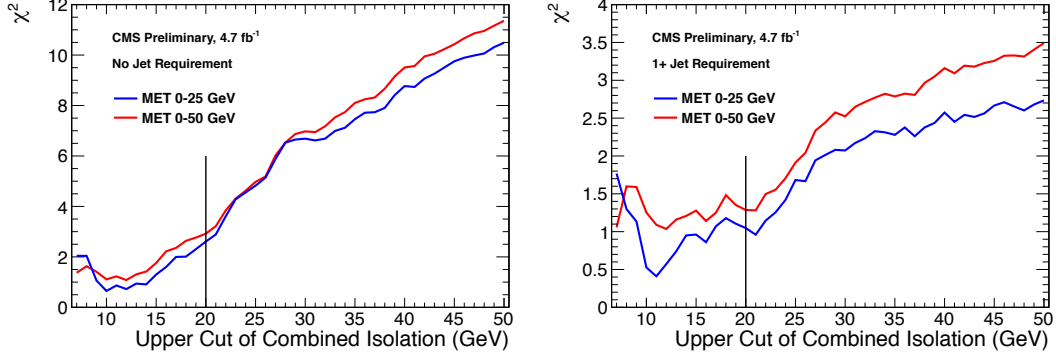


Figure 3.8: Neyman’s χ^2 between the ff and $\gamma\gamma$ \cancel{E}_T distributions, truncated at either 25 (red) or 50 (blue) GeV, vs. upper bound on fake combined isolation. The left plot includes all events; the right plot is for events with ≥ 1 jet defined as in Table 3.2, but with the ΔR cleaning criteria applied to the two primary EM objects and all additional electrons, photons, and fake photons. The full reweighting and normalization procedure is employed in the \cancel{E}_T calculation (see Sec. 4.1). Error bars include statistical, reweighting, and normalization error (see Sec. 4.3). Reprinted from Fig. 9 of ref. [63].

983 The upper bound on fake photon combined isolation guarantees that poorly iso-
 984 lated dijet events, with \cancel{E}_T resolution dissimilar to the candidate diphoton events,
 985 do not enter the ff sample. The exact value of 20 GeV (cf. Table 3.1) arises from
 986 a low- \cancel{E}_T $ff/\gamma\gamma$ χ^2 optimization procedure [63]. Figure 3.8 shows the value of the
 987 Neyman’s χ^2 between the ff and $\gamma\gamma$ \cancel{E}_T distributions, truncated at either 25 or 50
 988 GeV, vs. upper bound on fake combined isolation. As shown in the figure, 20 GeV
 989 very nearly minimizes the χ^2 , while also being large enough that a sufficient number
 990 of ff events may be collected.

991 Finally, a “pixel seed” is defined as a hit in the pixel detector consistent with a
 992 track extrapolated from the position of the ECAL SC back to the primary vertex.
 993 Real photons, having no charge and therefore no bending in the magnetic field, should
 994 not have a pixel seed.

995 3.1.2 Electrons

996 Electrons are reconstructed identically to photons, except that in the electron case
 997 the presence of a pixel seed is enforced, rather than vetoed.² Photons and electrons
 998 are defined by very similar criteria so that $Z \rightarrow ee$ events can be used to model
 999 the QCD background in the two-photon sample without introducing any bias in the
 1000 electron energy measurement (cf. Sec. 4.1).

1001 3.1.3 Jets and Missing Transverse Energy

1002 Particle Flow

1003 In this analysis, jets and \cancel{E}_T are formed from *particle flow* (PF) candidates. The parti-
 1004 cle flow algorithm [67, 68] uses information from all CMS subdetectors to reconstruct
 1005 as accurately as possible the positions and momenta of all visible jet constituents,
 1006 exploiting the fine granularity of the tracker and ECAL to achieve a greatly improved
 1007 momentum resolution over calorimeter-only jets [69]. The PF algorithm is summa-
 1008 rized below [70].

- 1009 1. Reconstruct the fundamental detector objects via iterative procedures
 - 1010 • Tracks in the inner silicon layers
 - 1011 – High efficiency and low fake rate for charged hadrons in jets
 - 1012 – Relaxed primary vertex constraint allows photon conversions, parti-
 1013 cles originating from nuclear interactions in the silicon, and long-lived
 1014 particles to be reconstructed
 - 1015 • Calorimeter clusters
 - 1016 • Muon tracks in the outer muon layers

²In many CMS analyses, electrons are reconstructed very differently from photons. In particular, a special tracking algorithm [66] is used to best follow a radiating electron. However, in this analysis, the electron tracking is not used.

1017 2. Create a “block” of linked fundamental objects

- 1018 • Link silicon tracks to calorimeter clusters via $\Delta R_{\text{track-cluster}}$ (account for
1019 electron bremsstrahlung)
- 1020 • Link clusters in one calorimeter layer to clusters in a separate layer via
1021 $\Delta R_{\text{cluster-cluster}}$
- 1022 • Link silicon tracks to muon tracks via global track χ^2

1023 3. ID the particles in the block

- 1024 • If global (silicon + muon layers) muon p_T is compatible with silicon track
1025 p_T , ID as a muon and remove corresponding tracks from block
- 1026 • ID electron tracks via special algorithm and removed all corresponding
1027 tracks and cluster from block
- 1028 • Remove fake tracks from the block Fixed
- 1029 • Remove excess track-cluster links via $\Delta R_{\text{track-cluster}}$ minimization (but al-
1030 low multiple tracks to be associated to one cluster) typo
- 1031 • If the cluster energy is significantly larger then the energy of the linked
1032 track, ID as a PF photon or PF neutral hadron and remove corresponding
1033 clusters from the block
- 1034 • If the cluster is not linked to a track, ID as a PF photon or PF neutral
1035 hadron and remove corresponding clusters from the block
- 1036 • Remaining track-cluster links are PF charged hadrons

1037 **Jets**

1038 PF candidates are clustered into jets by means of the anti- k_T algorithm with $R = 0.5$
1039 [71]. In this algorithm, all possible pairs of PF candidates i, j are looped over, and
1040 the momenta of the pair that minimize the distance variable

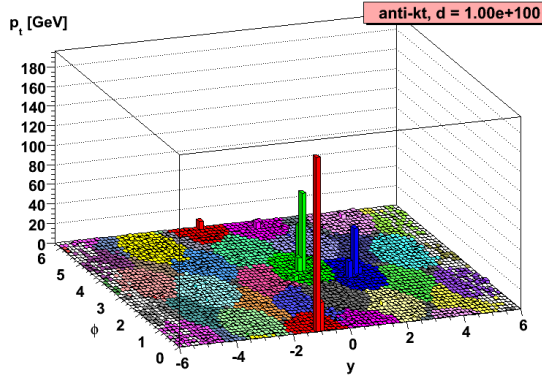


Figure 3.9: Example event display showing jets clustered via the anti- k_T algorithm. y is pseudorapidity. Reprinted from slide 85 of ref. [72].

$$d_{ij} = \frac{\Delta R_{ij}^2}{R^2 \max(k_{Ti}^2, k_{Tj}^2)} \quad (3.4)$$

1041 are combined, where k_{Ti} is the transverse momentum of “combined” PF candidate i .
 1042 The constituent PF candidates are clustered together. The process is repeated until
 1043 $d_{ij} > 1/k_{Ti}^2$ for all pairs of clustered PF momenta [72]. An illustration is given in Fig-
 1044 ure 3.9. The anti- k_T algorithm is infrared and collinear safe, leading to well-behaved Added
 1045 theoretical predictions and ease of comparison between data and MC simulation. It refer-
 1046 also tends to form circular jets, making it easy for experimental effects such as ex- ence to
 1047 pected out-of-cone energy and fiducial acceptance to be measured or simulated. For Fig. 3.9
 1048 these reasons, the anti- k_T jet clustering algorithm was chosen for this analysis.

1049 Once jets are clustered, they must be corrected for biases in the energy mea-
 1050 surement due to non-compensation [73], invisible energy (lost to overcoming nuclear
 1051 binding energy, in neutrinos, or in unclustered muons, for example) [73], detector
 1052 geometry and cracks [74], zero suppression and trigger inefficiencies [75], pileup, and
 1053 effects of the clustering algorithm [74]. Four multiplicative correction factors are ap-
 1054 plied to the raw jet four-momentum p_μ^{raw} [69]:

- 1055 • $C_{\text{offset}}(p_T^{\text{raw}})$, which accounts for extra energy due to noise, pileup, and the un-

1056 derlying event;

- 1057 • $C_{\text{MC}}(C_{\text{offset}}p_T^{\text{raw}}, \eta)$, which is derived from MC and accounts for most of the p_T
1058 and η dependence;
- 1059 • $C_{\text{rel}}(\eta)$, which accounts for the remaining differences in uniformity over the
1060 entire calorimeter between data and MC; and
- 1061 • $C_{\text{abs}}(C_{\text{rel}}C_{\text{MC}}C_{\text{offset}}p_T^{\text{raw}})$, which accounts for the remaining differences in linear-
1062 ity over the full p_T range between data and MC.

1063 Figure 3.10 shows the total jet energy correction factor $C_{\text{offset}}C_{\text{MC}}C_{\text{rel}}C_{\text{abs}}$ vs. η
1064 for jets reconstructed with the anti- k_T algorithm, $R = 0.5$. The PF jet corrections
1065 are more uniform across η than those of CALO jets (composed of simple calorimeter
1066 towers) or JPT jets (Jet Plus Tracks; composed of calorimeter energies replaced,
1067 where possible, with matching track p_T) [76]. In addition, for p_T in the range 30-200
1068 GeV and $|\eta|$ up to 2.0, the PF jet energy correction uncertainty is lower than that of
1069 the other two types of jets, and never exceeds $\sim 3\%$ [69]. The superior performance
1070 of PF jets motivates their use in this search.

1071 In this analysis, candidate and QCD control events are binned by number of jets
1072 satisfying the criteria in Table 3.2.

1073 Missing Transverse Energy

1074 To be consistent with the jet reconstruction, \cancel{E}_T in this analysis is also reconstructed
1075 from PF candidates. Raw \cancel{E}_T is defined as

$$\cancel{E}_{T\text{raw}} = \left| - \sum_{i=1}^{n_{\text{PF}}} \vec{p}_{Ti} \right| \quad (3.5)$$

Table 3.2: Definition of HB/HE hadronic jets.

Variable	Cut
Algorithm	L1FastL2L3Residual corrected PF
p_T	$> 30 \text{ GeV}$
$ \eta $	< 2.6
Neutral hadronic energy fraction	< 0.99
Neutral electromagnetic energy fraction	< 0.99
Number of constituents	> 1
Charged hadronic energy	$> 0.0 \text{ GeV}$ if $ \eta < 2.4$
Number of charged hadrons	> 0 if $ \eta < 2.4$
Charged electromagnetic energy fraction	< 0.99 if $ \eta < 2.4$
ΔR to nearest PF electron ^a , muon ^b , or one of the two primary EM objects	> 0.5

^aA PF electron is defined as an electron reconstructed with the PF algorithm [64] with $p_T > 15 \text{ GeV}$, $|\eta| < 2.6$, and $(I_{\text{charged}} + I_{\text{photon}} + I_{\text{neutral}})/p_T < 0.2$, where $I_{\text{charged}}(I_{\text{photon}})(I_{\text{neutral}})$ is the sum of PF charged hadron(PF photon)(PF neutral hadron) momenta in a $\Delta R = 0.4$ cone around the PF electron.

^bMuons are reconstructed [65] from a combination of muon station and inner tracker hits. Here, a muon must have track $\chi^2 < 10$, at least one good muon station hit, inner track transverse impact parameter $< 0.02 \text{ cm}$, inner track longitudinal impact parameter $< 0.5 \text{ cm}$, $p_T > 15 \text{ GeV}$, $|\eta| < 2.6$, and $(I_{\text{ECAL}} + I_{\text{HCAL}} + I_{\text{track}})/p_T < 0.2$, where $I_{\text{ECAL}}(I_{\text{HCAL}})(I_{\text{track}})$ is the sum of ECAL(HCAL)(track) momenta in a $\Delta R = 0.3$ cone around the muon.

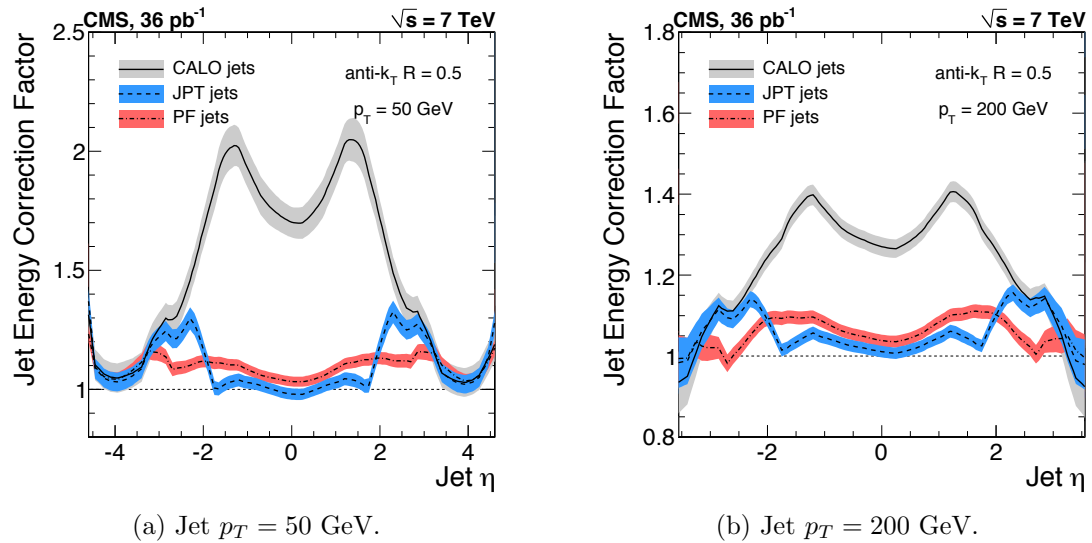


Figure 3.10: Total jet energy correction factor $C_{\text{offset}}C_{\text{MC}}C_{\text{rel}}C_{\text{abs}}$ vs. η , including uncertainty band, for jets reconstructed with the anti- k_T algorithm, $R = 0.5$. Reprinted from Fig. 26 of ref. [69].

where n_{PF} is the number of PF candidates in the event. \cancel{E}_{Raw} may be corrected for the same effects that necessitate jet corrections, since \cancel{E}_{Raw} is usually the result of jet mis-measurement (except, of course, in electroweak physics processes that include an energetic neutrino, or SUSY production). CMS *Type-I* \cancel{E}_T corrections simply involve replacing the PF jets with their corrected energies (cf. Sec 3.1.3) and recalculating \cancel{E}_T . Only jets with electromagnetic fraction (EMF) below 90% and $p_T > 20$ GeV are replaced. This ensures that very electromagnetic jets (as well as isolated leptons, which also receive no correction), which consist chiefly of neutral pions and are measured accurately by the ECAL, do not receive a correction derived for jets with a large fraction of their energy in charged hadrons. In addition, the p_T cut guarantees that jet corrections are only applied where they are known to within a few percent. For this search, the level of agreement between the SM background estimate and the two-photon search sample in a low- \cancel{E}_T control region is the same regardless of whether the \cancel{E}_T is corrected or not, so for simplicity the Type-I \cancel{E}_T corrections are not used (see Sec. ??).

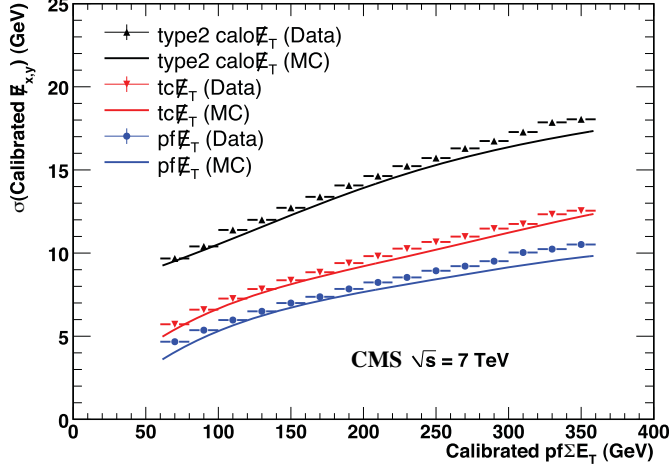


Figure 3.11: σ of a Gaussian fit to the x- and y-components of calibrated E_T vs. the calibrated PF E_T sum in a sample of events containing at least two jets with $p_T > 25$ GeV. σ is calibrated such that the E_T scale is equal for all three algorithms. PF $\sum E_T$ is corrected, on average, to the particle level using a Pythia v8 simulation [77]. The blue markers (data) and line (MC) refer to PF jets. Reprinted from Fig. 13 of ref. [75].

1091 Figure 3.11 shows the σ of a Gaussian fit to the x- and y-components of calibrated
 1092 E_T vs. the calibrated PF E_T sum in a sample of events containing at least two jets
 1093 with $p_T > 25$ GeV. Again, PF E_T outperforms E_T constructed of calorimeter towers
 1094 or track-corrected calorimeter deposits.

1095 3.2 HLT

1096 From the objects described in Sec. 3.1, four samples of events are formed:

- 1097 • $\gamma\gamma$ candidate sample, in which the two highest E_T objects are photons,
- 1098 • $e\gamma$ control sample, in which the two highest E_T objects are one electron and
 one photon,
- 1100 • ee control sample, in which the two highest E_T objects are electrons, and
- 1101 • ff control sample, in which the two highest E_T objects are fakes.

1102 In all samples, the leading EM object is required to have $E_T > 40$ GeV, while the
1103 trailing EM object is required to have $E_T > 25$ GeV. The high level triggers used to
1104 select the four samples, by run range, are listed in Table 3.3. No trigger is prescaled.

Table 3.3: HLT paths triggered by the $\gamma\gamma$, $e\gamma$, ee , and ff samples, by run range. No triggers are prescaled.

Run range	$\gamma\gamma$	$e\gamma$	ee	ff
160404-163261	Photon26_ IsoVL_ Photon18	Photon26_ IsoVL_ Photon18	Photon26_ IsoVL_ Photon18	Photon26_ IsoVL_ Photon18
161216-166967	Photon36_ CaloIdL_ Photon22_ CaloIdL	Photon36_ CaloIdL_ Photon22_ CaloIdL	Photon36_ CaloIdL_ Photon22_ CaloIdL	Photon36_ CaloIdL_ Photon22_ CaloIdL
166347-180252	Photon36_ CaloIdL_ IsoVL_ Photon22_ CaloIdL_ IsoVL	Photon36_ CaloIdL_ IsoVL_ Photon22_ CaloIdL_ IsoVL	Photon36_ CaloIdL_ IsoVL_ Photon22_ R9Id	Photon36_ CaloIdL_ IsoVL Photon36_ CaloIdL_ IsoVL Photon36_ R9Id_ Photon22_ CaloIdL_ IsoVL Photon36_ R9Id_ Photon22_ R9Id

1105 Each piece of the HLT path name is defined as follows.

- 1106 • Photon: Energy deposit in the ECAL that fired an L1 trigger (cf. Sec. 2.2.1).

1107 For Photon26_IsoVL_Photon18, the L1 seed E_T threshold is 12 GeV, while for Switched
 1108 all other triggers in Table 3.3 it is 20 GeV (cf. Sec. 2.2.1). HLT
 1109 • Integer following the word **Photon**: E_T threshold in GeV for offline reconstructed path
 1110 photon, using the full photon reconstruction of Sec. 3.1.1 minus the laser cali- names
 1111 brations and assuming the primary vertex at (0, 0, 0). to ver-
 1112 • **CaloIdL**: For EB photons, $H/E < 0.15$ and $\sigma_{in\eta} < 0.014$. batim
 1113 • **IsoVL**: $I_{ECAL} < 0.012E_T + 6$ GeV, $I_{HCAL} < 0.005E_T + 4$ GeV, and $I_{track} <$ font and
 1114 $0.002E_T + 4$ GeV. added
 1115 • **R9Id**: $R9 > 0.8$. reference
 1116 In addition, the versions of **HLT_Photon26_IsoVL_Photon18** and to L1
 1117 **Photon36_CaloIdL_Photon22_CaloIdL** that were active during runs 160404-163268 section
 1118 included a cut $E_{max}/E_{5\times5} < 0.98$ for spike rejection. E_{max} is the energy in the Switched
 1119 highest HLT path energy crystal of the EM cluster and $E_{5\times5}$ is the energy in the 5×5 crystal matrix names
 1120 around the seed crystal. For runs after 163268, Swiss cross spike rejection of individual to ver-
 1121 crystals from HLT quantities was performed (cf. Sec. 3.1.1). All information about the batim
 1122 evolution of the CMS HLT settings can be found in the HLT configuration browser font
 1123 at <http://j2eeps.cern.ch/cms-project-confdb-hltdev/browser/>. Switched
 1124 As an example of the naming convention just described, the HLT path HLT
 1125 **Photon36_CaloIdL_IsoVL_Photon22_R9Id** is fired if one photon is found with $E_T >$ path
 1126 36 GeV passing the **CaloIdL** and **IsoVL** requirements, and another is found with names
 1127 $E_T > 22$ GeV passing the **R9Id** requirement. to ver-
 1128 For the offline E_T cuts described in this section, the triggers are > 99% efficient, batim
 1129 as shown in Figure 3.12 [63]. The efficiencies are measured with respect to triggers font
 1130 with lower E_T thresholds. Added
 1131 HLT ef-
 1132 ficiency
 1133 discus-
 1134 sion

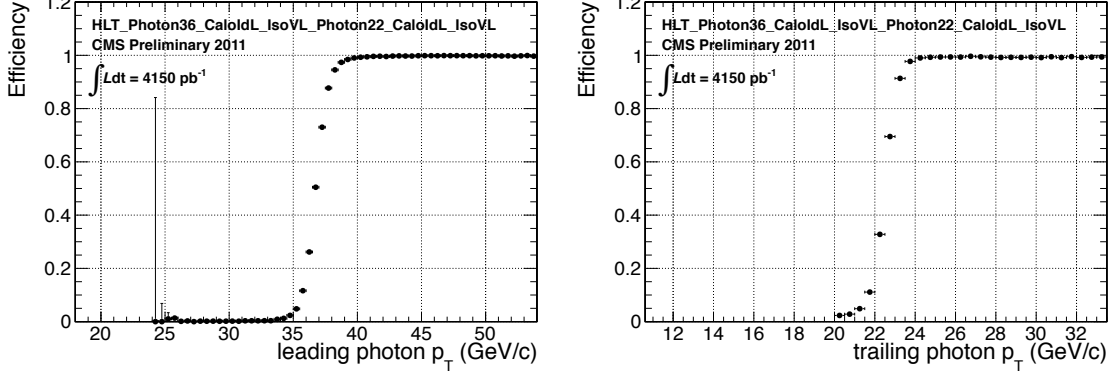


Figure 3.12: Efficiency of HLT_Photon36_CaloIdL_IsoVL_Photon22_CaloIdL_IsoVL for offline selected leading photon (left) and trailing photon (right) vs. photon p_T . Reprinted from Fig. 2 of ref. [63].

1131 3.3 Event Quality

1132 To suppress instrumental backgrounds, a set of event quality cuts are applied to the
 1133 $\gamma\gamma$, $e\gamma$, ee , and ff samples. First, all events are required to pass a good run selec-
 1134 tion, as determined by the CMS Physics Validation Team (<https://twiki.cern.ch/twiki/bin/view/CMS/PVTMain>, CERN computing ID needed). The good run selec-
 1135 tion excludes luminosity sections during which a sufficient part of the CMS detector
 1136 was unpowered or malfunctioning. Such conditions could occur if, for example, a high
 1137 voltage supply trips off in the middle of a run, or a DAQ error corrupts data quality
 1138 but is not spotted until after the data have been collected. The severity of a detec-
 1139 tor problem is judged by its effect on a wide range of analyses and reconstruction
 1140 algorithms. Of the $\sim 5 \text{ fb}^{-1}$ of integrated luminosity delivered by the LHC in 2011,
 1141 4.68 fb^{-1} passed the good run selection. This analysis is performed on the entire 2011
 1142 certified dataset.

1144 Second, all events must contain at least one good interaction vertex. The criteria
 1145 for a good vertex are:

- 1146 • $\chi^2 \neq 0 \parallel \text{ndof} \neq 0 \parallel N_{\text{tracks}} \neq 0$, where χ^2 and ndof are calculated for the track
 1147 fit to the vertex, and N_{tracks} is the number of tracks in the vertex fit

- 1148 • $\text{ndof} > 4$
- 1149 • $|z| < 24 \text{ cm}$, where z is the z -coordinate of the vertex position
- 1150 • $|\rho| < 2 \text{ cm}$, where ρ is the transverse displacement of the vertex position from
1151 the beam line

1152 The good vertex requirement eliminates non-collision backgrounds such as beam
1153 scraping, beam halo, cosmic muon interactions, and instrumental effects.

1154 Third, the two electromagnetic objects in the $\gamma\gamma$, $e\gamma$, ee , and ff events must
1155 be separated in ϕ by at least 0.05. This requirement protects against beam halo
1156 bremsstrahlung, in which a halo muon traveling parallel to the beam line radiates an
1157 energetic photon while itself depositing a large amount of energy in the ECAL. In
1158 this case, the two ECAL hits would likely be at the same ϕ (and ρ).

1159 Fourth, the two EM objects must be separated in R by at least 0.6. Since the
1160 isolation cone size used is 0.3, this ensures that the isolation energy of one EM object
1161 cannot be in the veto strip (Fig. 3.5) of the other.

1162 Finally, the $\gamma\gamma$, $e\gamma$, ee , and ff events must pass an HCAL noise filter and ECAL
1163 dead channel filter. The HCAL noise filter guarantees that all HCAL reconstructed
1164 hits are inconsistent with any noise source. Noise sources [78] include:

- 1165 • Ion feedback in the HPDs absent any true incident photons, in which a thermal
1166 electron ionizes a molecule in the HPD acceleration gap, faking a real signal
- 1167 • HPD discharge affecting nearly all channels in the same HPD [79], partially
1168 explained by the effect of the 4 T CMS magnetic field on the flashover voltage
1169 of the dielectric [81]
- 1170 • Concurrent signals in nearly all 72 channels of a single RBX, as yet unexplained
- 1171 • HF PMT window hits (as opposed to the usual quartz fiber hits)

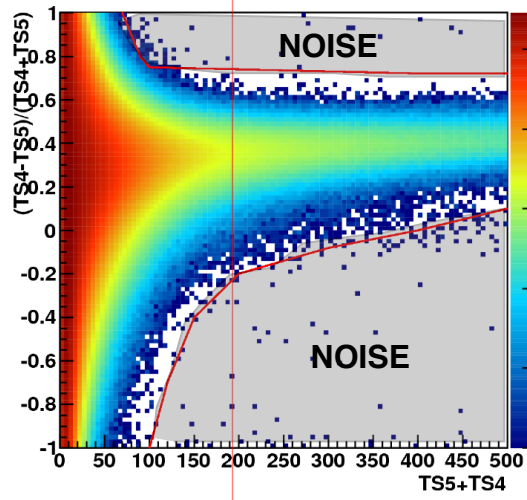


Figure 3.13: $(TS4 - TS5)/(TS4 + TS5)$ vs. $TS4 + TS5$ for a minimum bias sample. HB/HE hits are considered noisy if they lie in the sparsely populated gray region labeled "NOISE" defined by the curved red lines. Adapted from ref. [80].

- 1172 • ADC saturation

1173 Since HCAL noise may induce fake jets or E_T , events are rejected if any of the
1174 following criteria are true:

- 1175 • Any HPD has > 17 hits

- 1176 • A single HPD has > 10 hits, but every other HPD has zero hits

- 1177 • An RBX has > 10 zero-ADC-count hits

1178 • Any HB/HE reconstructed hit corresponding to an RBX with > 50 GeV of
1179 energy fails a two-dimensional cut defined by the variables $(TS4 - TS5)/(TS4 +$
1180 $TS5)$ vs. $TS4 + TS5$, where $TS4(TS5)$ is the hit amplitude in the fourth(fifth)
1181 time sample read out for that hit. The cut is defined in Fig. 3.13.

1182 The ECAL dead channel filter is designed to flag events in which significant EM
1183 energy was deposited in a masked region of the ECAL by using the trigger primitive
1184 information for the corresponding trigger tower. Energy deposited in a masked region

1185 of ECAL can cause fake E_T . Events are rejected if the trigger primitive E_T exceeds
1186 the maximum value of 63.75 GeV in any trigger tower that is masked in the readout.

1187 3.4 Photon Identification Efficiency

1188 In order to determine the cross section (or cross section upper limit) for a GGM
1189 signal, the photon identification efficiency is needed. Since no suitably large sample
1190 of $Z \rightarrow \mu\mu\gamma$ events in CMS exists yet, the efficiency calculation relies on the similarity
1191 between detector response to electrons and photons. A scale factor to correct the MC
1192 photon ID efficiency to the real photon efficiency for the data is obtained from the
1193 ratio of the electron efficiency from the data to the electron efficiency from MC.
1194 The different types of photon ID variables—calorimeter and track isolation, ratio of Removed
1195 hadronic to electromagnetic energy of the shower, and transverse shower shape—are refer-
1196 chosen so that their distributions for isolated electrons and photons are similar.³ ence to
1197 The photon selection efficiency is plots

$$\epsilon_\gamma = \epsilon_\gamma^{\text{MC}} \times \frac{\epsilon_e^{\text{data}}}{\epsilon_e^{\text{MC}}} \quad (3.6)$$

1198 where

- 1199 • ϵ_γ is the photon ID efficiency in data,
- 1200 • $\epsilon_\gamma^{\text{MC}}$ is the photon ID efficiency in MC,
- 1201 • ϵ_e^{data} is the electron ID efficiency obtained using $Z \rightarrow ee$ electrons in the data
1202 that satisfy the photon ID cuts, and

³R9 differs between photons and radiating electrons, but the requirement $R9 < 1$ is loose enough not to introduce problems with the use of electrons to measure the photon ID efficiency.

- 1203 • ϵ_e^{data} is the electron ID efficiency obtained using $Z \rightarrow ee$ electrons in MC that
 1204 satisfy the photon ID cuts.

1205 The ratio $\epsilon_e^{\text{data}}/\epsilon_e^{\text{MC}}$ is defined as the scale factor by which the GGM signal MC
 1206 photon ID efficiency must be multiplied to give an estimate of the photon ID efficiency
 1207 in data. The photon ID requirements of Table 3.1 plus the IsoVL HLT requirement
 1208 described in Sec. 3.2 and Table 3.3 are repeated in Table 3.4.

Table 3.4: Candidate photon ID requirements.

Variable	Cut
I_{ECAL}	$< 0.012E_T + 6 \text{ GeV}$
I_{HCAL}	$< 0.005E_T + 4 \text{ GeV}$
I_{track}	$< 0.002E_T + 4 \text{ GeV}$
H/E	< 0.05
$\sigma_{i\eta i\eta}$	< 0.011
$I_{\text{ECAL}} - 0.0792\rho + I_{\text{HCAL}} - 0.0252\rho + I_{\text{track}}$	$< 6 \text{ GeV}$
$R9$	< 1

1209 3.4.1 Tag and Probe Method

1210 A *Z tag and probe* method is utilized to measure the efficiency of the photon ID
 1211 cuts in Table 3.1. The tag is a well-identified electron. The probe, by contrast, is as
 1212 loosely identified as possible, and all tags must pass the probe criteria in addition to
 1213 the stringent tag criteria. The tag and probe criteria used in this study are shown in
 1214 Table 3.5.

1215 The invariant mass of the tag and probe are required to be within a narrow window
 1216 around Z mass. Assuming that the probabilities of the tag and probe legs of the Z
 1217 decay to pass the photon ID cuts are uncorrelated, the efficiency can be estimated as

$$\epsilon = \frac{N_{\text{tag-pass}}}{N_{\text{tag-pass}} + N_{\text{tag-fail}}} \quad (3.7)$$

Table 3.5: Tag and probe criteria. The superscript 0.4 indicates that the isolation variable was calculated in a cone of $\Delta R = 0.4$ around the photon candidate. The isolations without superscripts use the standard $\Delta R = 0.3$ cones.

Variable	Cut	
	Tag	Probe
RECO object	photon	photon
HLT	HLT_Ele17_CaloIdVT_CaloIsoVT_TrkIdT_TrkIsoVT_SC8_Mass30_v* (must have fired the 17 GeV leg)	—
H/E	< 0.05	< 0.15
$I_{\text{ECAL}}^{0.4}$	$< 0.006E_T + 4.2 \text{ GeV}$	—
$I_{\text{HCAL}}^{0.4}$	$< 0.0025E_T + 2.2 \text{ GeV}$	—
$I_{\text{track}}^{0.4}$	$< 0.001E_T + 2.0 \text{ GeV}$	—
E_T	$> 25 \text{ GeV}$	—
SC E_T	—	$> 15 \text{ GeV}$
SC $ \eta $	< 1.4442	< 1.4442
$\sigma_{i\eta i\eta}$	< 0.009	—
Has pixel seed	Yes	—
Track match type	General track ^a	—
Track match ΔR	< 0.04	—
Track match p_T	$> 15 \text{ GeV}$	—
Track match $ \eta $	< 1.479	—

^aA general track is reconstructed with the CMS standard combinatorial track finder [82].

1218 where $N_{\text{tag-pass}}$ is the number of tag-probe pairs in which the probe leg passes the
 1219 photon ID cuts under study and $N_{\text{tag-fail}}$ is the number of tag-probe pairs in which
 1220 the probe leg fails the cuts. Implicit in these definitions is a double counting of pairs
 1221 in which both electrons pass the tag and probe criteria [83]. In addition, in the rare
 1222 circumstance (less than 1% in MC [83]) that two or more probes may be matched to
 1223 one tag, the pair with invariant mass closest to the Z mass is chosen.

1224 In practice, $N_{\text{tag-pass}}$ and $N_{\text{tag-fail}}$ are returned by a simultaneous unbinned maxi-
 1225 mum likelihood fit to the invariant mass distributions of tag-pass and tag-fail events,
 1226 with appropriate signal and background PDF assumptions. The fit form used is

$$\begin{aligned} f_{\text{tag-pass}}(m_{\text{tag-pass}}) &= \epsilon N_S f_S^{\text{pass}}(m_{\text{tag-pass}}) + N_B^{\text{pass}} f_B^{\text{pass}}(m_{\text{tag-pass}}) \\ f_{\text{tag-fail}}(m_{\text{tag-fail}}) &= (1 - \epsilon) N_S f_S^{\text{fail}}(m_{\text{tag-fail}}) + N_B^{\text{fail}} f_B^{\text{fail}}(m_{\text{tag-fail}}) \end{aligned} \quad (3.8)$$

1227 where $f_{\text{tag-pass}}(m_{\text{tag-pass}})$ and $f_{\text{tag-fail}}(m_{\text{tag-fail}})$ are the tag-pass and tag-fail PDFs,
 1228 respectively; ϵ is the efficiency; N_S is the total number of Z signal events summed over
 1229 both samples; $f_S^{\text{pass}}(m_{\text{tag-pass}})$ and $f_S^{\text{fail}}(m_{\text{tag-fail}})$ are the tag-pass and tag-fail signal
 1230 PDFs, respectively; N_B^{pass} and N_B^{fail} are the numbers of background events in the tag-
 1231 pass and tag-fail samples, respectively; and $f_B^{\text{pass}}(m_{\text{tag-pass}})$ and $f_B^{\text{fail}}(m_{\text{tag-fail}})$ are the
 1232 tag-pass and tag-fail background PDFs, respectively. This particular implementation
 1233 of the tag and probe methodology is based on tag `CMSSW_4_2_5` of the CMSSW
 1234 package `PhysicsTools/TagAndProbe`, and uses the MINUIT2 [84] library, as coded
 1235 in RooFit [85], for the likelihood maximization. For this study, CMSSWv4.2.8 was
 1236 used.

1237 For both samples, the signal shape is assumed to be a Crystal Ball function [86]
 1238 convoluted with the Z generated lineshape, while the background shape is a PDF
 1239 that describes the falling background as well as the kinematic turn-on at low invariant

1240 mass. The background PDF, called `RooCMSShape` [83], is given by

$$f_{\text{RooCMSShape}}(x) = \begin{cases} 1e20 & \text{for } (x - \mu)\gamma < -70 \\ 0 & \text{for } (x - \mu)\gamma > 70 \\ \text{erfc}((\alpha - x)\beta) \exp(-(x - \mu)\gamma) & \text{otherwise} \end{cases} \quad (3.9)$$

1241 where α , β , γ , and μ are parameters of the fit, most of which are held fixed. In the
 1242 three lowest E_T bins, all parameters of the tag-pass and tag-fail background PDFs
 1243 are left floating, because the effect of the relaxed E_T cuts has a significant effect on
 1244 the background shape. More details of the signal and background PDFs are given
 1245 in Table 3.6. The fixed signal and background parameter values were determined by
 1246 fitting a small sample ($0.0 \leq \eta < 0.25$) of `Fall11 MC signal (DYJetsToLL)` and back-
 1247 ground (`QCD_Pt-20to30_BCtoE`, `QCD_Pt-30to80_BCtoE`, `QCD_Pt-80to170_BCtoE`,
 1248 `GJet_Pt-20_doubleEMEnriched`, `WJetsToLNu`, `TTJets`) with parameters left float-
 1249 ing.⁴

Added

1250 Some fit examples are shown in Figures 3.14 and 3.15. In Fig. 3.14, which shows fits
 1251 fits to data and MC for $15 \text{ GeV} \leq \text{probe } E_T < 20 \text{ GeV}$, the kinematic turn-on is below
 1252 the invariant mass range covered by the plot. The exponentially falling background
 1253 is easily seen underneath the signal, and is especially pronounced in the background-
 1254 dominated tag-fail sample.

1255 3.4.2 Photon Efficiency Scale Factor $\epsilon_e^{\text{data}}/\epsilon_e^{\text{MC}}$

1256 Figure 3.16 shows the dependence of the photon ID efficiency scale factor $\epsilon_e^{\text{data}}/\epsilon_e^{\text{MC}}$
 1257 on E_T , η , and N_{jet} , where jets are defined as in Table 3.2, but with only the two
 1258 Z electrons considered as candidates for overlap removal. Errors are statistical only.

⁴See Appendix A for a discussion of the MC samples.

Table 3.6: Parameter values (parameter definitions are in the text) for the signal and background PDFs for the different samples. The background PDF applies to all efficiency bins except the four lowest E_T bins, which use a floating `RooCMSShape` background. When a bracketed range is given, the parameter is allowed to float within that range. When a constant is given, the parameter is fixed to that constant.

PDF	Crystal Ball fit parameters				RooCMSShape fit parameters			
	μ	σ	α	n	μ	α	β	γ
Tag-pass signal	[-1.0, 1.0]	[1.0, 3.0]	0.87	97.0	N/A	N/A	N/A	N/A
Tag-fail signal	[-1.0, 1.0]	[1.0, 3.0]	0.73	134.9	N/A	N/A	N/A	N/A
Tag-pass background	N/A	N/A	N/A	N/A	65.0	61.949	0.04750	0.01908
Tag-fail background	N/A	N/A	N/A	N/A	α	[50.0, 100.0]	0.065	0.048

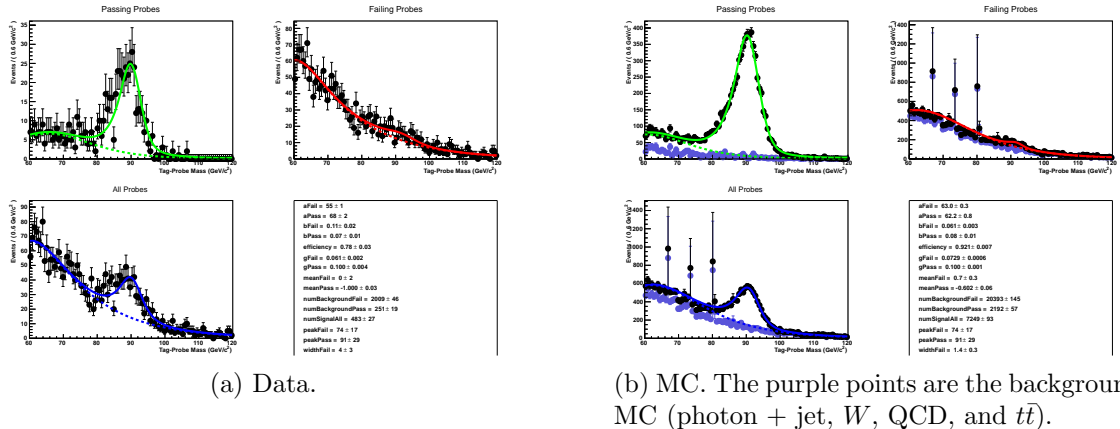


Figure 3.14: Tag and probe invariant mass fits for $15 \text{ GeV} \leq \text{probe } E_T < 20 \text{ GeV}$. Errors are statistical only. The tag-pass fit is shown in green, the tag-fail fit in red, and a fit to both samples in blue. Dotted lines are the background components of the fits; solid lines are signal plus background.

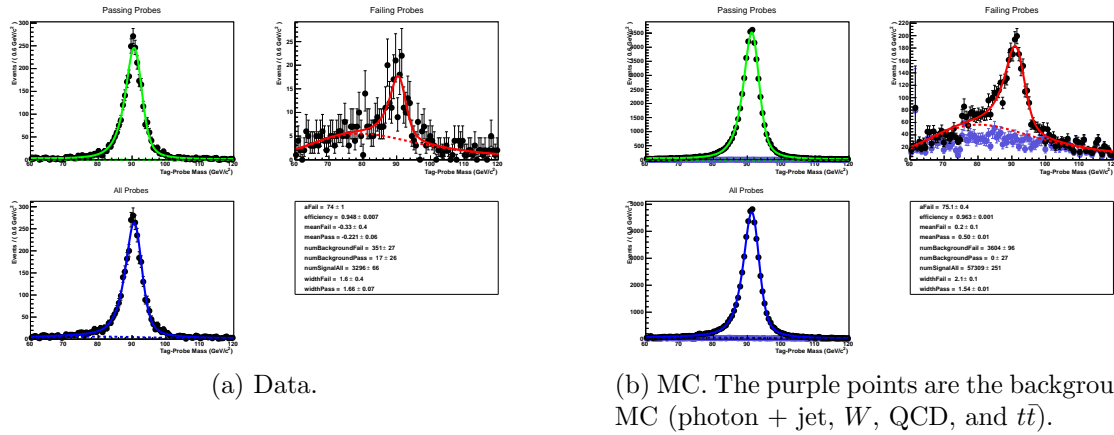


Figure 3.15: Tag and probe invariant mass fits for $-0.25 \leq \text{probe } \eta < -0.5$. Errors are statistical only. The tag-pass fit is shown in green, the tag-fail fit in red, and a fit to both samples in blue. Dotted lines are the background components of the fits; solid lines are signal plus background.

1259 There no significant dependence of the scale factor on these variables, so only one
1260 scale factor is computed from the entire dataset.

1261 The effect of pileup is studied by comparing the efficiencies ϵ_e^{data} and ϵ_e^{MC} vs. the
1262 number of primary vertices (N_{PV}) in the event. The efficiency only drops a few percent
1263 for events with large N_{PV} after using pileup-corrected isolation cuts, as can be seen in
1264 Figure 3.17a. The MC tracks the data, and the scale factor is flat vs. N_{PV} , as shown
1265 in Fig. 3.17b.

1266 The scale factor is measured to be $\epsilon_e^{\text{data}}/\epsilon_e^{\text{MC}} = 0.994 \pm 0.002(\text{stat.}) \pm 0.035(\text{syst.})$.
1267 Four main sources of systematic error, in addition to the statistical error of 0.2%, were
1268 studied.

1269 **Different behavior of electrons and photons in MC** Even though the photon
1270 ID cuts are designed to be similarly efficient for both electrons and photons,
1271 there might be a small difference in the performance between the two kinds
1272 of particles, e.g. because of electron bremsstrahlung. To check this effect, the
1273 MC electron ID efficiency was calculated using a $Z \rightarrow ee$ sample and the MC
1274 photon ID efficiency was calculated using a $\gamma + \text{jets}$ sample. Both samples were

Official
result
uses this
syst.
error, so
I am not
recheck-
ing
it

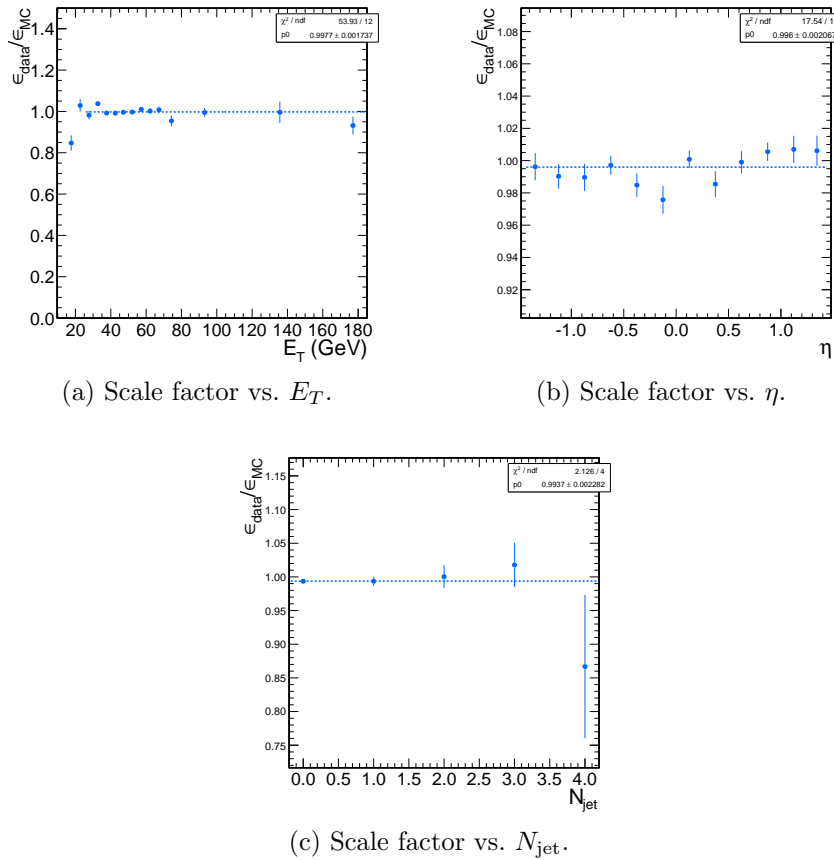


Figure 3.16: Dependence of the photon ID efficiency scale factor on some kinematic variables. Errors are statistical only.

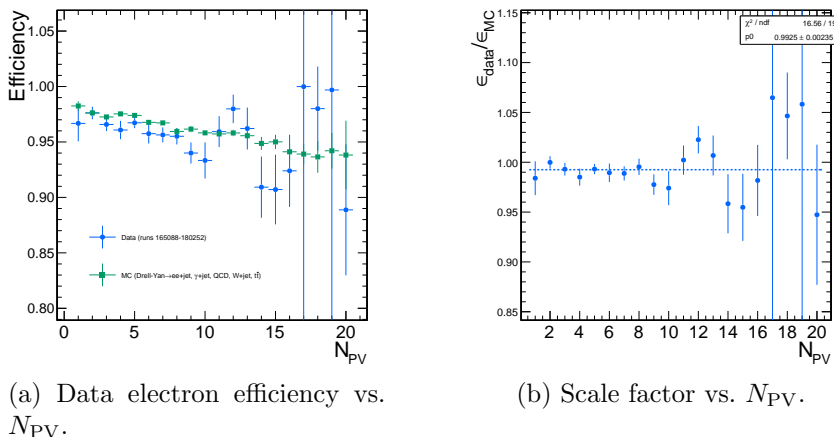


Figure 3.17: Dependence of the photon ID efficiency scale factor on the number of primary vertices per event. Errors are statistical only.

1275 reconstructed in CMSSWv3.6. Half the difference between these two results,
 1276 0.5%, was taken as an error on the scale factor.

Corrected

1277 **Pileup** To account for the possibility that the MC simulation may not adequately some of
 1278 reproduce the data in a high pileup environment, the data/MC scale factor these
 1279 for events with 1-4 good reconstructed primary vertices was calculated, along bullets
 1280 with the same for events with ≥ 5 good reconstructed primary vertices. The
 1281 difference between the scale factors from both samples, 2.4%, was taken as an
 1282 error on the scale factor from pileup.

1283 **Signal fit over/underestimation** It was found that the signal fit slightly under-
 1284 estimates the data in the tag-pass sample, and slightly overestimates it in the tag-fail sample. To cover this effect with a systematic error, the efficiencies in
 1285 data and MC, and then the scale factor, were recalculated using the background
 1286 (from fit) subtracted integrals of the tag-pass and tag-fail distributions, rather
 1287 than the fitted signal yields in those distributions. The difference between the
 1288 scale factor found in this way and the nominal scale factor, 1.9%, was taken as
 1289 an error on the scale factor.

1290 **Signal and background shape assumption** To assess the magnitude of the error
 1291 from the signal and background shape assumptions, the tag-pass and tag-fail
 1292 tail parameters (Crystal Ball α and n) were varied by $\pm 1\sigma$, and the background
 1293 shape was varied between `RooCMSShape`, exponential, power law, and quadratic.
 1294 All possible combinations of varied parameters were generated, and the data and
 1295 MC were refit and new scale factors generated according to those combinations.
 1296 The error was taken as the largest deviation of the scale factor from nominal,
 1297 1.8%.

1298 Finally, the pixel veto efficiency was estimated from MC to be 0.96 ± 0.005 (syst.),
 1300 with error due to varying assumptions of the tracker material distribution [87].

1301 Chapter 4

1302 Data Analysis

1303 The signature of GGM SUSY particle production in this search is an excess of two-
1304 photon events with high \cancel{E}_T . \cancel{E}_T is reconstructed using the particle flow algorithm
1305 as described in Sec. 3.1.3. Candidate two-photon events, as well as control events,
1306 are selected according to the offline object criteria presented in Secs. 3.1.1, 3.1.2,
1307 and 3.1.3; the event quality criteria in Sec. 3.3; and the trigger requirements in Sec. 3.2.
1308 These are summarized in Table 4.1.

Table 4.1: Selection criteria for $\gamma\gamma$, $e\gamma$, ee , and ff events.

Variable	Cut			
	$\gamma\gamma$	$e\gamma$	ee	ff
HLT match	IsoVL	IsoVL	IsoVL	IsoVL R9Id
E_T	$> 40/ > 25 \text{ GeV}$			
SC $ \eta $	< 1.4442	< 1.4442	< 1.4442	< 1.4442
H/E	< 0.05	< 0.05	< 0.05	< 0.05
$R9$	< 1	< 1	< 1	< 1
Pixel seed	No/No	Yes/No	Yes/Yes	No/No
I_{comb} , $\sigma_{inj\eta}$	$< 6 \text{ GeV} \&& < 0.011$	$< 6 \text{ GeV} \&& < 0.011$	$< 6 \text{ GeV} \&& < 0.011$	$< 20 \text{ GeV} \&& (\geq 6 \text{ GeV} \parallel \geq 0.011)$
JSON	Yes	Yes	Yes	Yes
No. good PVs	≥ 1	≥ 1	≥ 1	≥ 1
ΔR_{EM}	> 0.6	> 0.6	> 0.6	> 0.6
$\Delta\phi_{\text{EM}}$	≥ 0.05	≥ 0.05	≥ 0.05	≥ 0.05

1309 This search utilizes 4.7 fb^{-1} of CMS data collected during the period April
 1310 December 2011, corresponding to the following datasets [88]:

- 1311 • /Photon/Run2011A-05Jul2011ReReco-ECAL-v1/AOD
- 1312 • /Photon/Run2011A-05Aug2011-v1/AOD
- 1313 • /Photon/Run2011A-03Oct2011-v1/AOD
- 1314 • /Photon/Run2011B-PromptReco-v1/AOD

1315 The search strategy is to model the backgrounds to the GGM SUSY signal using
 1316 \cancel{E}_T shape templates derived from the control samples, and then to look for a high- \cancel{E}_T
 1317 excess above the estimated background in the $\gamma\gamma$ sample. There are two categories
 1318 of backgrounds: QCD processes with no real \cancel{E}_T and electroweak processes with real
 1319 \cancel{E}_T from neutrinos. The relevant QCD background processes are multijet production
 1320 with at least two jets faking photons, photon + jet production with at least one jet
 1321 faking a photon, and diphoton production, and Z production with a radiated photon
 1322 where at least one of the Z decay products (typically a jet) fakes a photon. The
 1323 relevant electroweak background processes, which are small compared to the QCD
 1324 background, involve $W \rightarrow e\nu$ decay with a recoiling jet that fakes a photon or a
 1325 real radiated photon (the W may come from the decay of a top quark in $t\bar{t}$ events).
 1326 In both cases, the electron is misidentified as a photon due to a small inefficiency
 1327 in reconstructing the electron pixel seed. The main diagrams contributing to the
 1328 QCD(electroweak) backgrounds are shown in Figure 4.1(4.2).

1329 Data control samples are used to model all of the backgrounds. The primary
 1330 control sample used to model the QCD background is the ff sample, which is similar
 1331 to the candidate $\gamma\gamma$ sample but with combined isolation or $\sigma_{inj\eta}$ cuts inverted. The cuts
 1332 on these variables are used to distinguish between photons and jets, so by inverting
 1333 those cuts, the resulting ff sample becomes enriched with QCD dijets. Because the

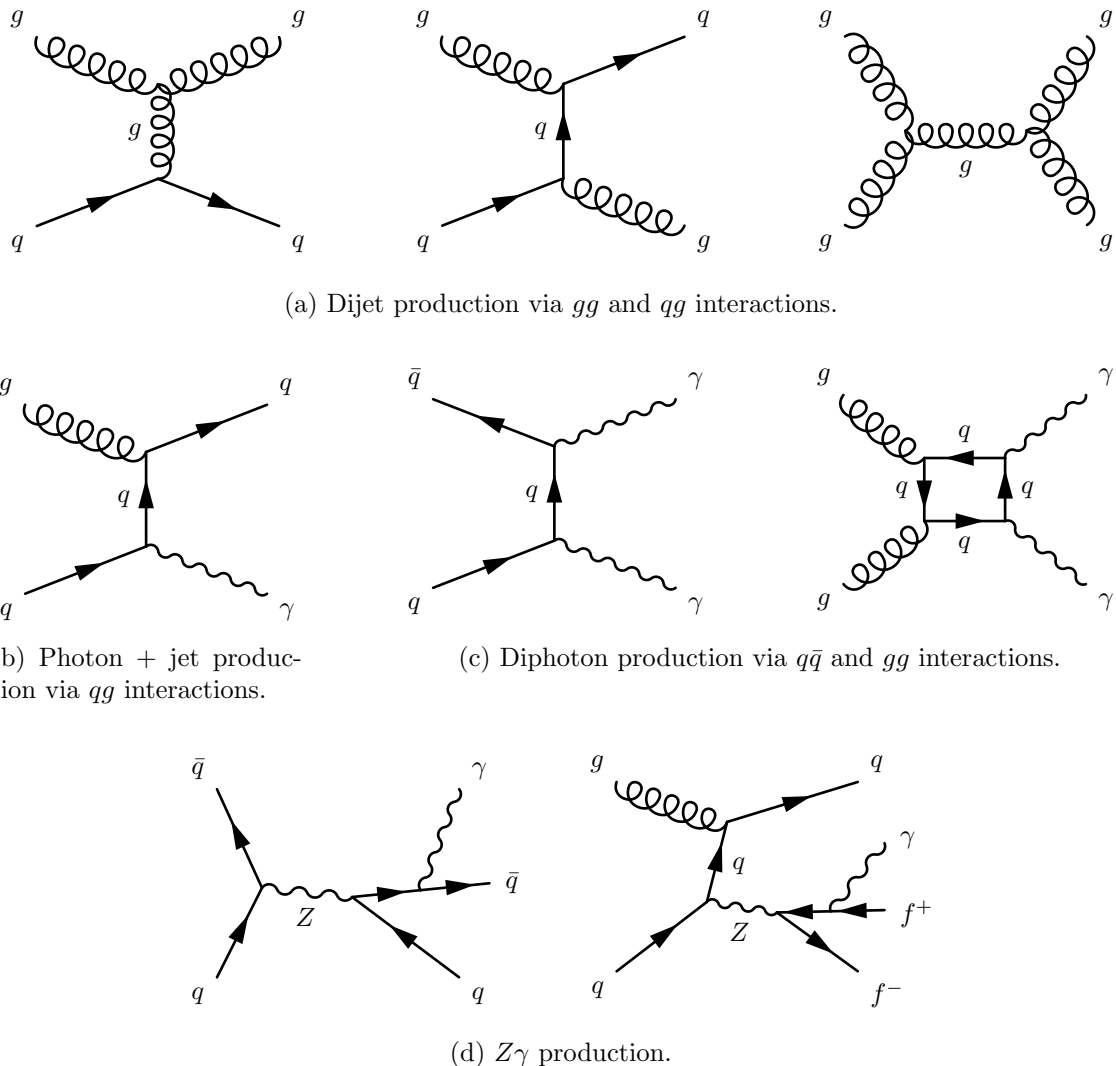


Figure 4.1: Representative Feynman diagrams of some QCD backgrounds to the GGM SUSY search.

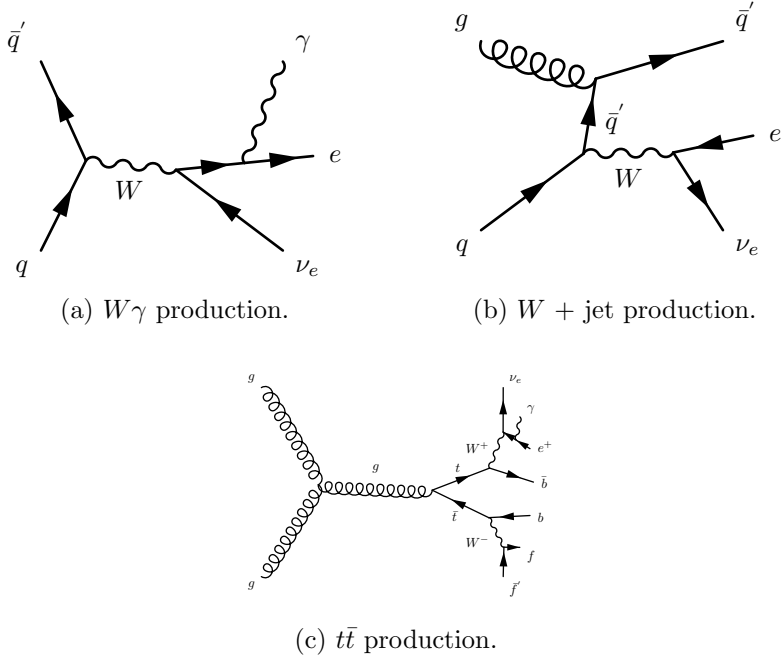


Figure 4.2: Representative Feynman diagrams of some electroweak backgrounds to the GGM SUSY search.

fake photons are still required to pass a tight cut on H/E , they are guaranteed to be very electromagnetic jets, with an EM energy scale and resolution similar to that of the candidate photons. This insures that the resulting estimate of the \cancel{E}_T shape does not have too long of a tail from severe HCAL mis-measurements that are actually rare in the $\gamma\gamma$ sample.

As a cross-check, the ee sample is also used to model the QCD background. This sample of Z decays should have no true \cancel{E}_T , just like the ff sample, and the electron definition (differing from the photon definition only in the presence of a pixel seed) insures that the electron energy scale and resolution is similar to that of the photon.

Finally, the $e\gamma$ sample is used to model the electroweak background from $W \rightarrow e\nu$ decays. The $e\gamma$ \cancel{E}_T distribution is scaled by the electron \rightarrow photon misidentification rate to predict the number of $W\gamma$, $W + \text{jet}$, and $t\bar{t}$ events in the $\gamma\gamma$ sample.

The remainder of this chapter describes the data analysis procedures and the final results of the search. Sec. 4.1 addresses the QCD background estimation. Sec. 4.2

1348 addresses the electroweak background estimation. The chapter concludes with a dis-
 1349 cussion of systematic errors in Sec. 4.3 and a presentation of the final results in
 1350 Sec. 4.4.

1351 4.1 Modeling the QCD Background

1352 4.1.1 Outline of the Procedure

1353 Due to the fact that the CMS ECAL energy resolution is much better than the
 1354 HCAL energy resolution, the energies of the two candidate photons in the events of
 1355 the $\gamma\gamma$ sample are typically measured to far greater accuracy and precision than the
 1356 energy of the hadronic recoil in those events. Therefore, fake E_T in the $\gamma\gamma$ sample
 1357 is almost entirely the result of hadronic mis-measurement in QCD dijet, photon +
 1358 jet, and diphoton events. The strategy employed to model this background is to find
 1359 a control sample in data consisting of two well-measured EM objects, just like the
 1360 candidate $\gamma\gamma$ sample, and assign each event a weight to account for the underlying
 1361 kinematic differences between the control and candidate samples. Once the reweighted
 1362 E_T spectrum of the control sample is created, it is then normalized in the low- E_T
 1363 region, the assumption being that GGM SUSY does not predict a significant amount
 1364 of events at low E_T . There are three aspects of this QCD background estimation
 1365 procedure that bear highlighting:

1366 **Choice of control sample** Since the underlying cause of E_T in the candidate sam-
 1367 ple is mis-measured hadronic activity, a control sample with similar hadronic
 1368 activity to the candidate sample should be chosen. Hadronic activity refers to
 1369 number of jets, jet E_T , pileup, etc.

1370 **Reweighting** The control sample is reweighted so that its E_T spectrum appears as it
 1371 would if the control sample had the same kinematic properties as the candidate

sample (i.e. particle p_T and η distributions, etc.). By choosing an appropriate control sample and reweighting it, the control \cancel{E}_T distribution should now match both the hadronic activity and the kinematics of the candidate sample.

Normalization Finally, the control E_T distribution is normalized in a region of low \cancel{E}_T , where contamination from the expected GGM SUSY signal is small. This implies an extrapolation of the low- \cancel{E}_T QCD background prediction to the high- \cancel{E}_T signal region.

As explained in the beginning of this chapter, the ff sample is used as the primary QCD control sample, while the ee sample is used as a cross-check. Both samples have two well-measured EM objects per event, no real \cancel{E}_T , and similar hadronic activity to the $\gamma\gamma$ sample. Figure 4.3 shows a comparison of the shapes of some distributions relevant to hadronic activity between the $\gamma\gamma$, ee , and ff samples. In general, the ee sample has less hadronic activity than the $\gamma\gamma$ and ff samples, as shown by the more steeply falling ee distributions in Figs. 4.3a, 4.3b, 4.3c, and 4.3d. In addition to the kinematic reweighting, there is also a reweighting by number of jets per event, which attempts to correct for this difference (see Sec. 4.1.2).

4.1.2 Reweighting

To reweight the control sample events to match the kinematics of the candidate sample events, a weight based on the p_T of the di-EM-object system and the number of jets in the event is used. As explained in Sec. 4.1.1, E_T in the $\gamma\gamma$, ff , and ee samples is due to the poorly measured hadronic recoil off the well-measured di-EM system. Therefore, the p_T of the di-EM system is a good handle on the true magnitude of the hadronic recoil, which affects the measured \cancel{E}_T . The di-EM system is depicted in Figure 4.4. As shown in Figure 4.5, \cancel{E}_T is largely uncorrelated with di-EM p_T , so there is little danger of reweighting away a true signal excess.

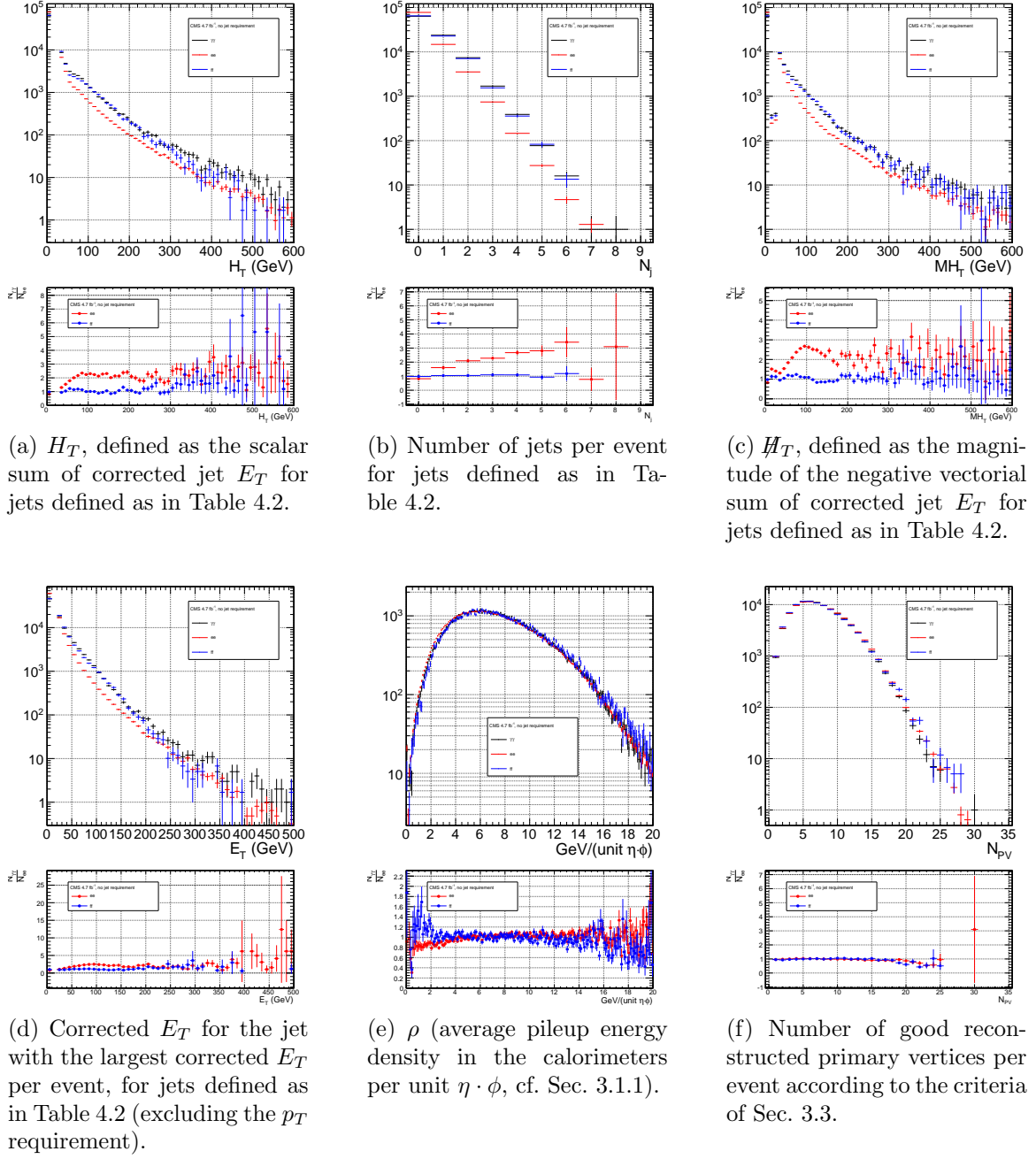


Figure 4.3: Comparison of the shapes of some distributions relevant to hadronic activity between the $\gamma\gamma$, ee ($81 \text{ GeV} \leq m_{ee} < 101 \text{ GeV}$), and ff samples. The ee and ff distributions are normalized to the number of events in the $\gamma\gamma$ distribution. Errors are statistical only.

Table 4.2: Definition of HB/HE/HF hadronic jets.

Variable	Cut
Algorithm	L1FastL2L3Residual corrected PF (cf. Sec. 3.1.3)
p_T	$> 30 \text{ GeV}$
$ \eta $	< 5.0
Neutral hadronic energy fraction	< 0.99
Neutral electromagnetic energy fraction	< 0.99
Number of constituents	> 1
Charged hadronic energy	$> 0.0 \text{ GeV}$ if $ \eta < 2.4$
Number of charged hadrons	> 0 if $ \eta < 2.4$
Charged electromagnetic energy fraction	< 0.99 if $ \eta < 2.4$
ΔR to nearest PF electron ^a , muon ^b , or one of the two primary EM objects	> 0.5

^aA PF electron is defined as an electron reconstructed with the PF algorithm [64] with $p_T > 15 \text{ GeV}$, $|\eta| < 2.6$, and $(I_{\text{charged}} + I_{\text{photon}} + I_{\text{neutral}})/p_T < 0.2$, where $I_{\text{charged}}(I_{\text{photon}})(I_{\text{neutral}})$ is the sum of PF charged hadron(PF photon)(PF neutral hadron) momenta in a $\Delta R = 0.4$ cone around the PF electron.

^bMuons are reconstructed [65] from a combination of muon station and inner tracker hits. Here, a muon must have track $\chi^2 < 10$, at least one good muon station hit, inner track transverse impact parameter $< 0.02 \text{ cm}$, inner track longitudinal impact parameter $< 0.5 \text{ cm}$, $p_T > 15 \text{ GeV}$, $|\eta| < 2.6$, and $(I_{\text{ECAL}} + I_{\text{HCAL}} + I_{\text{track}})/p_T < 0.2$, where $I_{\text{ECAL}}(I_{\text{HCAL}})(I_{\text{track}})$ is the sum of ECAL(HCAL)(track) momenta in a $\Delta R = 0.3$ cone around the muon.

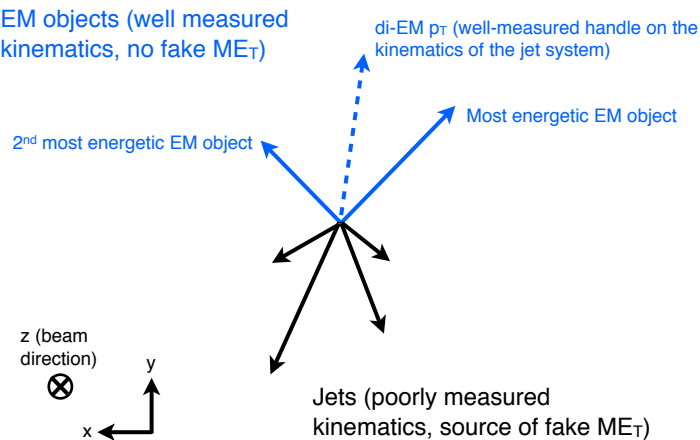


Figure 4.4: Cartoon showing the di-EM system in blue and the hadronic recoil in black. The di-EM p_T (dashed blue line) is used to reweight the control sample kinematic properties to match those of the candidate $\gamma\gamma$ sample.

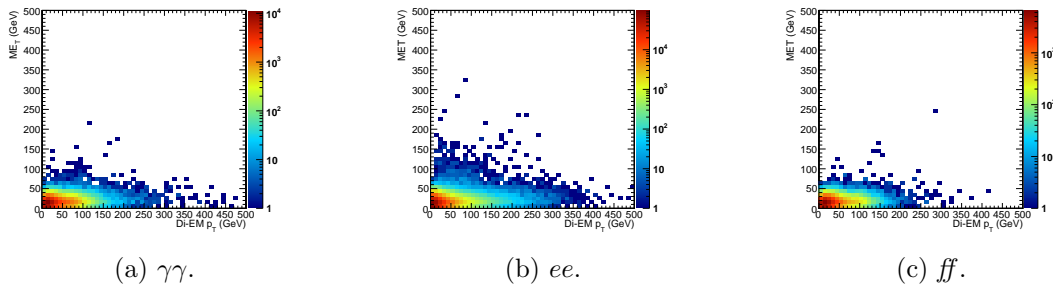


Figure 4.5: E_T vs. di-EM p_T .

Whereas the di-EM p_T reweighting accounts for differences in production kinematics between the control and $\gamma\gamma$ samples, a simultaneous reweighting based on the number of jets in the event accounts for differences in hadronic activity between the samples, especially between ee and $\gamma\gamma$ (cf. Fig. 4.3). Jets are defined as in Table 3.2. Figure 4.6 shows the effect of reweighting by number of jets per event, which is to increase(decrease) the tail of the $ee(ffff)$ E_T spectrum.

1403 Although the electron and photon energies are well measured by the ECAL, the
 1404 ECAL-only measurement of the fake photon energy (cf. Sec 3.1.1) is biased slightly
 1405 low due to the fact that fakes (which are really jets) tend to deposit some energy in
 1406 the HCAL. This can be seen in Figs. 4.7 and 4.8, which show the relative difference
 1407 between the ECAL-only E_T measurement and the PF E_T measurement vs. EMF for
 1408 electrons, photons, and fakes. PF E_T is defined as the L1Fast-corrected E_T of the
 1409 nearest PF jet with $p_T \geq 20$ GeV (i.e., the E_T of the PF jet object reconstructed from
 1410 the same ECAL shower as the fake photon). On average, the fakes tend to deposit
 1411 a few percent more energy in the HCAL than the electrons or photons, which is
 1412 recovered by the PF algorithm. For this reason, the PF p_T is used in the calculation
 1413 of di-EM p_T rather than the ECAL-only p_T .¹ This leads to a modest improvement in
 1414 the agreement between the ee and ff E_T spectra, as shown in Figure 4.9.

1415 The control sample event weights are defined as

¹In the few events ($\mathcal{O}(10^{-3})$) in which two PF jet objects, corresponding to the two electrons or fakes, are not found, the ECAL-only p_T is used.

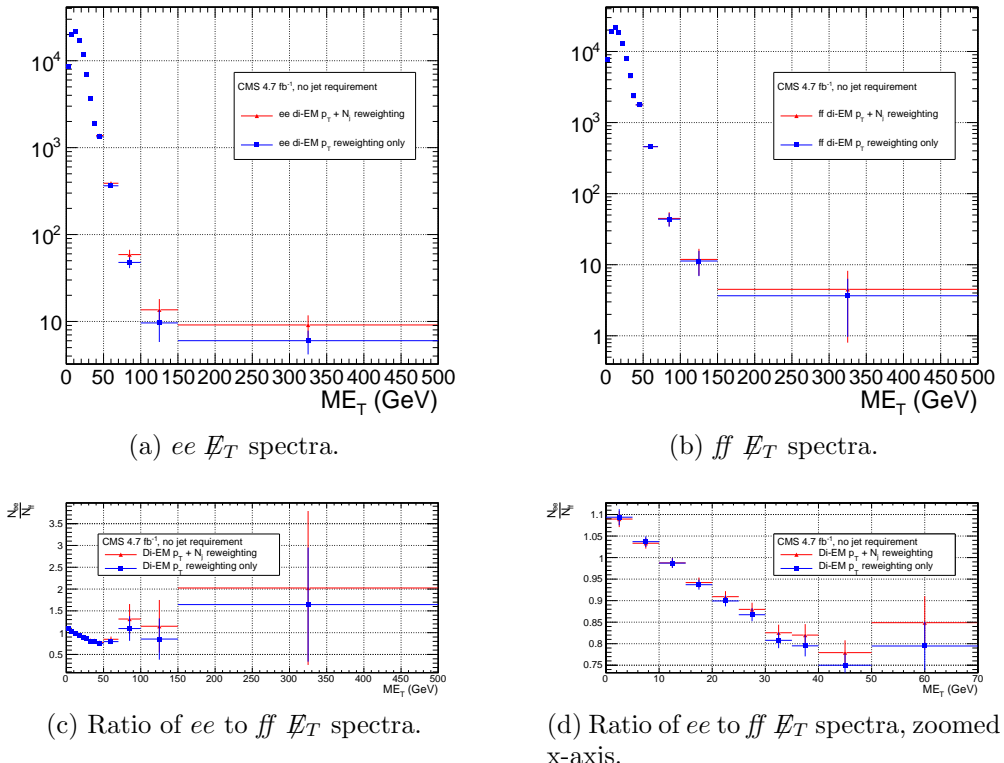


Figure 4.6: \cancel{E}_T spectra of the reweighted ee ($81 \text{ GeV} \leq m_{ee} < 101 \text{ GeV}$) and ff control samples. Blue squares indicate di-EM p_T reweighting only; red triangles indicate di-EM p_T + number of jets reweighting. PF p_T (cf. p. 101) is used to calculate the di-EM p_T . The full normalization procedure is employed, along with ee sideband subtraction (discussed at the end of this section). Error bars are statistical only.

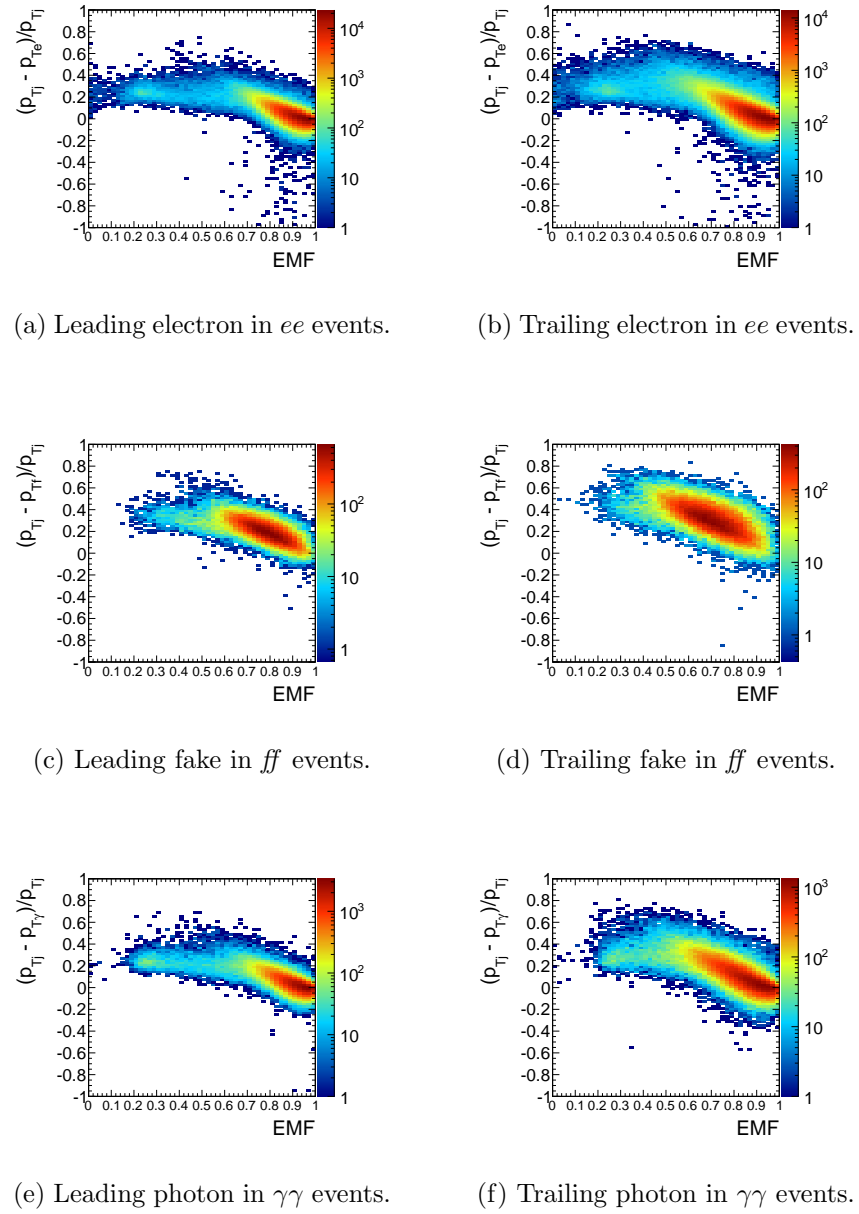


Figure 4.7: Relative difference between the ECAL-only E_T measurement and the PF E_T measurement vs. EMF. PF E_T is defined in the text.

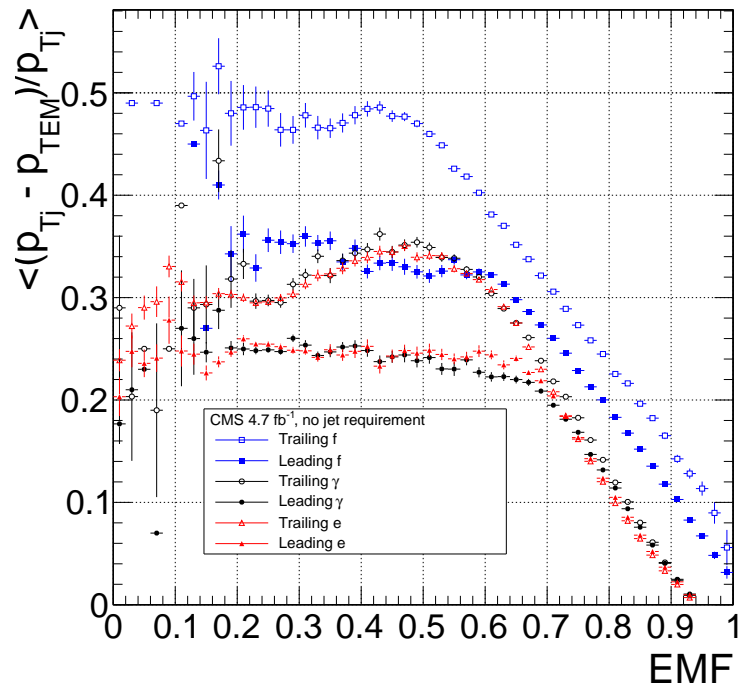


Figure 4.8: Average relative difference between the ECAL-only E_T measurement and the PF E_T measurement vs. EMF for the leading (filled marker) and trailing (open marker) electrons in ee events (red triangles), fakes in ff events (blue squares), and photons in $\gamma\gamma$ events (black circles). These are nothing more than profile histograms of Fig. 4.7. PF E_T is defined in the text. Error bars are statistical only.

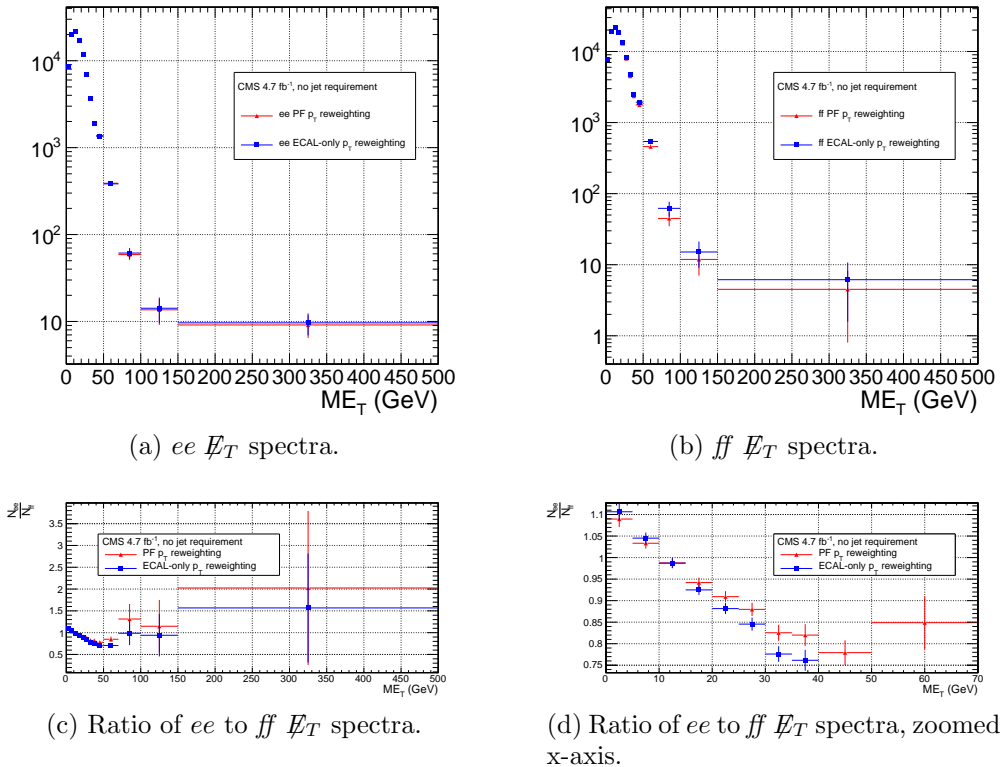


Figure 4.9: E_T spectra of the reweighted ee ($81 \text{ GeV} \leq m_{ee} < 101 \text{ GeV}$) and ff control samples. Blue squares indicate reweighting using the ECAL-only p_T estimate; red triangles indicate reweighting using the PF p_T estimate. The full reweighting and normalization procedure is employed, along with ee sideband subtraction (discussed at the end of this section). Error bars are statistical only.

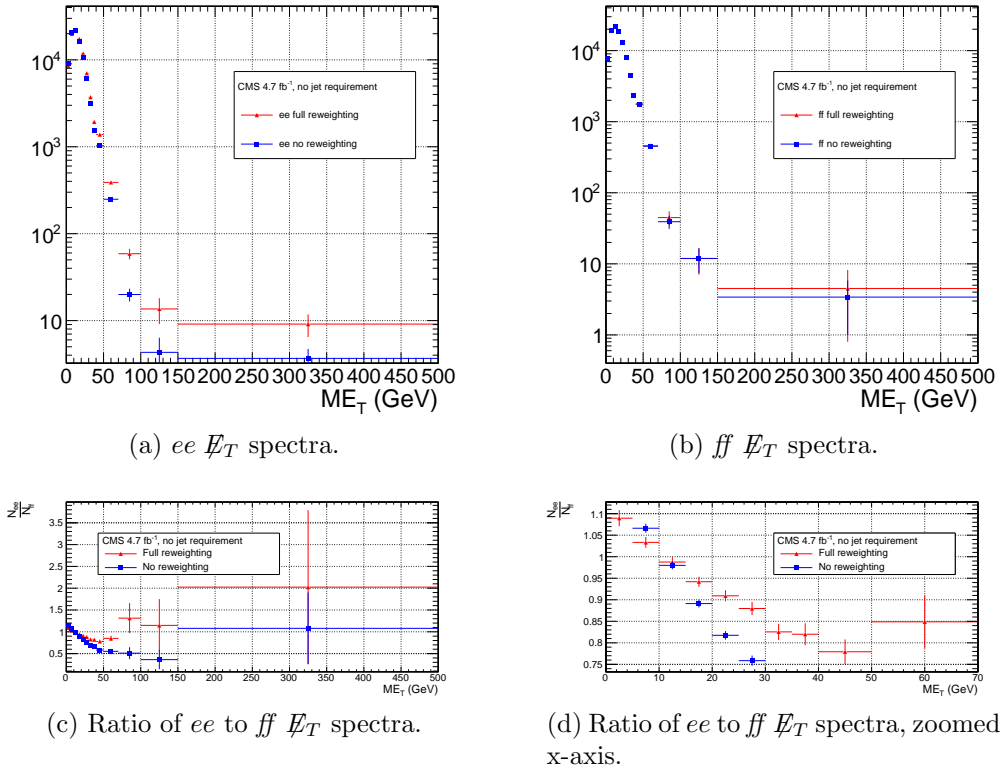


Figure 4.10: E_T spectra of the ee ($81 \text{ GeV} \leq m_{ee} < 101 \text{ GeV}$) and ff control samples. Red triangles indicate full di-EM p_T + number of jets reweighting; blue squares indicate no reweighting. PF p_T (cf. p. 103) is used to calculate the di-EM p_T . The full normalization procedure is employed, along with ee sideband subtraction (discussed at the end of this section). Error bars are statistical only.

$$w_{ij} = \frac{N_{\text{control}}}{N_{\gamma\gamma}} \frac{N_{\gamma\gamma}^{ij}}{N_{\text{control}}^{ij}} \quad (4.1)$$

where i runs over the number of di-EM p_T bins, j runs over the number of jet bins,
 N_{control} is the total number of events in the control sample, $N_{\gamma\gamma}$ is the total number of
events in the $\gamma\gamma$ sample, $N_{\gamma\gamma}^{ij}$ is the number of $\gamma\gamma$ events in the i^{th} di-EM p_T bin and
 j^{th} jet bin, and N_{control}^{ij} is the number of control sample events in the i^{th} di-EM p_T
bin and j^{th} jet bin. The effect of the reweighting is more significant for the ee sample
than for the ff sample, as shown in Figure 4.10.

1422 The ee sample contains a non-negligible background of $t\bar{t}$ events in which both
 1423 W bosons decay to electrons. These events have significant real \cancel{E}_T from the two
 1424 neutrinos (unlike the $\gamma\gamma$ events), and therefore inflate the background estimate at
 1425 high \cancel{E}_T . In order to remove the $t\bar{t}$ contribution from the ee sample, a sideband
 1426 subtraction method is employed.

1427 Only events in the ee sample with $81 \text{ GeV} \leq m_{ee} < 101 \text{ GeV}$, where m_{ee} is the
 1428 di-electron invariant mass, are used in the QCD background estimate. This choice
 1429 maximizes the ratio of Z signal to background. The sidebands used to estimate the
 1430 background contribution within the Z window are defined such that $71 \text{ GeV} \leq m_{ee} <$
 1431 81 GeV and $101 \text{ GeV} \leq m_{ee} < 111 \text{ GeV}$.

1432 The full reweighting procedure is applied to the Z signal region and the two
 1433 sideband regions independently. Only Z signal events are used in the calculation of
 1434 the di-EM p_T weights for the Z signal region, and likewise only the events within
 1435 a given sideband region are used in the calculation of the weights for that region.
 1436 Assuming a constant $t\bar{t}$ background shape, the resulting reweighted sideband \cancel{E}_T
 1437 distributions are added together and subtracted from the reweighted Z signal \cancel{E}_T
 1438 distribution. The sideband subtracted Z signal \cancel{E}_T distribution is then normalized
 1439 as discussed in Secs. 4.1.1 and 4.1.3. The statistical and reweighting error from the
 1440 sideband regions is propagated to the error on the final ee QCD \cancel{E}_T estimate.

1441 The di-EM p_T weights for the two ee sideband regions are shown in Figure 4.11.
 1442 The overall scale of the weights, as well as the trend with di-EM p_T , is similar for
 1443 the two regions (except at high di-EM p_T , where the statistics are poor anyway).
 1444 Figure 4.12 shows the \cancel{E}_T spectra for the two sideband regions and the Z signal
 1445 region after subtraction. The shapes of the spectra indicate that the high- \cancel{E}_T $t\bar{t}$ tail,
 1446 present in the sideband distributions, was successfully subtracted from the Z signal
 1447 distribution.

1448 The ee ($81 \text{ GeV} \leq m_{ee} < 101 \text{ GeV}$), ff , and $\gamma\gamma$ di-EM p_T spectra for events with

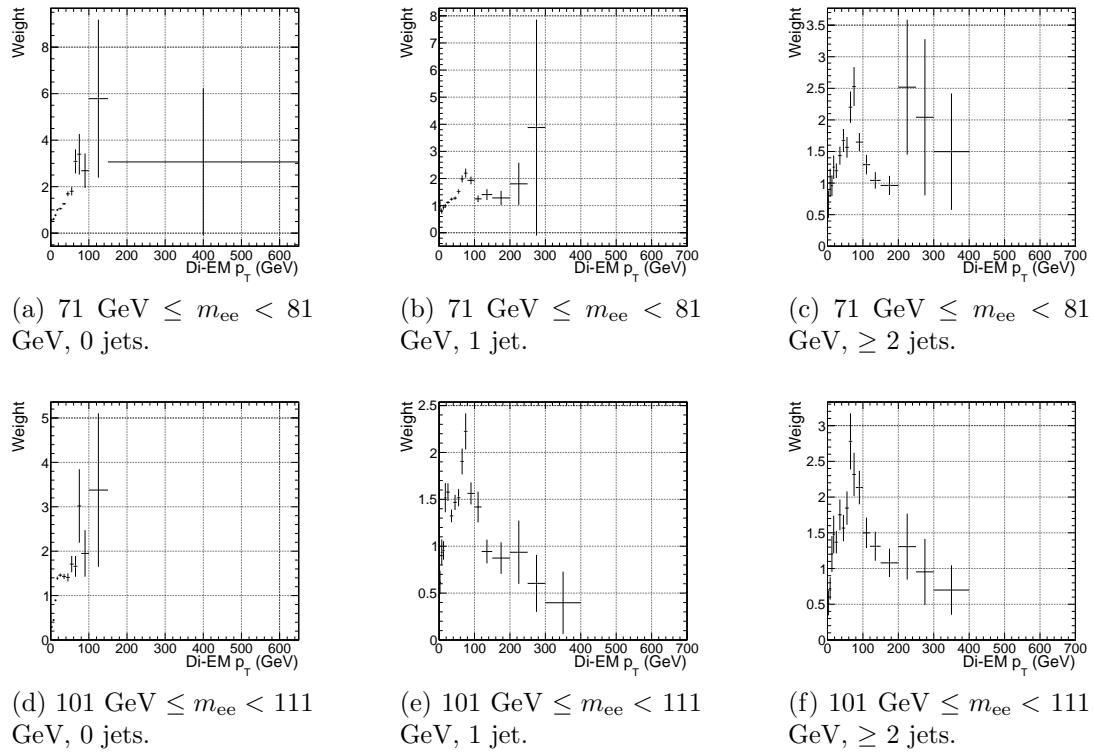


Figure 4.11: ee sideband di-EM p_T weights for events with 0, 1, or ≥ 2 jets (as in Table 3.2). Errors are statistical only.

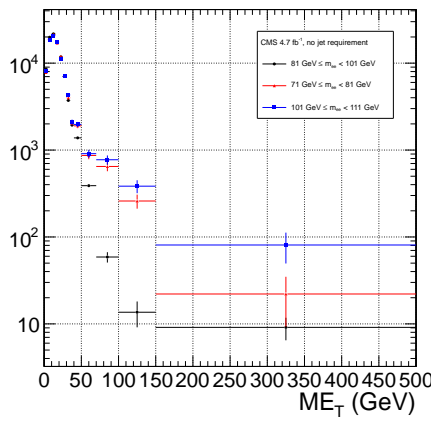


Figure 4.12: E_T spectra of the ee sample for $71 \text{ GeV} \leq m_{ee} < 81 \text{ GeV}$ (red triangles), $81 \text{ GeV} \leq m_{ee} < 101 \text{ GeV}$ (black circles), and $101 \text{ GeV} \leq m_{ee} < 111 \text{ GeV}$ (blue squares). The two sideband distributions (red and blue) and the Z signal distribution (black) are normalized to the total number of $\gamma\gamma$ events. Errors are statistical only.

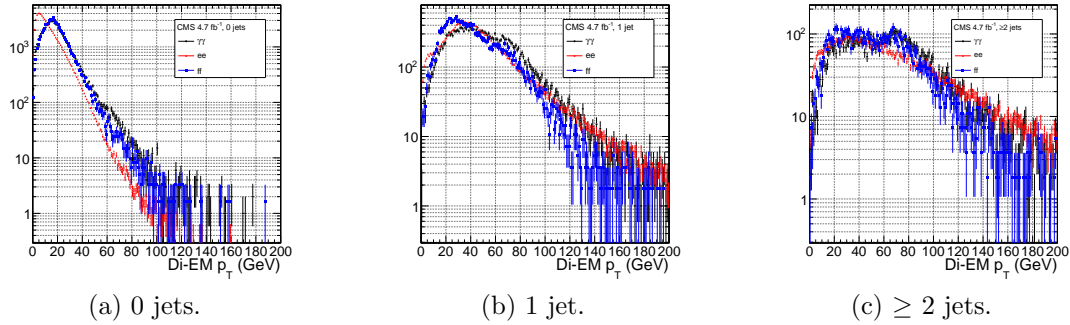


Figure 4.13: ee ($81 \text{ GeV} \leq m_{ee} < 101 \text{ GeV}$) (red triangles), ff (blue squares), and $\gamma\gamma$ (black circles) di-EM p_T spectra for events with 0, 1, or ≥ 2 jets (as in Table 3.2). Errors are statistical only.

1449 0, 1, or ≥ 2 jets (as in Table 3.2) are shown in Figure 4.13. Broad humps in the ff
 1450 and $\gamma\gamma$ spectra are due to kinematic ΔR and p_T turn-ons that are suppressed in the
 1451 ee sample due to the invariant mass cut. Figure 4.14 shows the weights applied to
 1452 the ee ($81 \text{ GeV} \leq m_{ee} < 101 \text{ GeV}$) and ff \cancel{E}_T spectra as a function of di-EM p_T and
 1453 number of jets per event.

1454 4.1.3 Normalization

After reweighting, the \cancel{E}_T distributions of the QCD control samples are normalized to the $\cancel{E}_T < 20$ GeV region of the candidate $\gamma\gamma \cancel{E}_T$ spectrum, where signal contamination is low. The normalization factor is $(N_{\gamma\gamma}^{\cancel{E}_T < 20\text{GeV}} - N_{e\gamma}^{\cancel{E}_T < 20\text{GeV}})/N_{\text{control}}^{\cancel{E}_T < 20\text{GeV}}$, where $N_{e\gamma}^{\cancel{E}_T < 20\text{GeV}}$ is the expected number of electroweak background events with $\cancel{E}_T < 20$ GeV (discussed in Section 4.2).

¹⁴⁶⁰ 4.2 Modeling the Electroweak Background

¹⁴⁶¹ $W\gamma$, $W + \text{jet}$, and $t\bar{t}$ processes in which the W decay electron is misidentified as a
¹⁴⁶² photon (due to a failure to properly associate a pixel seed to the electron candidate)
¹⁴⁶³ can contribute significantly to the high- E_T tail of the $\gamma\gamma E_T$ spectrum. To estimate

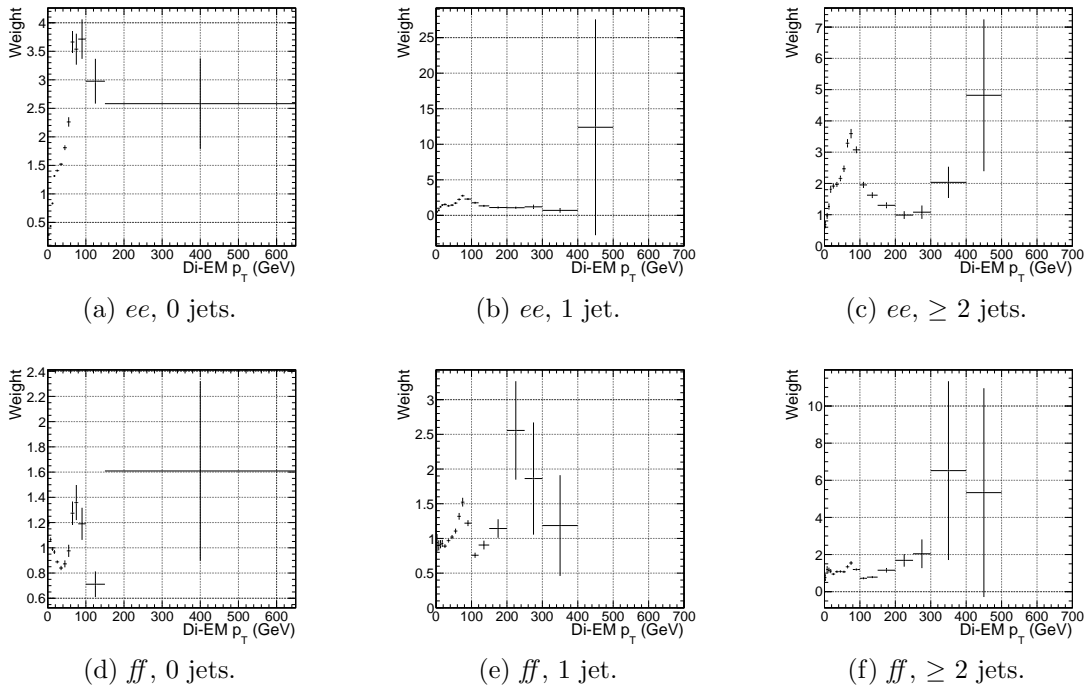


Figure 4.14: ee ($81 \text{ GeV} \leq m_{ee} < 101 \text{ GeV}$) and ff di-EM p_T weights for events with 0, 1, or ≥ 2 jets (as in Table 3.2). Errors are statistical only.

¹⁴⁶⁴ this background, the $e\gamma$ sample, which is enriched in $W \rightarrow e\nu$ decays, is scaled by
¹⁴⁶⁵ $f_{e \rightarrow \gamma}/(1 - f_{e \rightarrow \gamma})$, where $f_{e \rightarrow \gamma}$ is the rate at which electrons are misidentified as photons.
¹⁴⁶⁶ The derivation of this scaling factor comes from the two equations

$$N_{e\gamma}^W = f_{e \rightarrow e} N_W \quad (4.2)$$

$$N_{\gamma\gamma}^W = (1 - f_{e \rightarrow e}) N_W \quad (4.3)$$

¹⁴⁶⁷ where $N_{e\gamma}^W$ is the number of W events in the $e\gamma$ sample in which the electron was
¹⁴⁶⁸ correctly identified, $f_{e \rightarrow e}$ is the probability to correctly identify an electron, N_W is
¹⁴⁶⁹ the true number of triggered $W \rightarrow e\nu$ events, and $N_{\gamma\gamma}^W$ is the number of W events in
¹⁴⁷⁰ the $\gamma\gamma$ sample in which the electron was misidentified as a photon. The contribution
¹⁴⁷¹ from $Z \rightarrow ee$ can be neglected (i.e. $f_{e \rightarrow \gamma}$ is small and the Z contribution involves
¹⁴⁷² $f_{e \rightarrow \gamma}^2$, since both electrons have to be misidentified). Since $f_{e \rightarrow e} = 1 - f_{e \rightarrow \gamma}$, solving

¹⁴⁷³ for $N_{\gamma\gamma}^W$ gives

$$N_{\gamma\gamma}^W = \frac{f_{e\rightarrow\gamma}}{1 - f_{e\rightarrow\gamma}} N_{e\gamma}^W \quad (4.4)$$

¹⁴⁷⁴ $f_{e\rightarrow\gamma}$ is measured by fitting the Z peaks in the ee and $e\gamma$ samples. The number of
¹⁴⁷⁵ Z events fitted in the ee and $e\gamma$ samples, respectively, is given by

$$N_{ee}^Z = (1 - f_{e\rightarrow\gamma})^2 N_Z \quad (4.5)$$

$$N_{e\gamma}^Z = 2f_{e\rightarrow\gamma}(1 - f_{e\rightarrow\gamma}) N_Z \quad (4.6)$$

¹⁴⁷⁶ where N_Z is the true number of triggered $Z \rightarrow ee$ events. Solving for $f_{e\rightarrow\gamma}$ gives

$$f_{e\rightarrow\gamma} = \frac{N_{e\gamma}^Z}{2N_{ee}^Z + N_{e\gamma}^Z} \quad (4.7)$$

¹⁴⁷⁷ A Crystal Ball function is used to model the Z signal shape in both the ee and
¹⁴⁷⁸ $e\gamma$ samples, while an exponential convoluted with an error function (`RooCMSShape`,
¹⁴⁷⁹ see Sec. 3.4.1) is used to model the background shape. The fixed fit parameters are
¹⁴⁸⁰ identical for the two samples, but the other parameters are allowed to float indepen-
¹⁴⁸¹ dently. Table 4.3 shows the values and ranges of the fixed and floating fit parameters,
¹⁴⁸² respectively.

¹⁴⁸³ Fits to the ee and $e\gamma$ invariant mass spectra are shown in Figure 4.15. Figure 4.16
¹⁴⁸⁴ indicates that the dependence of $f_{e\rightarrow\gamma}$ on the electron p_T and η is small. (Note that all
¹⁴⁸⁵ fit parameters are floating in the p_T -dependent fits.) Therefore, a constant misidenti-
¹⁴⁸⁶ fication rate (derived from all ee and $e\gamma$ events), rather than a p_T - and η -dependent
¹⁴⁸⁷ misidentification rate, is used in the final electroweak background estimate, with the

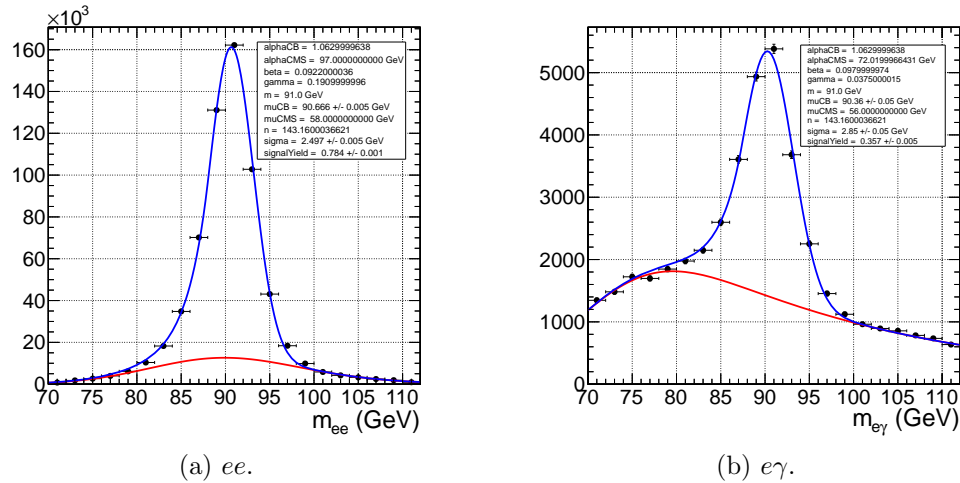


Figure 4.15: Fits to the ee and $e\gamma$ invariant mass spectra using the Crystal Ball RooCMSShape function described in the text and in Table 4.3. The total fit is shown in blue, while the background component is shown in red.

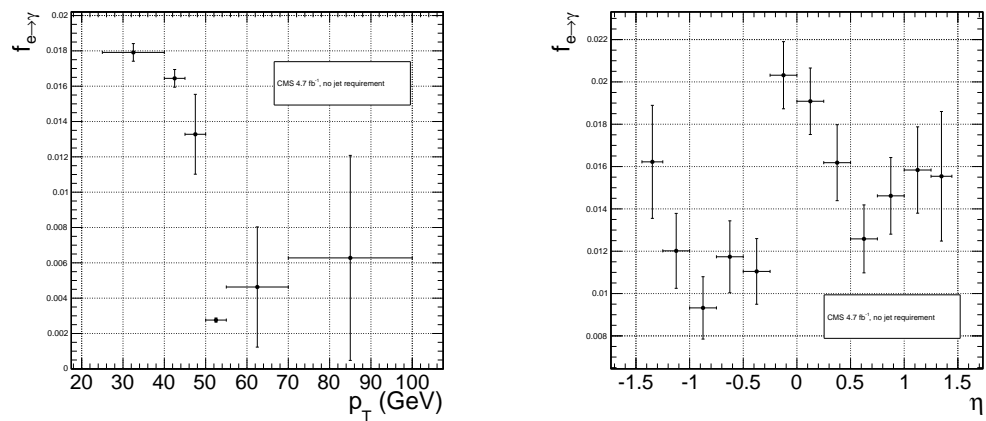
¹⁴⁸⁸ difference between the constant rate and the rate for electrons with p_T between 25
¹⁴⁸⁹ and 40 GeV (the range in which the bulk of the trailing photons in the $\gamma\gamma$ sample
¹⁴⁹⁰ lie) taken as a systematic error.

¹⁴⁹¹ Using the integrals of the Z fits shown in Fig. 4.15, Eq. 4.7, and the p_T systematic
¹⁴⁹² discussed above, $f_{e \rightarrow \gamma}$ is calculated to be $0.014 \pm 0.000(\text{stat.}) \pm 0.004(\text{syst.})$. The
¹⁴⁹³ scaled $e\gamma$ MET distribution is shown in Figure 4.17.

In the 36 pb^{-1} version of this analysis [89], it was shown that the ee sample could accurately predict the QCD and real Z contribution to the $e\gamma$ sample at low \cancel{E}_T , and that the expectation from $W \rightarrow e\nu$ MC accounted for the remaining W contribution at high \cancel{E}_T . A plot of the \cancel{E}_T distributions of the 2010 $e\gamma$ sample and the predicted components is shown in Figure 4.18. This exercise helps to validate both the QCD and electroweak background prediction methods.

Table 4.3: Parameter values for the signal and background PDFs for the ee and $e\gamma$ samples. When a bracketed range is given, the parameter is allowed to float within that range. When a constant is given, the parameter is fixed to that constant.

PDF	Crystal Ball fit parameters				RooCMSShape fit parameters			
	μ	σ	α	n	μ	α	β	γ
ee signal	[86.2, 96.2]	[1.0, 5.0]	1.063	143.16	N/A	N/A	N/A	N/A
$e\gamma$ signal	[86.2, 96.2]	[1.0, 5.0]	1.063	143.16	N/A	N/A	N/A	N/A
ee background	N/A	N/A	N/A	N/A	58	97.0	0.0922	0.191
$e\gamma$ background	N/A	N/A	N/A	N/A	56	72.02	0.098	0.0375



(a) $f_{e \rightarrow \gamma}$ vs. electron p_T . For the lowest p_T bin, the fit to the $e\gamma$ spectrum does not converge well, so the Z signal fraction is fixed to the value in Fig. 4.15b.

(b) $f_{e \rightarrow \gamma}$ vs. electron η .

Figure 4.16: $f_{e \rightarrow \gamma}$ vs. electron p_T and η .

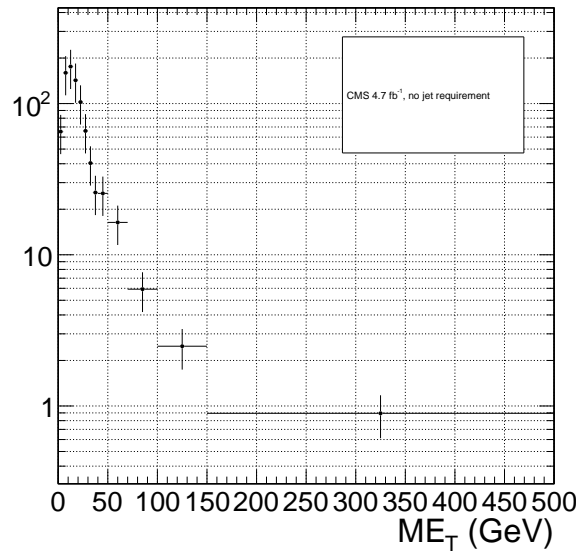


Figure 4.17: E_T spectrum of the $e\gamma$ sample after scaling by $f_{e \rightarrow \gamma}$. The total error on $f_{e \rightarrow \gamma}$ is propagated to the total error on the electroweak background estimate.

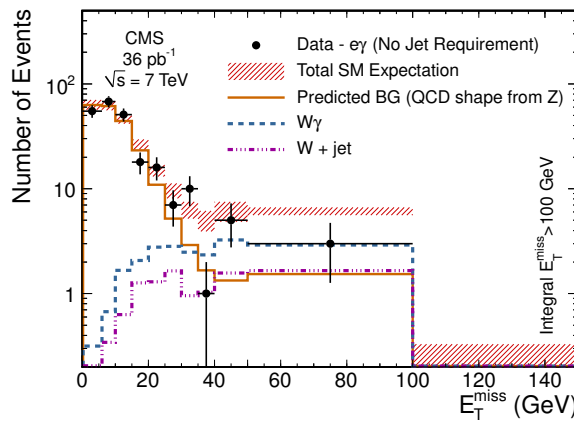


Figure 4.18: E_T spectrum of the $e\gamma$ sample in 36 pb^{-1} of 2010 LHC data scaled by the 2010 measured $f_{e \rightarrow \gamma}$ (black dots), QCD and real Z predicted background from the 2010 ee sample (solid orange line), MC $W + \text{jet}$ estimate (dash-dotted purple line), and MC $W\gamma$ estimate (dashed blue line). The total $e\gamma$ prediction (red band) is the sum of the ee , $W + \text{jet}$, and $W\gamma$ predictions. Reprinted from Fig. 2 of ref. [89].

1500 4.3 Errors on the Background Prediction

1501 The statistical error on the final background estimate in a particular \cancel{E}_T bin comes
 1502 from three sources: the number of control sample events collected in that bin, the
 1503 statistical error on the weights applied to events in that bin, and the statistics of the
 1504 normalization region. In the case of the ee control sample, there are contributions
 1505 from the statistics of the m_{ee} sidebands as well.

1506 In order to estimate the statistical error due to the reweighting procedure, 1000
 1507 toy sets of weights are generated. Each set includes a weight for each (di-EM p_T , N_j)
 1508 bin, with the values picked from a Gaussian distribution with mean and standard
 1509 deviation equal to the observed weight for that bin and its statistical error. The effect
 1510 of reweighting error is not correlated between \cancel{E}_T bins. For each of the 1000 exper-
 1511 iments, the control sample data are reweighted according to the generated weights,
 1512 and the background estimates are calculated for each \cancel{E}_T bin. Since the distribution
 1513 of the toy background estimates follows a Gaussian distribution in each \cancel{E}_T bin, the
 1514 RMS spread of the estimates is taken as the statistical error due to reweighting. This
 1515 procedure is carried out for the ff , ee , low sideband ee , and high sideband ee samples.

1516 The total statistical error on the background estimate per \cancel{E}_T bin is given by

$$\sigma_{\text{stat}}^2 = \sigma_{\text{stat,QCD}}^2 + \sigma_{\text{stat,EW}}^2 \quad (4.8)$$

1517 where $\sigma_{\text{stat,QCD}}^2$ is the square of the total statistical error on the QCD prediction in
 1518 the \cancel{E}_T bin

$$\sigma_{\text{stat,QCD}}^2 = \sigma_{\text{stat},s}^2 + \sigma_{\text{Poisson,QCD}}^2 + \sigma_{\text{reweight},s}^2 + \sigma_{\text{reweight,QCD}}^2 \quad (4.9)$$

1519 and $\sigma_{\text{stat,EW}}$ is the Poisson error on the number of $e\gamma$ events in the \cancel{E}_T bin ($= \sqrt{N_{e\gamma}}$,
 1520 where $N_{e\gamma}$ is the prediction in the \cancel{E}_T bin after scaling by $f_{e\rightarrow\gamma}$). The contributions
 1521 to $\sigma_{\text{stat,QCD}}^2$ are discussed below.

- 1522 • $\sigma_{\text{stat},s}^2$ is the statistical error contributed by the normalization factor s (i.e. from
 1523 Poisson error in the normalization region $\cancel{E}_T < 20$ GeV):

$$\begin{aligned}\sigma_{\text{stat},s}^2 = & \frac{N_{\text{control}}^2}{(N_{\gamma\gamma}^{\text{norm}} - N_{e\gamma}^{\text{norm}})^2} ([\sigma_{\text{Poisson},\gamma\gamma}^{\text{norm}}]^2 + [\sigma_{\text{Poisson},e\gamma}^{\text{norm}}]^2) + \\ & \frac{N_{\text{control}}^2}{(N_{\text{control}}^{\text{norm}})^2} (\sigma_{\text{Poisson,control}}^{\text{norm}})^2\end{aligned}\quad (4.10)$$

1524 where N_{control} is the number of reweighted, normalized events in the \cancel{E}_T bin,
 1525 $N_{\gamma\gamma}^{\text{norm}}$ is the number of $\gamma\gamma$ events in the normalization region, $N_{e\gamma}^{\text{norm}}$ is the num-
 1526 ber of $e\gamma$ events in the normalization region (after scaling by $f_{e\rightarrow\gamma}$), $\sigma_{\text{Poisson},\gamma\gamma}^{\text{norm}}$
 1527 is the Poisson error on the number of $\gamma\gamma$ events in the normalization region
 1528 ($= \sqrt{N_{\gamma\gamma}^{\text{norm}}}$), $\sigma_{\text{Poisson},e\gamma}^{\text{norm}}$ is the Poisson error on the number of $e\gamma$ events in the
 1529 normalization region ($= \sqrt{N_{e\gamma}^{\text{norm}}}$), $N_{\text{control}}^{\text{norm}}$ is the number of QCD control (ee
 1530 or ff) events in the normalization region, and $\sigma_{\text{Poisson,control}}^{\text{norm}}$ is the Poisson error
 1531 on the number of QCD control (ee or ff) events in the normalization region
 1532 ($= \sqrt{\sum_{i=1}^{N_{\text{control}}^{\text{norm}}} w_i^2}$, where w_i is the di-EM p_T weight applied to event i). For
 1533 the ee control region, N_{control} and $N_{\text{control},\text{norm}}$ are sideband subtracted, and
 1534 $\sigma_{\text{Poisson,control}}^{\text{norm}}$ includes the Poisson error on the number of sideband events.

- 1535 • $\sigma_{\text{Poisson,QCD}}$ is the Poisson error due to the number of QCD control (ee or ff)
 1536 events in the \cancel{E}_T bin, equal to $\sqrt{\sum_{i=1}^{N_{\text{control}}^{\text{norm}}} w_i^2}$, where w_i is the di-EM p_T weight
 1537 applied to event i . For the ee control region, $\sigma_{\text{Poisson,QCD}}$ includes the Poisson
 1538 error on the number of subtracted sideband events.
- 1539 • $\sigma_{\text{reweight},s}$ is the error contributed by the control sample reweighting in the nor-

1540 malization region ($= \frac{N_{\text{control}}^2}{(N_{\text{control}}^{\text{norm}})^2} \sigma_{\text{reweight,control}}^{\text{norm}}$). $\sigma_{\text{reweight,control}}^{\text{norm}}$ is the quadrature
 1541 sum of the RMS of the 1000 toy reweighting experiments for each \cancel{E}_T bin in the
 1542 normalization region. For the ee control sample, it also includes (in quadrature)
 1543 the RMS of the toys in the sideband samples.

- 1544 • $\sigma_{\text{reweight,QCD}}$ is the error contributed by the control sample reweighting in the \cancel{E}_T
 1545 bin ($= s\sigma_{\text{reweight,control}}$). $\sigma_{\text{reweight,control}}$ is the RMS of the 1000 toy reweighting
 1546 experiments for the E_T bin. For the ee control sample, it also includes (in
 1547 quadrature) the RMS of the toys in the sideband samples.

1548 The dominant source of systematic error on the background estimate is the slight
 1549 difference in hadronic activity between the ee , ff , and $\gamma\gamma$ samples. This results in a
 1550 small bias (~ 1 GeV) of the ee \cancel{E}_T distribution towards lower values with respect to
 1551 the ff and $\gamma\gamma$ samples, as shown in Figure 4.19. Therefore, the ff sample is used as
 1552 the primary QCD background estimator, and the difference between the ee and ff
 1553 predictions is assigned as an error on the knowledge of the hadronic activity. For \cancel{E}_T
 1554 > 100 GeV, this error amounts to 43% of the total QCD + electroweak background
 1555 estimate.

1556 The second largest source of systematic error comes from the p_T dependence of the
 1557 $e \rightarrow \gamma$ misidentification rate (see 4.2). For $\cancel{E}_T > 100$ GeV, the expected electroweak
 1558 background is 3.4 ± 1.0 events, so this error amounts to 4.8% of the total QCD +
 1559 electroweak background estimate.

1560 The assumption of a constant $t\bar{t}$ and $W + \text{jets}$ background shape under the Z
 1561 peak in the ee sample induces a systematic error on the ee sideband-subtracted back-
 1562 ground prediction. To assess the magnitude of this error, the sideband subtraction
 1563 (see Sec. 4.1.2) is performed once using only the prediction from the high sideband,
 1564 and once using only the prediction from the low sideband. In each of these cases, the
 1565 prediction is weighted by a factor of two, to account for the fact that the sideband
 1566 regions are only half as wide (10 GeV) as the signal region (20 GeV). The maximum

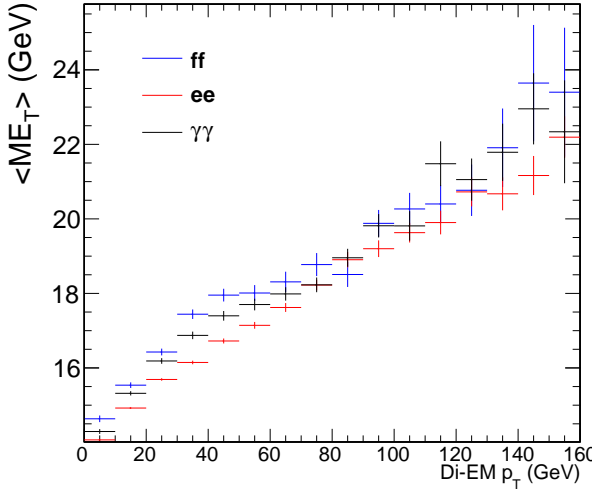


Figure 4.19: Average \mathcal{E}_T vs. di-EM p_T for the ff (blue), ee (red), and $\gamma\gamma$ (black) samples.

1567 variation from the nominal ee estimate is taken as the error, which amounts to 11%
 1568 for $\mathcal{E}_T > 100$ GeV. \mathcal{E}_T distributions using the nominal ee sideband subtraction, the
 1569 low-sideband-only subtraction, and the high-sideband-only subtraction are shown in
 1570 Figure 4.20.

Added

1571 Finally, the few percent error on the jet energy correction factors introduces an this
 1572 error on the final background estimate through (a) the use of the PF p_T to measure para-
 1573 the di-EM p_T , (b) the counting of jets passing a 30 GeV p_T threshold for placement of graph
 1574 the event in an N_j bin for reweighting, and (c) the counting of jets above threshold for
 1575 the ≥ 1 -jet version of the selection. To estimate this error, 100 pseudo-experiments
 1576 are generated with identical properties as the true data sample, except with corrected
 1577 jet energies (in all events) all shifted by an amount $r\sigma(p_T, \eta)$. r is a random number
 1578 drawn from a Gaussian distribution with mean 0 and width 1, and $\sigma(p_T, \eta)$ is the
 1579 uncertainty on the jet energy correction factor (which, like the correction factor itself,
 1580 is a function of p_T and η). The same factor r is applied to all jets in all events in the
 1581 pseudo-experiment because the jet energy correction errors are correlated from jet to
 1582 jet (they result from e.g. uncertainties in MC simulation or uncertainties in ECAL

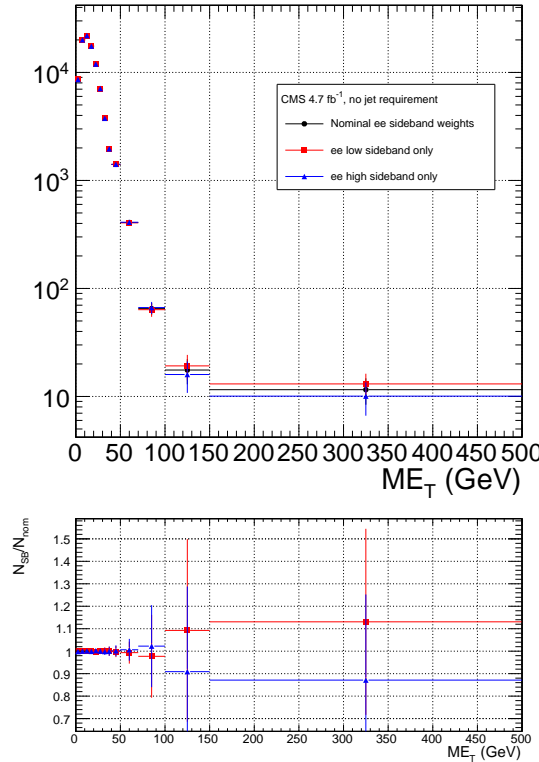


Figure 4.20: ee E_T distributions using the nominal sideband subtraction (black circles), low sideband only (red squares), and high sideband only (blue triangles). The bottom plot shows the ratio of the low sideband distribution to the nominal (red squares) and the ratio of the high sideband distribution to the nominal (blue triangles).

1583 energy scale [69]). The standard error of the mean of the 100 resulting background
 1584 estimates in each relevant E_T bin is taken as the error. The error in each E_T bin is
 1585 assumed to be uncorrelated. This process is repeated for both the inclusive and ≥ 1 -
 1586 jet selections. For $E_T \geq 100$ GeV, the jet energy correction uncertainty is 1.5% (2.2%)
 1587 of the total background for the inclusive (≥ 1 -jet) selection.

1588 The uncertainty in how to define the (di-EM p_T , N_j) bins, especially at high di-
 1589 EM p_T where the statistics are low, is covered by the 1000-toys procedure as long as
 1590 the bins are not too coarse. This is shown in Figure 4.21. If the bins are too coarse,
 1591 the details of the shape of the di-EM p_T spectra are lost, and the reweighting has a
 1592 smaller effect.

1593 The use of uncorrected instead of corrected PF E_T (see Sec. 3.1.3) makes no

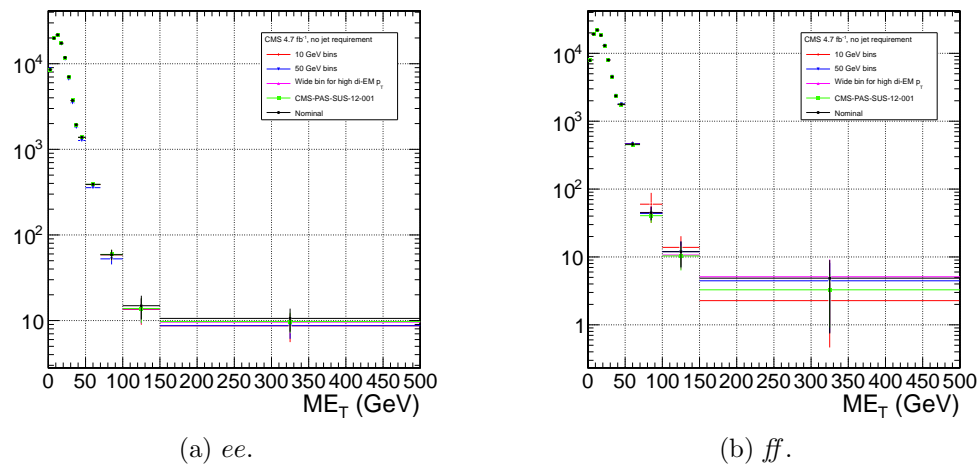


Figure 4.21: Comparison of \cancel{E}_T distributions for five different di-EM p_T bin definitions: uniform bins of width 10 GeV (red diamonds); uniform bins of width 50 GeV (blue downward-pointing triangles); bins with lower edges $\{0.0, 5.0, 10.0, 15.0, 20.0, 30.0, 40.0, 50.0, 60.0, 70.0, 80.0, 100.0, 750.0\}$ GeV for 0-jet events and $\{0.0, 5.0, 10.0, 15.0, 20.0, 30.0, 40.0, 50.0, 60.0, 70.0, 80.0, 100.0, 150.0\}$ GeV for ≥ 1 -jet events (magenta upward-pointing triangles), i.e. a single wide bin at high di-EM p_T ; bins with lower edges $\{0.0, 5.0, 10.0, 15.0, 20.0, 30.0, 40.0, 50.0, 60.0, 70.0, 80.0, 100.0, 150.0\}$ GeV for 0-jet events and $\{0.0, 5.0, 10.0, 15.0, 20.0, 30.0, 40.0, 50.0, 60.0, 70.0, 80.0, 100.0, 120.0, 150.0, 200.0\}$ GeV for ≥ 1 -jet events (green squares), i.e. the bins used in ref. [19]; and the nominal bin definitions shown in Fig. 4.14 (black circles).

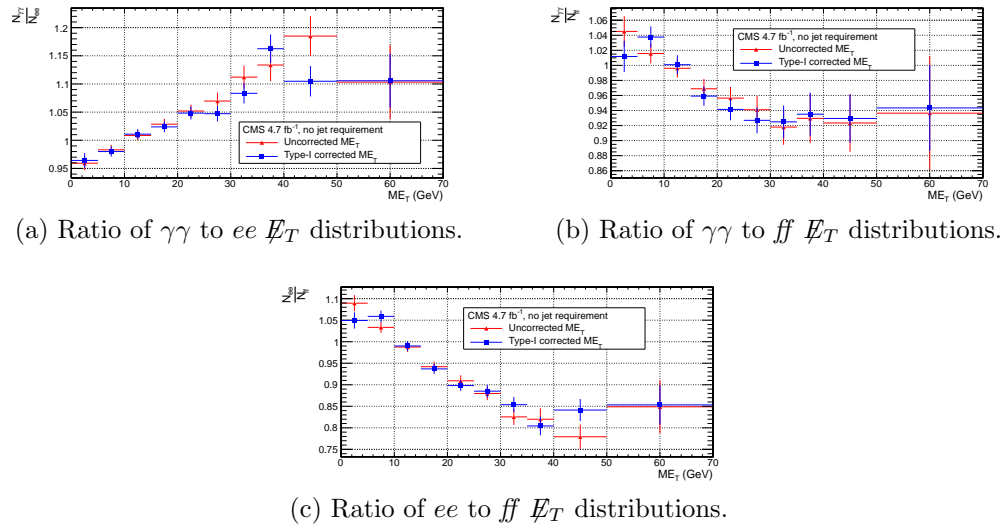


Figure 4.22: Agreement between $\gamma\gamma$, ee , and ff samples for uncorrected (red triangles) and corrected (blue squares) \not{E}_T .

difference in the agreement of the background predictions and the search sample in a control region at low \not{E}_T , as shown in Figure 4.22. Since the control samples are derived from the same data as the search sample, any biases in the \not{E}_T reconstruction due to jet energy scale are present equally in both samples.

Tables 4.4 and 4.5 list all the errors on the ee and ff QCD background predictions, respectively, for the \not{E}_T bins used in the search. Table 4.6 lists the errors on the electroweak background prediction. Finally, Table 4.7 shows the errors on the total QCD + electroweak background prediction, broken down by origin (statistical or systematic) and QCD background estimation sample (ee or ff). In the final result, only the ff QCD estimate is used.

4.4 Results

Figure 4.23(4.24) shows the \not{E}_T distribution of the inclusive(≥ 1 -jet) $\gamma\gamma$ search sample along with the predicted \not{E}_T distributions of the QCD and electroweak backgrounds. The observed number of two-photon events, background estimates and their errors,

Table 4.4: Errors on the ee QCD background prediction as a fraction of the ee prediction.

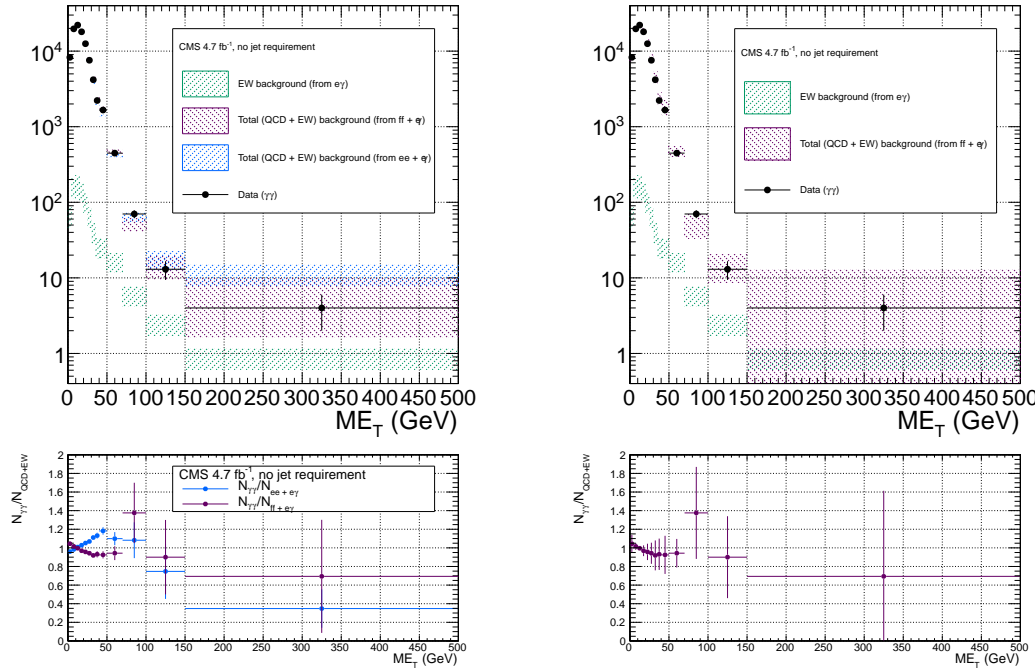
Source of error	Fractional uncertainty (%)				
	[50, 60)	[60, 70)	[70, 80)	[80, 100)	≥ 100
Total	3.9	8.1	16	25	25
Statistics	3.6	7.8	16	24	22
No. events	3.6	7.7	15	24	20
In norm. region	0.43	0.44	0.46	0.55	0.51
In this E_T bin	3.5	7.7	15	24	20
Reweighting	0.73	1.2	3.5	4.3	7.7
In norm. region	0.19	0.19	0.2	0.24	0.23
In this E_T bin	0.71	1.2	3.5	4.3	7.7
Systematics	2.6	4.4	1.2	7.5	14
$f_{e \rightarrow \gamma}$ (in norm. region)	0.0012	0.0012	0.0013	0.0015	0.0014
m_{ee} background shape	1.4	2	0.72	5.5	12
Jet energy scale	2.2	3.9	0.96	5.1	6.9

Table 4.5: Errors on the ff QCD background prediction as a fraction of the ff prediction.

Source of error	Fractional uncertainty (%)				
	[50, 60)	[60, 70)	[70, 80)	[80, 100)	≥ 100
Total	15	25	61	34	64
Statistics	7.2	14	30	33	38
No. events	7.1	14	29	33	36
In norm. region	0.64	0.64	0.64	0.64	0.64
In this E_T bin	7.1	14	29	33	36
Reweighting	0.85	2.7	5.1	6.9	13
In norm. region	0.27	0.27	0.27	0.27	0.27
In this E_T bin	0.81	2.6	5.1	6.9	13
Systematics	13	21	53	6.6	52
ee/ff difference	13	21	53	5.5	52
$f_{e \rightarrow \gamma}$ (in norm. region)	0.0012	0.0012	0.0012	0.0012	0.0012
Jet energy scale	0.099	1.7	1.8	3.5	1.8

Table 4.6: Errors on the $e\gamma$ electroweak background prediction as a fraction of the $e\gamma$ prediction.

Source of error	Fractional uncertainty (%)				
	[50, 60)	[60, 70)	[70, 80)	[80, 100)	≥ 100
Total	29	29	30	30	30
Statistics	3.6	5.2	6.7	7.2	6.5
Systematics ($f_{e \rightarrow \gamma}$)	29	29	29	29	29



(a) $ee + e\gamma$ and $ff + e\gamma$. The widths of the bands correspond to the errors given in Table 4.7, excluding the error associated with the difference between the ee and ff QCD estimates for the $ff + e\gamma$ E_T distribution.

(b) $ff + e\gamma$. The widths of the bands correspond to the errors given in Table 4.7, including the error associated with the difference between the ee and ff QCD estimates.

Figure 4.23: E_T distribution of the $\gamma\gamma$ search sample (black circles) along with the predicted E_T distributions of the QCD and electroweak backgrounds (blue band for ee QCD prediction + electroweak prediction, purple band for ff QCD prediction + electroweak prediction). The electroweak background prediction is shown in green. The bottom plots show the ratio of the $\gamma\gamma E_T$ distribution to the $ee + e\gamma$ background distribution (blue) and $ff + e\gamma$ background distribution (purple).

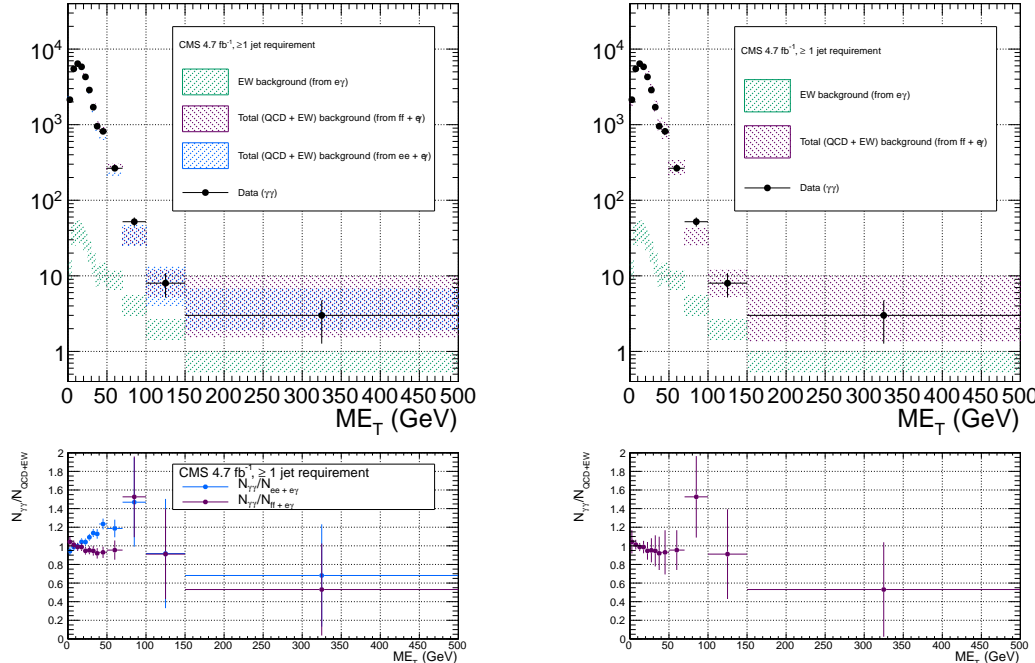
1608 and expected number of inclusive(≥ 1 -jet) two-photon events from two representative
 1609 GGM SUSY models are listed in Table 4.8(4.9). (Details of the SUSY MC production
 1610 are given in Chapter 5 and App. A.) No deviation from the Standard Model prediction
 1611 is observed in the $\gamma\gamma$ search sample.

Table 4.7: Errors on the total QCD + electroweak background prediction as a fraction of the total prediction.

Source of error	Fractional uncertainty (%)				
	[50, 60)	[60, 70)	[70, 80)	[80, 100)	≥ 100
Total ($ee + e\gamma$)	3.9	7.8	15	22	22
Statistics	3.4	7.3	14	21	18
QCD	3.4	7.3	14	21	18
Electroweak	0.13	0.3	0.53	0.79	0.76
Systematics	2.7	4.5	2.6	7.4	13
QCD	2.5	4.1	1.1	6.7	12
Electroweak	1	1.7	2.3	3.2	3.4
Total ($ff + e\gamma$)	14	24	54	30	54
Statistics	6.9	13	26	29	30
QCD	6.9	13	26	29	30
Electroweak	0.11	0.24	0.79	0.83	1.1
Systematics	12	20	47	6.7	43
QCD	12	20	47	5.8	43
Electroweak	0.9	1.3	3.4	3.4	4.8

Table 4.8: Observed numbers of two-photon events, background estimates and their errors, and expected numbers of two-photon events from two representative GGM SUSY models (details of MC simulation given in Chapter 5 and App. A) for the E_T bins used in the search. Errors on the background estimates are detailed in Tables 4.4, 4.5, 4.6, and 4.7. Errors on the expected numbers of GGM events are purely statistical.

Source	No. events				
	[50, 60)	[60, 70)	[70, 80)	[80, 100)	≥ 100
Observation ($\gamma\gamma$)	354	93	37	33	17
Predicted background ($ff + e\gamma$)	361 ± 51.5	113 ± 27.1	26.9 ± 14.5	23.9 ± 7.23	20.2 ± 10.9
$m_{\tilde{q}} = 720$ GeV $M_3 = 720$ GeV $M_1 = 375$ GeV	13.3 ± 2.13	17.7 ± 2.46	15.3 ± 2.33	42.9 ± 3.82	966 ± 18.3
$m_{\tilde{q}} = 1440$ GeV $M_3 = 1440$ GeV $M_1 = 375$ GeV	0.008 ± 0.003	0.009 ± 0.003	0.012 ± 0.003	0.030 ± 0.005	1.92 ± 0.04



(a) $ee + e\gamma$ and $ff + e\gamma$. The widths of the bands correspond to the errors given in Table 4.7, excluding the error associated with the difference between the ee and ff QCD estimates for the $ff + e\gamma$ E_T distribution.

(b) $ff + e\gamma$. The widths of the bands correspond to the errors given in Table 4.7, including the error associated with the difference between the ee and ff QCD estimates.

Figure 4.24: E_T distribution of the $\gamma\gamma + \geq 1$ jet search sample (black circles) along with the predicted E_T distributions of the QCD and electroweak backgrounds (blue band for ee QCD prediction + electroweak prediction, purple band for ff QCD prediction + electroweak prediction). The electroweak background prediction is shown in green. The bottom plots show the ratio of the $\gamma\gamma E_T$ distribution to the $ee + e\gamma$ background distribution (blue) and $ff + e\gamma$ background distribution (purple).

Table 4.9: Observed numbers of two-photon + ≥ 1 -jet events, background estimates and their errors, and expected numbers of two-photon + ≥ 1 -jet events from two representative GGM SUSY models (details of MC simulation given in Chapter 5 and App. A) for the \cancel{E}_T bins used in the search. Errors on the background estimates are detailed in Tables 4.4, 4.5, 4.6, and 4.7. Errors on the expected numbers of GGM events are purely statistical.

Source	No. events				
	[50, 60)	[60, 70)	[70, 80)	[80, 100)	≥ 100
Observation ($\gamma\gamma + \geq 1$ jet)	202	63	27	25	11
Predicted background ($ff + e\gamma$)	200 ± 35.4	77.7 ± 28.1	19.4 ± 8.55	14.7 ± 7.04	14.4 ± 5.59
$m_{\tilde{q}} = 720$ GeV $M_3 = 720$ GeV $M_1 = 375$ GeV	13.3 ± 2.13	17.7 ± 2.46	15.3 ± 2.33	42.9 ± 3.82	965 ± 18.3
$m_{\tilde{q}} = 1440$ GeV $M_3 = 1440$ GeV $M_1 = 375$ GeV	0.008 ± 0.003	0.009 ± 0.003	0.012 ± 0.003	0.031 ± 0.004	1.92 ± 0.04

₁₆₁₂ **Chapter 5**

₁₆₁₃ **Interpretation of Results in Terms
₁₆₁₄ of GMSB Models**

₁₆₁₅ As shown in Figs. 4.23 and 4.24 and Tables 4.8 and 4.9, no excess of events above
₁₆₁₆ the Standard Model expectation is found in either the ≥ 0 - or ≥ 1 -jet analyses for the
₁₆₁₇ GMSB-sensitive region $\cancel{E}_T \geq 50$ GeV. Therefore, upper limits on the production cross
₁₆₁₈ sections of various GMSB models are calculated and then translated into statements of
₁₆₁₉ exclusion. Section 5.1 describes the GMSB models that were generated with MC and
₁₆₂₀ tested for exclusion. The upper limit calculation and translation to model exclusions
₁₆₂₁ is laid out in Section 5.2. The upper limits themselves are presented in Section 5.3,
₁₆₂₂ and, finally, the exclusions are presented in Section 5.4.

₁₆₂₃ **5.1 Simplified Models**

₁₆₂₄ The exclusion reach of the two-photon search is presented for three different two-
₁₆₂₅ dimensional scans in GMSB parameter space. The first scan covers the bino NLSP
₁₆₂₆ scenario of Sec. 1.5. In this scan, M_2 , which controls the amount of wino mixing, is
₁₆₂₇ set to 3.5 TeV. M_1 , which controls the amount of bino mixing, is set to 375 GeV.
₁₆₂₈ This insures that all gauginos except the lightest neutralino are too heavy to be

1629 produced in significant numbers at the LHC. All other mass parameters except for
 1630 M_3 (\sim gluino mass) and $m_{\tilde{q}}$ (\sim first- and second-generation squark mass) are set to
 1631 3.5 TeV, which insures that squark/gluino decay to intermediate states such as third-
 1632 generation squarks or any flavor of lepton is strongly suppressed. M_3 and $m_{\tilde{q}}$ are
 1633 scanned over from $M_3 = m_{\tilde{q}} = 400$ GeV to $M_3 = m_{\tilde{q}} = 2$ TeV in 80-GeV steps.
 1634 The resulting simplified model consists only of a gluino, first- and second-generation
 1635 squarks, and the lightest neutralino and its decay products (the gravitino is forced to
 1636 be the LSP). The scan in M_3 - $m_{\tilde{q}}$ space illuminates the sensitivity of the two-photon
 1637 search to different levels of signal hadronic activity.

1638 The second scan is identical to the first except that the values of M_1 and M_2
 1639 are inverted ($M_1 = 3.5$ TeV and $M_2 = 375$ GeV). This corresponds to the wino
 1640 NLSP scenario of Sec. 1.5. Now, both the lightest neutralino and the lightest chargino
 1641 have masses of order 375 GeV, and are therefore produced with approximately equal
 1642 frequency in the gluino and squark decays. The chargino decays to $W + \tilde{G}$, so final
 1643 states in this scan often include leptons or large jet multiplicity. Since there is no
 1644 guarantee that two neutralinos will be produced and will decay to two photons, this
 1645 search is not well optimized for the wino NLSP scenario. However, a related CMS
 1646 search with one photon and ≥ 3 jets has an exclusion reach of ~ 1 TeV in M_3 and
 1647 $m_{\tilde{q}}$ for this scenario [19].

1648 The third scan is M_3 vs. M_1 for $m_{\tilde{q}}$, M_2 , and all other mass parameters equal to
 1649 2.5 TeV. M_3 is scanned from 160 GeV to 2 TeV in 80-GeV steps, while M_1 is scanned
 1650 from 150 GeV to 1050 GeV in 100-GeV steps. $M_3 < M_1$ is not allowed, as this would
 1651 imply that the gluino, not the lightest neutralino, is the NLSP. This scan highlights
 1652 the performance of the two-photon search as a function of M_1 (i.e. as a function of
 1653 decays open to the neutralino), whereas the previous two scans keep M_1 fixed.

1654 For each scan, the sparticle mass spectrum is generated with SuSpect 2.41 [100]
 1655 and the decay widths with SDECAY 1.3 [101]. The event data (including produc-

tion, unstable particle decay, parton showering, and hadronization) is generated with
 Pythia 6.422 [105], using the sparticle mass spectra and decay widths as inputs. The
 gravitino is always forced to be the LSP. The simulated data are reconstructed with
 CMSSWv4.2.2, which uses a detector simulation based on GEANT 4 [102]. Next to
 leading order cross sections are calculated with PROSPINO 2.1 [103], and shown in
 Figure 5.1 for the three signal MC scenarios.

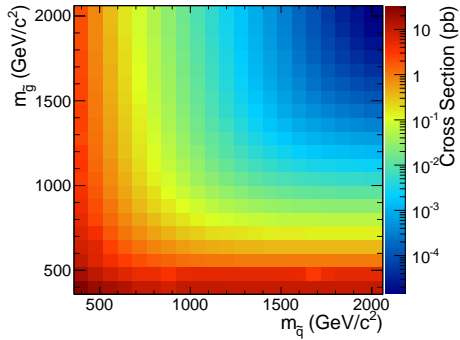
5.2 Upper Limit Calculation and Model Exclusion

The upper limits are calculated according to the prescription followed for the 2011
 ATLAS + CMS Higgs limit combination [90]. This prescription utilizes the frequentist
 CL_s method [91] with profile likelihood test statistic [92]. The CL_s method and the
 profile likelihood are explained in Section 5.2.2, using specific signal MC points to
 illustrate the procedure. First, however, the signal MC acceptance \times efficiency, which
 is an input to the limit setting procedure, is presented in Section 5.2.1.

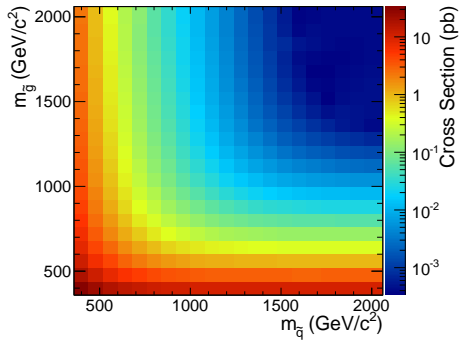
5.2.1 Signal Acceptance \times Efficiency

The signal acceptance \times efficiency (denoted $\mathcal{A} \times \epsilon$), defined for each signal point as
 the number of $\gamma\gamma$ events selected with $\cancel{E}_T \geq 50$ GeV divided by the total number of
 events generated, is shown in Figure 5.2 for the three different scenarios described in
 Sec. 5.1.

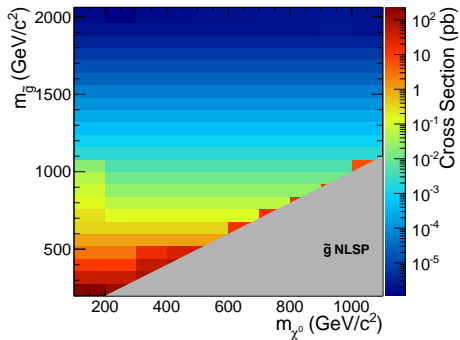
In Figs. 5.2a and 5.2b, the large drop in $\mathcal{A} \times \epsilon$ for $m_{\tilde{q}} > M_3$ is due to an increase
 in the number of jets produced per event and a consequent reduction in the number
 of photons that pass the $I_{\text{comb}} < 6$ GeV cut. For $m_{\tilde{q}} > M_3$, there is more phase space
 available to produce gluinos in the hard scatter than squarks. However, since gluinos
 must decay via squarks, and in these models all squarks are heavier than the gluino,
 only the two-jet decay $\tilde{g} \rightarrow qq\tilde{\chi}^0$ is available. Conversely, when $m_{\tilde{q}} < M_3$, there is



(a) M_2 decoupled ($M_2 = 3.5$ TeV), $M_1 = 375$ GeV, M_3 vs. $m_{\tilde{q}}$.



(b) M_1 decoupled ($M_1 = 3.5$ TeV), $M_2 = 375$ GeV, M_3 vs. $m_{\tilde{q}}$.



(c) $m_{\tilde{q}}$ decoupled ($m_{\tilde{q}} = 2.5$ TeV), M_3 vs. M_1 .

Figure 5.1: Next to leading order cross sections for the three different MC scenarios described in the text.

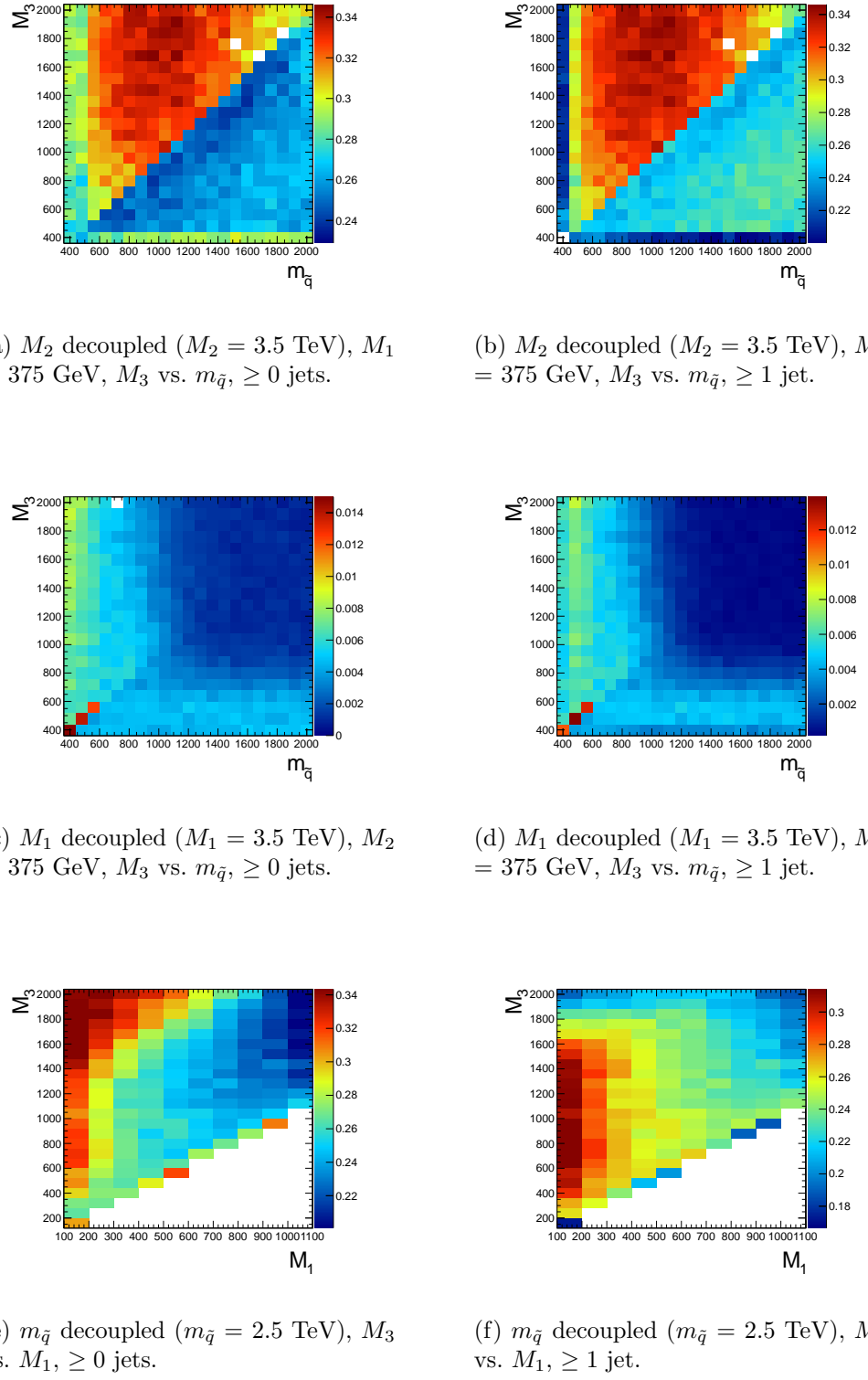


Figure 5.2: Signal acceptance \times efficiency (defined in the text) for the three different scenarios described in Sec. 5.1.

more phase space available to produce squarks, which may then decay via one jet as $\tilde{q} \rightarrow q\tilde{\chi}^0$. Jets in SUSY events may be very close to the neutralino decay photons, and as a result the photons may fail the strict isolation requirements, leading to lower $\mathcal{A} \times \epsilon$ for jet-rich events. The worsened acceptance along $M_3 = 400$ GeV and $m_{\tilde{q}} = 400$ GeV in Fig. 5.2b is due to efficiency of the jet cut, which decreases drastically as M_3 and $m_{\tilde{q}}$ approach M_1 because of shrinking phase space to produce hard jets in the squark and gluino decays to neutralinos.

The broad peak in $\mathcal{A} \times \epsilon$ shown in Fig. 5.2a for $m_{\tilde{q}} < M_3$ and ~ 600 GeV $< m_{\tilde{q}} < \sim 1600$ GeV is due to the $\cancel{E}_T > 50$ GeV cut. The efficiency of the cut decreases as $m_{\tilde{q}}$ decreases because of the fixed M_1 of 375 GeV. If the squark-neutralino mass splitting gets too small, the likelihood of producing an energetic enough gravitino to pass the \cancel{E}_T cut decreases.

$\mathcal{A} \times \epsilon$ is generally much lower for the $M_2 = 375$ GeV grid (Figs. 5.2c and 5.2d) due to the larger contribution from chargino decays to $W + \tilde{G}$, which do not give rise to photons in the final state. The increased acceptance for $M_3 > m_{\tilde{q}}$ is due to the same jet multiplicity issue affecting the $M_1 = 375$ GeV grid. As M_3 and $m_{\tilde{q}}$ increase relative to the fixed M_2 , the jets from squark and gluino decay get more energetic, increasing the chance that they will overlap with the neutralino decay photon and cause it to fail the isolation cut. For $m_{\tilde{q}} \gtrsim 1$ TeV and $M_3 \gtrsim 800$ GeV, the acceptance is so low that not enough events were simulated to see the acceptance decrease over the statistical error.

In Fig. 5.2e, the neutralino is always heavy enough to guarantee decay to a photon that can pass the 40 GeV p_T cut. $\mathcal{A} \times \epsilon$ increases as M_3 increases because the larger gluino-neutralino mass splitting gives the neutralino a larger kinetic energy, increasing the chance that it will decay to a photon with 40 GeV p_T or higher. After the bino mass increases beyond the threshold needed to produce high p_T photons, $\mathcal{A} \times \epsilon$ decreases with increasing M_1 , independent of gluino mass, because higher M_1 means more phase

1707 space is open to decays of the form $\tilde{\chi}_1^0 \rightarrow Z\tilde{G}$ and $\tilde{\chi}_1^0 \rightarrow H\tilde{G}$. The two-photon search
 1708 is naturally not as efficient for these decays.

Added

1709 There is a small chance that some real GMSB signal events could be reconstructed signal
 1710 as ff events in the data. To correct the signal acceptance for this effect, the number contamination
 1711 of signal events reconstructed as ff events is subtracted from the number of signal $\gamma\gamma$ ination
 1712 events, effectively reducing the signal acceptance. This is generally a small correction par.
 1713 ($\sim 5\%$).

1714 5.2.2 CL_s and the Profile Likelihood Test Statistic

1715 The process of setting a cross section upper limit entails (1) defining a test statistic,
 1716 (2) generating a distribution for that test statistic under the signal + background
 1717 and background-only hypotheses, and (3) deciding whether or not the observed value
 1718 of the test statistic is more compatible with the signal + background (i.e. weaker
 1719 upper limit) or background-only (i.e. stronger upper limit) hypotheses by considering
 1720 where it falls within the test statistic distributions. An important requirement on the
 1721 choice of test statistic is that it be able to effectively discriminate between the signal
 1722 + background and background-only hypotheses, i.e. the shape of its distribution for
 1723 these two hypotheses should be different. The procedure for determining the exclud-
 1724 ability of a particular model given the value of the test statistic observed should not
 1725 give rise to pathological behavior in the presence of small signals, low statistics, or
 1726 weak sensitivity to models, as is commonly the case in high energy physics. These
 1727 demands on the test statistic and the limit setting procedure itself dictate the choice
 1728 of the profile likelihood test statistic and CL_s procedure.

1729 In the remainder of this section, the notation is taken from ref. [90].

1730 **Profile Likelihood**

1731 For a specific model of GMSB, the limit setting procedure concerns the question of
 1732 whether to reject the signal + background hypothesis $\mu s + b$ in favor of the background-
 1733 only (Standard Model) hypothesis of b ($\mu = 0$). μ is a dimensionless signal strength
 1734 parameter. s is the expected number of signal events, calculated from MC simulated
 1735 signal events as in Secs. 5.1 and 5.2.1. b is the expected number of background events,
 1736 estimated in Chap. 4. By the Neyman-Pearson lemma [93], the ratio of the likelihood
 1737 of $\mu s + b$ to the likelihood of b is the test statistic with the highest power to reject $\mu s + b$
 1738 at whatever confidence level is desired. In practice, this means that the likelihood ratio
 1739 is the best discriminator between the GMSB and Standard Model hypotheses.

1740 The likelihood of the signal + background hypothesis as a function of the data
 1741 (either real or generated) is defined as

$$\mathcal{L}(\text{data}|\mu, \theta) = \prod_{i=1}^N \frac{(\mu s_i(\theta) + b_i(\theta))^{n_i}}{n_i!} e^{-\mu s_i(\theta) - b_i(\theta)} p(\tilde{\theta}|\theta) \quad (5.1)$$

1742 where $N = 5$ is the number of E_T bins used in the analysis ([50, 60) GeV, [60,
 1743 70) GeV, [70, 80) GeV, [80, 100) GeV, and [100, ∞) GeV); $s_i(\theta)$ and $b_i(\theta)$ are the
 1744 expected number of signal and background events in E_T bin i , respectively; n_i is the
 1745 number of events observed in E_T bin i ; and θ represents all the nuisance parameters
 1746 (uncertainties). $p(\tilde{\theta}|\theta)$ represents the product of probability distribution functions
 1747 (PDFs) for the nuisance parameters, where $\tilde{\theta}$ is the default value of the nuisance
 1748 parameter. In this analysis, there are eight experimental nuisance parameters per E_T
 1749 bin, given here as relative errors on the expected number of signal events:

- 1750 • Uncertainty on the measured integrated luminosity (4.5% in all bins) [94]
- 1751 • Uncertainty on the signal acceptance due to $\epsilon_e^{\text{data}}/\epsilon_e^{\text{MC}}$ and the pixel veto effi-
 1752 ciency error (cf. Sec. 3.4.2) (8% in all bins)

1753 ● Uncertainty on the signal acceptance due to imperfect pileup simulation (2.6%
 1754 in all bins)

1755 ● Systematic uncertainty on QCD background prediction due to difference be-
 1756 tween ff and ee estimates (5.5%-53% of the QCD background depending on
 1757 bin)

1758 ● Systematic uncertainty on electroweak background prediction due to p_T depen-
 1759 dence of $f_{e \rightarrow \gamma}$ (29%-30% of the electroweak background depending on bin)

1760 ● Statistical uncertainty on the signal acceptance (1.8%-100% depending on model
 1761 and bin)

1762 ● Statistical uncertainty on the QCD background prediction (7.2%-38% of the
 1763 QCD background depending on bin)

1764 ● Statistical uncertainty on the electroweak background prediction (3.6%-7.2% of
 1765 the electroweak background depending on bin)

1766 and one very small theoretical nuisance parameter: the uncertainty on the signal
 1767 acceptance due to underlying parton distribution function (PDF) uncertainties. In
 1768 the limit-setting code, the uncertainties on signal acceptance due to photon efficiency
 1769 and PDF errors are added in quadrature and treated as one. The uncertainty on the
 1770 signal acceptance due to jet energy correction uncertainties is negligible, due to the
 1771 presence of many hard jets in GMSB signal events. The uncertainties on integrated
 1772 luminosity and pileup are 100% correlated between \cancel{E}_T bins, and the uncertainty on
 1773 signal acceptance can usually be treated similarly because the error on $\epsilon_e^{\text{data}}/\epsilon_e^{\text{MC}}$ often
 1774 dominates the PDF error on acceptance (although these three uncertainties are 0%
 1775 correlated with each other).

1776 To estimate the uncertainty due to imperfect simulation of LHC pileup, the square
 1777 of the average data efficiency for photons over the range 1-15 reconstructed primary

vertices (see Fig. 3.17a), weighted by the number of $\gamma\gamma$ events per primary vertex bin, is calculated. The efficiency per primary vertex bin is estimated from a linear fit to Fig. 3.17a. The process is repeated for MC using the entire range of primary vertices in Fig. 3.17a (all MC signal points have the same pileup simulation). The error is taken as $2 \times |\text{avg. data efficiency squared} - \text{avg. MC efficiency squared}| / (\text{avg. data efficiency squared} + \text{avg. MC efficiency squared})$.

Each nuisance parameter PDF is modeled by a log-normal distribution:

$$p(\tilde{\theta}|\theta) = \frac{1}{\sqrt{2\pi} \ln \kappa} \exp\left(-\frac{(\ln \tilde{\theta}/\theta)^2}{2(\ln \kappa)^2}\right) \frac{1}{\tilde{\theta}} \quad (5.2)$$

where $\tilde{\theta} = 1$ and $\kappa = 1 +$ the one-standard-deviation relative error on the nuisance parameter (e.g. for the 4.5% error due to integrated luminosity, $\kappa = 1.045$).

Similarly, the likelihood of the background-only hypothesis as a function of the data (either real or generated) is defined as

$$\mathcal{L}(\text{data}|0, \theta) = \prod_{i=1}^N \frac{b_i(\theta)^{n_i}}{n_i!} e^{-b_i(\theta)} p(\tilde{\theta}|\theta) \quad (5.3)$$

The profile likelihood test statistic is defined as

$$\tilde{q}_\mu = -2 \ln \frac{\mathcal{L}(\text{data}|\mu, \hat{\theta}_\mu)}{\mathcal{L}(\text{data}|\hat{\mu}, \hat{\theta})}, 0 \leq \hat{\mu} \leq \mu \quad (5.4)$$

where the $\hat{\theta}_\mu$ maximize $\mathcal{L}(\text{data}|\mu, \hat{\theta}_\mu)$ when it is evaluated at a particular μ , and $\hat{\mu}$ and $\hat{\theta}$ are the global maximum likelihood estimators of μ and θ . The condition $\hat{\mu} \leq \mu$ insures that the obtained cross section upper limit is one-sided, i.e. there is no possibility to find a lower limit on the cross section. The profile likelihood test

1794 statistic has the nice property that in the asymptotic (large statistics) limit its PDF
 1795 can be approximated by analytic formulae, eliminating the need to generate multiple
 1796 toy experiments to get the PDF. However, the approximation breaks down for small
 1797 numbers of observed events, so in practice the asymptotic limit is only used as a first
 1798 guess at the location of the true limit.

1799 The PDFs $f(\tilde{q}_\mu | \mu, \hat{\theta}_\mu^{\text{obs}})$ and $f(\tilde{q}_\mu | 0, \hat{\theta}_0^{\text{obs}})$ for the profile likelihood test statistic
 1800 under the signal + background and background-only hypotheses, respectively, are
 1801 obtained by generating toy MC pseudo-experiments. $\hat{\theta}_\mu^{\text{obs}}$ and $\hat{\theta}_0^{\text{obs}}$ maximize Eqs. 5.1
 1802 and 5.3, respectively, when they are evaluated for the observed data. For each μ (and
 1803 the background-only hypothesis $\mu = 0$), the pseudo-experiments are generated by
 1804 picking random values of s and b from a Poisson distribution with the θ fixed as just
 1805 described.

1806 **CL_s**

1807 In the classical frequentist approach, a signal model may be excluded at the 95%
 1808 confidence level (CL) if the probability of any measurement of the test statistic to be
 1809 greater than or equal to the observed value given the signal + background hypothesis
 1810 is 5%. This means that the observed value of the test statistic is so incompatible
 1811 with what one would expect to observe if the signal model were true that, under the
 1812 assumption that the signal model *is* true, the chance of observing a test statistic even
 1813 further afield from the signal expectation is only 5%. Mathematically,

$$p_\mu \equiv P(\tilde{q}_\mu \geq \tilde{q}_\mu^{\text{obs}} | \mu s + b) = \int_{\tilde{q}_\mu^{\text{obs}}}^{\infty} f(\tilde{q}_\mu | \mu, \hat{\theta}_\mu^{\text{obs}}) d\tilde{q}_\mu \quad (5.5)$$

$$p_\mu \leq 0.05 \Rightarrow \text{exclude } \mu$$

1814 where $\tilde{q}_\mu^{\text{obs}}$ is the observed value of the test statistic and p_μ is the p-value. As indicated
 1815 in Eq. 5.5, the p-value is simply the integral of the PDF of \tilde{q}_μ from $\tilde{q}_\mu^{\text{obs}}$ to infinity.

1816 By construction, the classical 95% CL frequentist approach described above will
 1817 reject a true signal + background hypothesis 5% of the time. This can happen if the
 1818 experiment gets “unlucky” and the observation fluctuates low, causing $\tilde{q}_\mu^{\text{obs}}$ to fall in
 1819 the tail of the \tilde{q}_μ distribution. This poses a problem for the case of very weak signals
 1820 ($\mu \sim 0$), because it will lead to spurious exclusions of models to which the experiment
 1821 has little sensitivity. To avoid this pitfall, the CL_s limit setting method is used.

1822 In the CL_s method, the classical frequentist p-value of Eq. 5.5 is simply divided by
 1823 one minus the p-value of the background-only hypothesis, and it is this ratio, rather
 1824 than the p-value of the signal + background hypothesis alone, that is required to be
 1825 ≤ 0.05 . Mathematically,

$$1 - p_0 \equiv P(\tilde{q}_\mu \geq \tilde{q}_\mu^{\text{obs}} | b) = \int_{\tilde{q}_\mu^{\text{obs}}}^{\infty} f(\tilde{q}_\mu | 0, \hat{\theta}_0^{\text{obs}}) d\tilde{q}_\mu \quad (5.6)$$

$$\text{CL}_s(\mu) \equiv \frac{p_\mu}{1 - p_0} \quad (5.7)$$

$$\text{CL}_s(\mu) \leq 0.05 \Rightarrow \text{exclude } \mu$$

1826 where p_0 is the p-value for the background-only hypothesis ($\mu = 0$). In the case of
 1827 low sensitivity to μ , $p_\mu \lesssim 1 - p_0$, so $\text{CL}_s(\mu) \lesssim 1$ and μ will not be excluded. On the
 1828 contrary, for high sensitivity to μ ($\mu s \gg \sigma_b$), $p_\mu \ll 1 - p_0$, so models that can be
 1829 excluded by the criterion $p_\mu \leq 0.05$ will also be excluded by the criterion $\text{CL}_s \leq 0.05$.
 1830 Compared to the classical frequentist method, CL_s limits can be a little stronger in
 1831 the case of low signal sensitivity [90].

1832 To determine the upper limit on the cross section of a particular model, the lowest
 1833 value of μ for which $\text{CL}_s(\mu) \leq 0.05$, denoted $\mu^{95\% \text{CL}}$, is found. The cross section upper
 1834 limit of that model is then simply $\mu^{95\% \text{CL}}$ multiplied by the expected cross section of

1835 the model (cf. Fig. 5.1).

1836 In contrast to the observed upper limit, the expected upper limit is calculated from
 1837 an ensemble of background-only MC pseudo-experiments. The distribution $f(\mu_{\text{pseudo}}^{\text{95%CL}})$
 1838 is plotted (one entry per pseudo-experiment). The median expected upper limits and
 1839 $\pm 1\sigma$ and $\pm 2\sigma$ bands are defined as

$$0.5 = \int_0^{\mu_{\text{exp}}^{\text{95%CL}}} f(\mu_{\text{pseudo}}^{\text{95%CL}}) d\mu_{\text{pseudo}}^{\text{95%CL}} \quad (5.8)$$

$$0.16 = \int_0^{\mu_{-1\sigma,\text{exp}}^{\text{95%CL}}} f(\mu_{\text{pseudo}}^{\text{95%CL}}) d\mu_{\text{pseudo}}^{\text{95%CL}} \quad (5.9)$$

$$0.84 = \int_0^{\mu_{+1\sigma,\text{exp}}^{\text{95%CL}}} f(\mu_{\text{pseudo}}^{\text{95%CL}}) d\mu_{\text{pseudo}}^{\text{95%CL}} \quad (5.10)$$

$$0.025 = \int_0^{\mu_{-2\sigma,\text{exp}}^{\text{95%CL}}} f(\mu_{\text{pseudo}}^{\text{95%CL}}) d\mu_{\text{pseudo}}^{\text{95%CL}} \quad (5.11)$$

$$0.975 = \int_0^{\mu_{+2\sigma,\text{exp}}^{\text{95%CL}}} f(\mu_{\text{pseudo}}^{\text{95%CL}}) d\mu_{\text{pseudo}}^{\text{95%CL}} \quad (5.12)$$

1840 The technical procedure followed to calculate the 95% CL cross section upper
 1841 limits for each GMSB model tested is given below.

1842 1. Calculate a guess for the median expected limit and $\pm 2\sigma$ error bands ($\mu_{\pm 2\sigma,\text{guess}}^{\text{95%CL}}$)
 1843 using the asymptotic formulae for $f(\tilde{q}_\mu | 0, \hat{\theta}_0^{\text{obs}})$.

1844 2. Calculate observed ($\mu_{\text{obs,asym}}^{\text{95%CL}}$), median expected ($\mu_{\text{exp,asym}}^{\text{95%CL}}$), and $\pm 1\sigma$ ($\mu_{\pm 1\sigma,\text{asym}}^{\text{95%CL}}$)
 1845 and $\pm 2\sigma$ ($\mu_{\pm 2\sigma,\text{asym}}^{\text{95%CL}}$) expected CL_s limits using the asymptotic formulae for
 1846 $f(\tilde{q}_\mu | \mu, \hat{\theta}_\mu^{\text{obs}})$ and $f(\tilde{q}_\mu | 0, \hat{\theta}_0^{\text{obs}})$. Restrict the range of $\mu_{\text{obs,asym}}^{\text{95%CL}}$ and $\mu_{\text{exp,asym}}^{\text{95%CL}}$ to
 1847 $[0, 5 \times \mu_{\pm 2\sigma,\text{guess}}^{\text{95%CL}}]$ (this avoids pathological behavior of the limit-setting code
 1848 when the expected number of signal events is much greater than the observed
 1849 number of events and only introduces a $\sim 5\%$ upward bias in the observed limit,
 1850 well within the $\pm 1\sigma$ error bands).

1851 3. Calculate median expected ($\mu_{\text{exp}}^{\text{95%CL}}$) and $\pm 1\sigma$ ($\mu_{\pm 1\sigma}^{\text{95%CL}}$) and $\pm 2\sigma$ ($\mu_{\pm 2\sigma}^{\text{95%CL}}$) ex-

1852 pected CL_s limits using 100 toy MC pseudo-experiments to generate $f(\tilde{q}_\mu|\mu, \hat{\theta}_\mu^{\text{obs}})$
 1853 and $f(\tilde{q}_\mu|0, \hat{\theta}_0^{\text{obs}})$. Restrict the range of $\mu_{\text{exp}}^{95\%CL}$ to $[0, 5 \times \mu_{\pm 2\sigma, \text{guess}}^{95\%CL}]$.

1854 4. If $\mu_{\pm 2\sigma}^{95\%CL}$ could not be calculated, set $\mu_{\pm 2\sigma}^{95\%CL} = \mu_{\pm 2\sigma, \text{asym}}^{95\%CL}$ instead.

1855 5. If $\mu_{+2\sigma}^{95\%CL} \neq \mu_{-2\sigma}^{95\%CL}$ and $\mu_{\text{obs}, \text{asym}}^{95\%CL} > 0.0001$:

1856 • If $\mu_{\text{obs}, \text{asym}}^{95\%CL} > \mu_{+2\sigma}^{95\%CL}$, set $\mu_{+2\sigma}^{95\%CL} = 1.3 \times \mu_{\text{obs}, \text{asym}}^{95\%CL}$.

1857 • If $\mu_{\text{obs}, \text{asym}}^{95\%CL} < \mu_{-2\sigma}^{95\%CL}$, set $\mu_{-2\sigma}^{95\%CL} = 0.7 \times \mu_{\text{obs}, \text{asym}}^{95\%CL}$.

1858 6. If $\mu_{+2\sigma}^{95\%CL} = \mu_{-2\sigma}^{95\%CL}$, set $\mu_{\pm 2\sigma}^{95\%CL} = \mu_{\pm 2\sigma, \text{asym}}^{95\%CL}$ instead.

1859 7. Scan over 100 equally spaced test values of μ between $\mu_{-2\sigma}^{95\%CL}$ and $\mu_{+2\sigma}^{95\%CL}$ and,
 1860 if $\mu > 0.0001$, calculate the CL_s p-value (p_μ) for this test value of μ to 10^{-6}
 1861 precision using a minimum of 500 toy experiments to generate $f(\tilde{q}_\mu|\mu, \hat{\theta}_\mu^{\text{obs}})$ and
 1862 $f(\tilde{q}_\mu|0, \hat{\theta}_0^{\text{obs}})$.

1863 8. Determine the observed ($\mu_{\text{obs}, \text{scan}}^{95\%CL}$), median expected ($\mu_{\text{exp}, \text{scan}}^{95\%CL}$), and $\pm 1\sigma$ ($\mu_{\pm 1\sigma, \text{scan}}^{95\%CL}$)
 1864 and $\pm 2\sigma$ ($\mu_{\pm 2\sigma, \text{scan}}^{95\%CL}$) expected CL_s limits from the scan p-values for the signal
 1865 + background and background-only pseudo-experiments.

1866 Finally, a particular GMSB model is excluded if the upper limit on the cross
 1867 section for that model is less than the expected theoretical cross section.

1868 5.3 Cross Section Upper Limits

1869 Figure 5.3 shows the observed upper limits on the cross sections for the models de-
 1870 scribed in Sec. 5.1. In some ($\mathcal{O}(10^{-3})$) cases, the upper limit is zero due to a com-
 1871 putational failure. The upper limit for these points is estimated from the average of the
 1872 upper limits of the four neighboring points, as shown in Figure 5.4. If any of the four
 1873 points is also missing a valid upper limit, it is dropped from the average. The errors

1874 on the individual upper limits used in the estimate are propagated to the error on
 1875 the average.

1876 5.4 Exclusion Contours

1877 Exclusion contours for the GMSB models discussed above are shown in Figure 5.5. The
 1878 contours are derived from plots of predicted cross section minus cross section upper
 1879 limit ($\sigma \times (1 - \mu^{95\%CL})$), where σ is the nominal value of the predicted cross section
 1880 for a given GMSB model) vs. the two model parameters of interest, so the values are
 1881 either negative (not excluded) or positive (excluded). Sometimes, a particular point
 1882 may have a different sign than its four same-sign neighbors (cf. Fig. 5.4) due to a
 1883 fluctuation. In these cases, $\sigma \times (1 - \mu^{95\%CL})$ for the anomalous point is estimated
 1884 as the average $\sigma \times (1 - \mu^{95\%CL})$ of the four neighboring points. The errors on the
 1885 individual values of $\sigma \times (1 - \mu^{95\%CL})$ used in the estimate are propagated to the error
 1886 on the average.

1887 In the plots in Fig. 5.5, the expected limit (i.e. the contour derived from $\sigma \times (1 -$
 1888 $\mu_{\text{exp,scan}}^{95\%CL})$) is drawn in dark orange and the 1σ experimental band around the expected
 1889 limit (i.e. the shaded region between the contours derived from $\sigma \times (1 - \mu_{\pm 1\sigma, \text{scan}}^{95\%CL})$) is
 1890 drawn in light orange. The values of $\mu_{\text{exp,scan}}^{95\%CL}$ and $\mu_{\pm 1\sigma, \text{scan}}^{95\%CL}$ only reflect the experimental
 1891 uncertainties given in Sec. 5.2.2.

1892 The observed limits (derived from $\sigma \times (1 - \mu_{\text{obs,scan}}^{95\%CL})$) and 1σ theoretical error
 1893 bands around the observed limits in Fig. 5.5 are drawn in blue. The contours that
 1894 define this band are derived from $\pm(\sigma_{\pm 1\sigma} - \sigma \mu_{\text{obs,scan}}^{95\%CL})$, where $\sigma_{\pm 1\sigma}$ is the nominal
 1895 value of the predicted cross section \pm the one-standard-deviation theoretical error on
 1896 the predicted cross section. In this way, the experimental and theoretical errors, the
 1897 latter due to imperfect knowledge of the predicted cross section, are shown separately.
 1898 Comparing with Fig. 5.1, one can easily see that the shapes of the exclusion curves

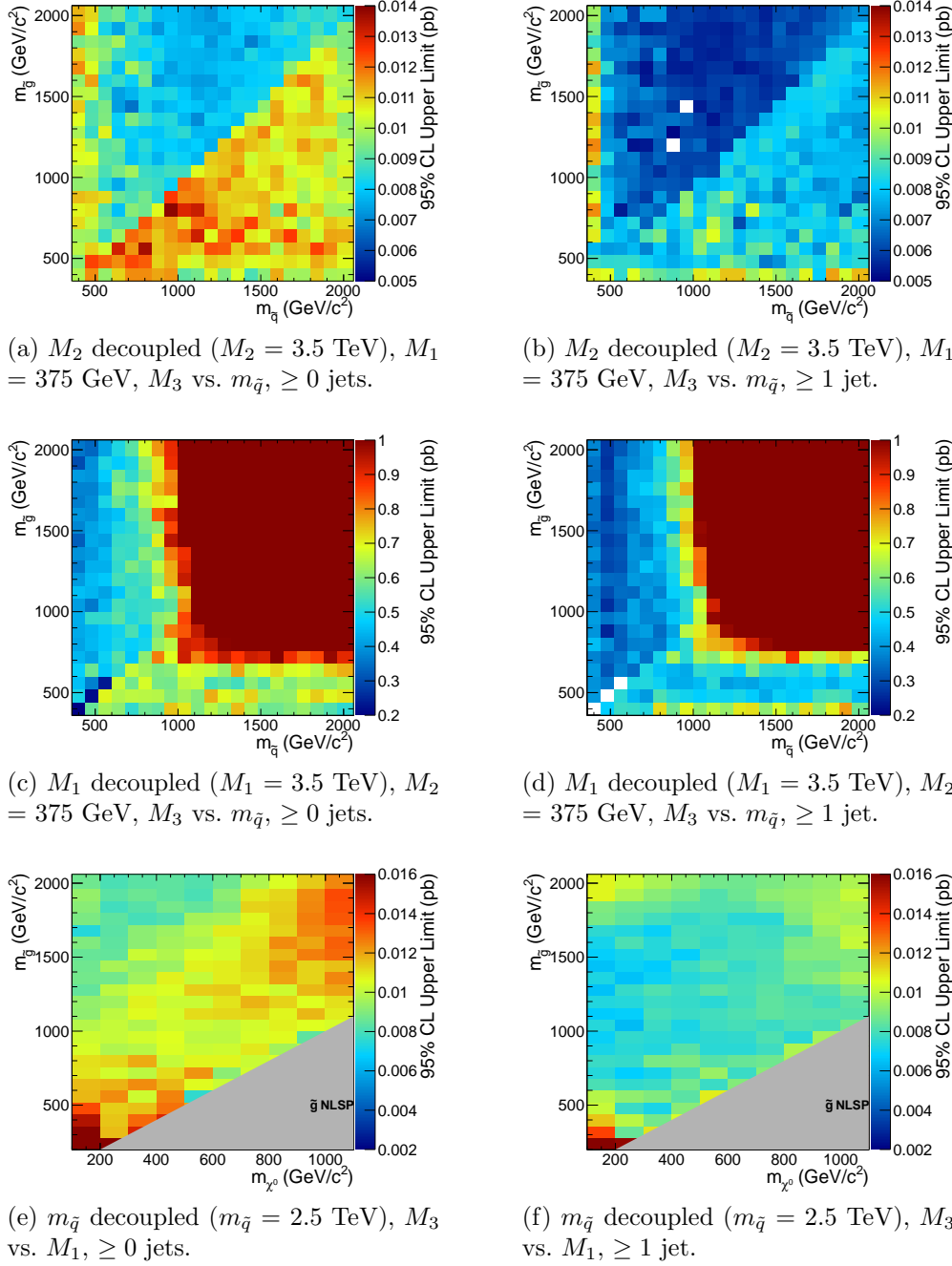


Figure 5.3: Cross section upper limits for the three different scenarios described in Sec. 5.1.

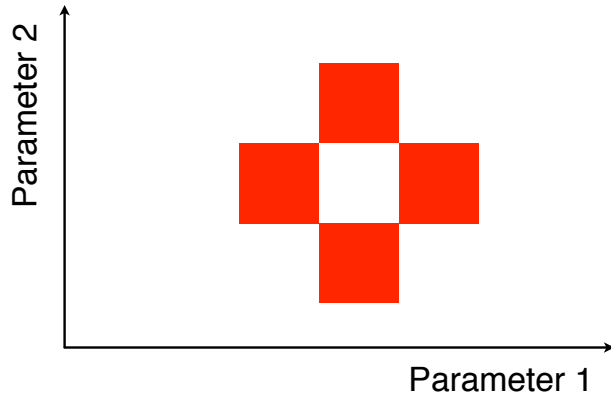


Figure 5.4: Diagram of the points (red squares) used in the estimation of an upper limit when a computational failure occurs (middle white square).

¹⁸⁹⁹ are driven by the contours in the expected cross section plane.

¹⁹⁰⁰ The dominant theoretical uncertainties on the GMSB cross sections are due to:

¹⁹⁰¹ • PDF uncertainty (4%-100% depending on model)

¹⁹⁰² • Renormalization scale uncertainty (0.036%-25% depending on model)

¹⁹⁰³ The PDF4LHC [95] recommendations are used to calculate the effect of these uncer-
¹⁹⁰⁴ tainties on the GMSB cross sections. The recommendations state that PDF sets from
¹⁹⁰⁵ MSTW08 [96], CTEQ6.6 [97], and NNPDF2.0 [98] should be considered in the deter-
¹⁹⁰⁶ mination of the PDF uncertainties, because these three PDF sets include constraints
¹⁹⁰⁷ from the Tevatron and from fixed target experiments, as well as from HERA [?], and
¹⁹⁰⁸ are thus the most complete.

¹⁹⁰⁹ Each collaboration's PDF prediction comes from a global fit to experimental data
¹⁹¹⁰ with a certain number of free parameters. The best fit parameters come from mini-
¹⁹¹¹ mizing the χ^2 ; increasing the χ^2 by one from its minimum can be written in terms of
¹⁹¹² the N -dimensional Hessian error matrix [?] where N is the number of free parameters.

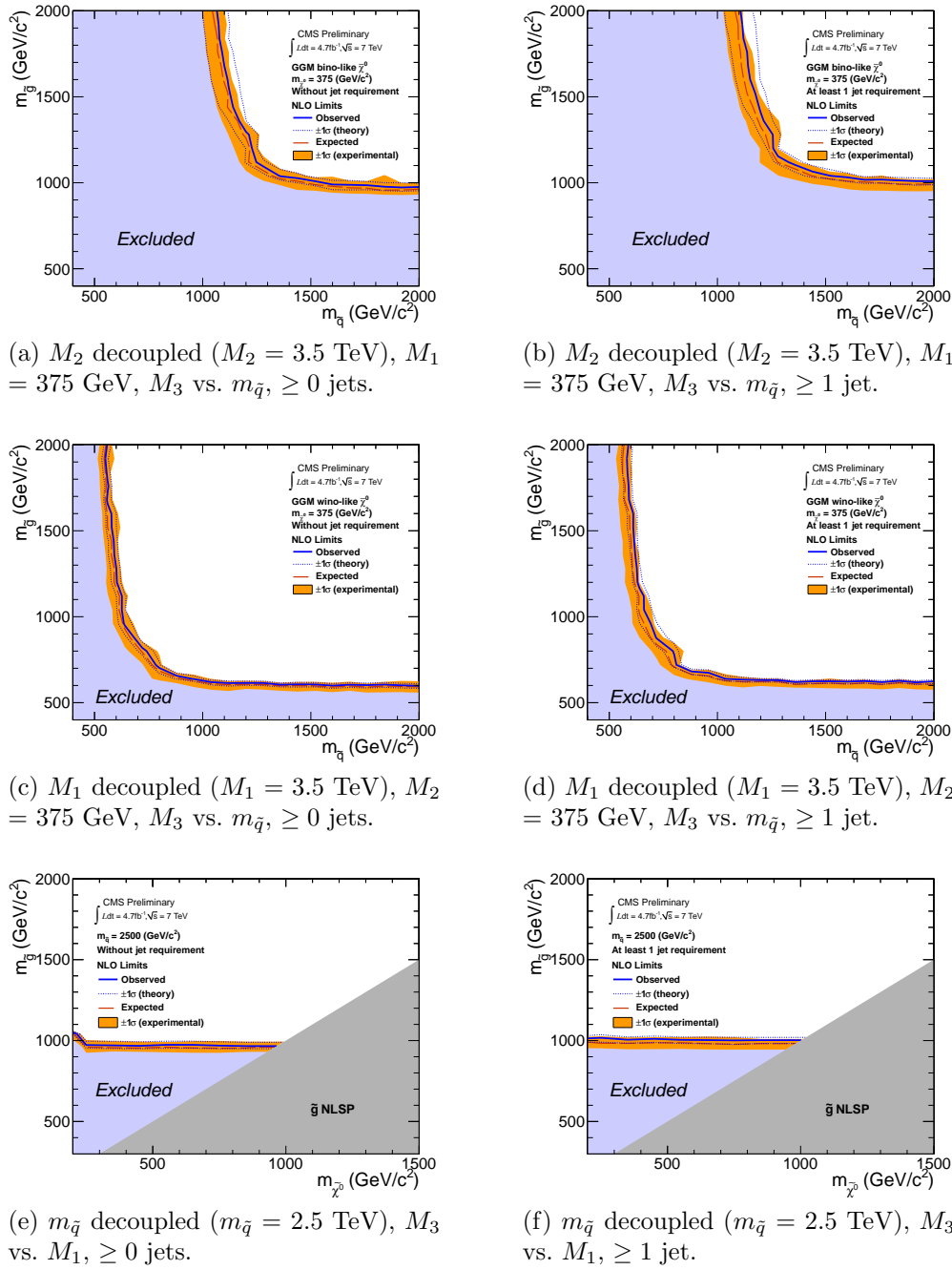


Figure 5.5: Exclusion contours for the three different scenarios described in Sec. 5.1.

1913 To form the i^{th} pair of members of the PDF set, the PDF is evaluated once at the
 1914 parameter values given by the i^{th} eigenvector of the Hessian matrix, and then again
 1915 at the parameter values given by the negative of the i^{th} eigenvector. Each PDF set
 1916 therefore contains $2N$ members, corresponding to the positive and negative values of
 1917 the N eigenvectors [99].

1918 To calculate the PDF uncertainties for a given GMSB model, the leading order
 1919 Pythia cross section is reweighted by a factor of the error PDF divided by the leading
 1920 order PDF with which the model was generated. This is repeated for each error PDF
 1921 in a given PDF set. The $\pm 1\sigma$ deviations are proportional to the maximum difference
 1922 between cross sections obtained this way. The actual equation for the $\pm 1\sigma$ errors is
 1923 Eq. (43) of ref. [99]. In the same way, the $\pm 1\sigma$ errors are calculated for the CTEQ6.6,
 1924 MSTW08, and NNPDF2.0 PDF sets. The total error is given by the half the difference
 1925 between the largest $+1\sigma$ deviation and the smallest -1σ deviation [95].

1926 The uncertainties on the signal cross sections due to the choice of renormaliza-
 1927 tion/factorization scale ($\alpha_S(M_Z)$) are evaluated by calculating the PROSPINO next
 1928 to leading order cross section once with $\alpha_S(M_Z)$ halved, then once with $\alpha_S(M_Z)$ dou-
 1929 bled. The lower error on the cross section is taken as the absolute difference between
 1930 the nominal and halved-scale values of the cross section, while the upper error is taken
 1931 as the absolute difference between the nominal and doubled-scale values. The PDF
 1932 and α_S uncertainties are added in quadrature to give the total PDF uncertainty.

1933 Note that the quoted GMSB cross sections are evaluated at next to leading order
 1934 using PROSPINO, but it is the leading order Pythia cross sections that are reweighted
 1935 to the next to leading order MSTW08, CTEQ6.6, and NNPDF2.0 PDFs to get the
 1936 error bands. In addition, since to a good approximation the GMSB production cross
 1937 sections for the M_3 - $m_{\tilde{q}}$ scans only depend on M_3 and $m_{\tilde{q}}$, the same PDF errors per
 1938 point are used for the \tilde{B} -like and \tilde{W} -like grids.

1939 **Appendix A**

1940 **Monte Carlo Samples**

1941 A number of MC samples are utilized in this analysis and referred to throughout the
1942 text. Below is a list of the MC samples used and an explanation of what the sample
1943 names mean.

1944 **A.0.1 List of Samples**

1945 1. Drell-Yan:

1946 /DYJetsToLL_TuneZ2_M-50_7TeV-madgraph-tauola/
1947 Fall11-PU_S6_START42_V14B-v1/AODSIM

1948 2. QCD enriched with B and D meson decays to electrons:

1949 /QCD_Pt-20to30_BCToE_TuneZ2_7TeV-pythia6/
1950 Fall11-PU_S6_START42_V14B-v1/AODSIM,
1951 /QCD_Pt-30to80_BCToE_TuneZ2_7TeV-pythia6/
1952 Fall11-PU_S6_START42_V14B-v1/AODSIM,
1953 /QCD_Pt-80to170_BCToE_TuneZ2_7TeV-pythia6/
1954 Fall11-PU_S6_START42_V14B-v1/AODSIM

1955 3. Photon + jet doubly enriched with jets passing an EM filter:

1956 /GJet_Pt-20_doubleEMEnriched_TuneZ2_7TeV-pythia6/
 1957 Fall11-PU_S6_START42_V14B-v1/AODSIM

1958 4. W leptonic decays:

1959 /WJetsToLNu_TuneZ2_7TeV-madgraph-tauola/
 1960 Fall11-PU_S6_START42_V14B-v1/AODSIM

1961 5. $t\bar{t}$:

1962 /TTJets_TuneZ2_7TeV-madgraph-tauola/
 1963 Fall11-PU_S6_START42_V14B-v2/AODSIM

1964 A.0.2 Explanation of Naming Conventions

1965 • L: charged lepton

1966 • B: B hadron

1967 • C: D , or charmed, hadron

1968 • E: electron or positron

1969 • G: photon

1970 • W: W boson

1971 • Nu: neutrino

1972 • T: top quark

1973 • TuneZ2: Pythia tune incorporating 2010 LHC data with CTEQ6L1 [97] PDFs
 1974 [104]

1975 • M-50: Generated l^+l^- invariant mass threshold of 50 GeV

1976 • 7TeV: Generated center-of-mass energy 7 TeV

- 1977 • **pythia6**: Parton showering and hadronization simulated with Pythia v6.424
- 1978 [105]
- 1979 • **madgraph**: Hard interaction generated with MadGraph [106]
- 1980 • **tauola**: τ decays generated with Tauola [107]
- 1981 • **PU_S6**: Generated with S6 pileup scenario
- 1982 • **START42_V14B**: Reconstructed with best alignment and calibration constants
- 1983 and magnetic field conditions as of August 3, 2011
- 1984 • **Pt_XtoY**: $X \leq$ generated $\hat{p}_T < Y$
- 1985 • **BCToE**: Enriched in B and D meson decays to electrons
- 1986 • **doubleEMEnriched**: Enriched in electromagnetic jets

1987 Bibliography

- 1988 [1] S.L. Glashow, J. Iliopoulos, and L. Maiani, *Phys. Rev. D* **2** (1970) 1285; S.L.
1989 Glashow, *Nucl. Phys.* **22(4)** (1961) 579; J. Goldstone, A. Salam, and S. Weinberg,
1990 *Phys. Rev.* **127** (1962) 965; S. Weinberg, *Phys. Rev. Lett.* **19** (1967) 1264; A.
1991 Salam and J.C. Ward, *Phys. Lett.* **13(2)** (1964) 168.
- 1992 [2] M. Gell-Mann, *Phys. Lett.* **8** (1964) 214; G. Zweig, *CERN 8419/TH. 412* (1964)
1993 (unpublished).
- 1994 [3] J. Drees, *Int. J. Mod. Phys.* **A17** (2002) 3259.
- 1995 [4] P.W. Higgs, *Phys. Lett.* **12(2)** (1964) 132; P.W. Higgs, *Phys. Rev. Lett.* **13** (1964)
1996 508; P.W. Higgs, *Phys. Rev.* **145** (1966) 1156.
- 1997 [5] I. Aitchison, *Supersymmetry in Particle Physics: An Elementary Introduction*
1998 (Cambridge University Press, Cambridge 2007), p. 4.
- 1999 [6] S. P. Martin, *A Supersymmetry Primer* **v4** (2006) 86. [arXiv:hep-ph/9709356](https://arxiv.org/abs/hep-ph/9709356).
- 2000 [7] M. Dine and W. Fischler, *Phys. Lett.* **B110** (1982) 227; C.R. Nappi and B.A.
2001 Ovrut, *Phys. Lett.* **B113** (1982) 175; L. Alvarez-Gaumé, M. Claudson, and M.B.
2002 Wise, *Nucl. Phys.* **B207** (1982) 96; M. Dine and A.E. Nelson, *Phys. Rev.* **D48**
2003 (1993) 1277; M. Dine, A.E. Nelson, and Y. Shirman, *Phys. Rev.* **D51** (1995)
2004 1362; M. Dine, A.E. Nelson, Y. Nir, and Y. Shirman, *Phys. Rev.* **D53** (1996)
2005 2658.

- 2006 [8] A.H. Chamseddine, R. Arnowitt, and P. Nath, *Phys. Rev. Lett.* **49** (1982) 970; R.
 2007 Barbieri, S. Ferrara, and C.A. Savoy, *Phys. Lett.* **B119** (1982) 343; L.E. Ibáñez,
 2008 *Phys. Lett.* **B118** (1982) 73; L.J. Hall, J.D. Lykken, and S. Weinberg, *Phys. Rev.*
 2009 **D27** (1983) 2359; N. Ohta, *Prog. Theor. Phys.* **70** (1983) 542; J. Ellis, D.V.
 2010 Nanopoulos, and K. Tamvakis, *Phys. Lett.* **B121** (1983) 123; L. Alvarez-Gaumé,
 2011 J. Polchinski, and M. Wise, *Nucl. Phys.* **B221** (1983) 495.
- 2012 [9] P. Meade, N. Seiberg, and D. Shih, *Progr. Theor. Phys. Suppl.* **177** (2009) 143.
- 2013 [10] G. Aad et al., *CERN-PH-EP-2011-160* (2011).
- 2014 [11] T. Aaltonen et al., *Phys. Rev. Lett.* **104** (2010) 011801.
- 2015 [12] CMS Collaboration, *CMS-PAS-SUS-11-009* (2011).
- 2016 [13] <http://en.wikipedia.org/wiki/Tevatron>.
- 2017 [14] E. Fernandez et al., *Phys. Rev. Lett.* **54** (1985) 1118; E. Fernandez et al., *Phys.*
 2018 *Rev.* **D35** (1987) 374; D. Decamp et al., *Phys. Lett.* **B237(2)** (1990) 291; F.
 2019 Abe et al., *Phys. Rev. Lett.* **75** (1995) 613; S. Abachi et al., *Phys. Rev. Lett.* **75**
 2020 (1995) 618; G. Alexander et al., *Phys. Lett.* **B377(4)** (1996) 273; S. Aid et al.,
 2021 *Z. Phys.* **C71(2)** (1996) 211; S. Aid et al., *Phys. Lett.* **B380(3-4)** (1996) 461; B.
 2022 Aubert et al., *Phys. Rev. Lett.* **95** (2005) 041802.
- 2023 [15] O. Buchmueller et al., *CERN-PH-TH/2011-220* (2011).
- 2024 [16] <https://twiki.cern.ch/twiki/bin/view/CMSPublic/PhysicsResultsSUS>.
- 2025 [17] G. Aad et al., *JINST* **3** (2008) S08003.
- 2026 [18] B.C. Allanach et al., *Eur. Phys. J.* **C25** (2002) 113.
- 2027 [19] CMS Collaboration, *CMS-PAS-SUS-12-001* (2012).

- 2028 [20] A. Boyarsky, J. Lesgourges, O. Ruchayskiy, and M. Viel, *CERN-PH-TH/2008-*
 2029 *234* (2009).
- 2030 [21] E. Komatsu et al., *Astrophys. J. Suppl. Ser.* **180** (2009) 330.
- 2031 [22] C.-H. Chen and J.F. Gunion, *Physical Review D***58** (1998) 075005.
- 2032 [23] F. Staub, W. Porod, J. Niemeyer, *JHEP* **1001** (2010) 058.
- 2033 [24] S. Chatrchyan et al. (CMS Collaboration), *JINST* **3** (2008) S08004.
- 2034 [25] G.L. Bayatian et al. (CMS Collaboration), *CERN/LHCC* **2006-001**, edited by
 2035 D. Acosta (2006).
- 2036 [26] M. Ivova, talk given at the Swiss Ph.D. School on Particle and Astroparticle
 2037 Physics (CHIPP), Monte Verita' (2010).
- 2038 [27] G. Bolla et al., *Nucl. Instr. Meth. Res.* **A461** (2001) 182.
- 2039 [28] https://twiki.cern.ch/twiki/pub/CMSPublic/DPGResultsTRK/_imgf9e0ee48ebca770d7774454532b4b4ee.png (2011).
- 2040 [29] https://twiki.cern.ch/twiki/pub/CMSPublic/DPGResultsTRK/_img7569b7652b3f7c15030a11a4223e631c.png (2011).
- 2041 [30] https://twiki.cern.ch/twiki/pub//CMSPublic/DPGResultsTRK/hv11_d1.png (2011).
- 2042 [31] https://twiki.cern.ch/twiki/pub/CMSPublic/DPGResultsTRK/_imga571742cbcd3a14a9e2581ae95efa54c.gif (2011).
- 2043 [32] <https://twiki.cern.ch/twiki/pub//CMSPublic/DPGResultsTRK/StripHitRes2.gif> (2011).

- 2049 [33] https://twiki.cern.ch/twiki/pub//CMSPublic/EcalDPGResults/histories2_laser.png (2012).
- 2050
- 2051 [34] https://twiki.cern.ch/twiki/pub//CMSPublic/EcalDPGResults/electronres_eb_inclusive.png (2012).
- 2052
- 2053 [35] https://twiki.cern.ch/twiki/pub//CMSPublic/EcalDPGResults/electronres_ee_inclusive.png (2012).
- 2054
- 2055 [36] <https://twiki.cern.ch/twiki/pub//CMSPublic/EcalDPGResults/seed-time.EEEE.png> (2012).
- 2056
- 2057 [37] N. Akchurin and R. Wigmans, *Rev. Sci. Instrum.* **74** (2003) 2955.
- 2058 [38] CMS Collaboration, *CMS-DP 2010-025* (2010).
- 2059 [39] https://twiki.cern.ch/twiki/pub/CMSPublic/PhysicsResultsMUO/dimuMass_2011Run_1fb_20July2011.pdf (2011).
- 2060
- 2061 [40] S. Chatrchyan et al. (CMS Collaboration), *JHEP* **4** (2012) 33.
- 2062 [41] W.H. Smith, P. Chumney, S. Dasu, F. Di Lodovico, M. Jaworski, J.R. Lackey, and P. Robl in *Proceedings of the 7th Workshop on Electronics for LHC Experiments, Stockholm, 2001*, edited by C. Isabella (CERN, Geneva, 2001), p. 238.
- 2063
- 2064
- 2065 [42] R. Brun and F. Rademakers, *Nucl. Inst. Meth. Res.* **A389** (1997) 81. See also <http://root.cern.ch/>.
- 2066
- 2067 [43] J. Gutleber and L. Orsini, *Cluster Comput.* **5** (2002) 55.
- 2068 [44] D. Box, D. Ehnebuske, G. Kakivaya, A. Layman, N. Mendelsohn, H.F. Nielsen, S. Thatte, and D. Winer, *W3C Note 08*, <http://www.w3.org/TR/2000/NOTE-SOAP-20000508/> (2000).
- 2069
- 2070

- 2071 [45] R. Arcidiacono et al., talk given at the 10th ICAL-EPCS International Conference
 2072 on Accelerator and Large Experiment Physics Control Systems, Geneva (2005).
- 2073 [46] J. Knobloch et al., *CERN-LHCC-2005-024* (2005).
- 2074 [47] R. Brunelière, *Nucl. Instr. Meth. Res. A***572** (2007) 33.
- 2075 [48] S. Chatrchyan et al. (CMS Collaboration), *JINST* **5** (2010) T03011.
- 2076 [49] CMS Collaboration, *CMS PAS EGM-10-002* (2010).
- 2077 [50] P. Meridiani and C. Seez, *CMS IN-2011/002* (2011).
- 2078 [51] P. Adzic et al. (CMS Electromagnetic Calorimeter Group), *Eur. Phys. J.* **C44S2**
 2079 (2006) 1.
- 2080 [52] P. Adzic et al. (CMS Electromagnetic Calorimeter Group), *JINST* **3** (2008)
 2081 P10007.
- 2082 [53] M. Malberti, *Nuc. Sci. Symposium Conference Record NSS/MIC IEEE* (2009)
 2083 2264.
- 2084 [54] S. Chatrchyan et al. (CMS Collaboration), *JINST* **5** (2010) T03010.
- 2085 [55] R. Paramatti, *J. Phys. Conf. Ser.* **293** (2011) 012045.
- 2086 [56] Y. Yang, [http://www.hep.caltech.edu/cms/posters/Pi0Poster_](http://www.hep.caltech.edu/cms/posters/Pi0Poster_CMSWeekDec2011.pdf)
 2087 CMSWeekDec2011.pdf (2011).
- 2088 [57] M. Anderson, A. Askew, A.F. Barfuss, D. Evans, F. Ferri, K. Kaadze, Y. Maravin,
 2089 P. Meridiani, and C. Seez, *CMS IN-2010/008* (2010).
- 2090 [58] <https://twiki.cern.ch/twiki/bin/view/CMS/ECALEnergyScaleCorrections>.
- 2091 [59] The H $\rightarrow \gamma\gamma$ working group, *CMS AN-2011/426* (2011).

- 2092 [60] M. Cacciari, *LPTHE-P06-04* (2006).
- 2093 [61] M. Cacciari, G.P. Salam, and G. Soyez, *CERN-PH-TH-2011-297* (2011).
- 2094 [62] S. Chatrchyan et al. (CMS Collaboration), *Phys. Rev. Lett.* **106** (2011) 082001.
- 2095 [63] A. Askew, B. Cox, D. Elvira, Y. Gershtein, M. Hildreth, D. Jang, Y.-F. Liu, D.
2096 Mason, D. Morse, U. Nauenberg, M. Paulini, R. Stringer, R. Yohay, and S.L.
2097 Zang, *CMS AN-2011/515* (2011).
- 2098 [64] F. Beaudette, D. Benedetti, P. Janot, and M. Pioppi, *CMS AN-2010/034* (2010).
- 2099 [65] M. Konecki, in Proceedings of the European Physical Society Europhysics Con-
2100 ference on High Energy Physics, Krakow, 2009, Eur. Phys.Soc. Mulhouse (ed.)
2101 (unpublished).
- 2102 [66] W. Adam, R. Früwirth, A. Strandlie, and T. Todorov, *J. Phys.* **G31** No. 9 (2005).
- 2103 [67] CMS Collaboration, *CMS PAS PFT-09-001* (2009).
- 2104 [68] CMS Collaboration, *CMS PAS PFT-10-002* (2010).
- 2105 [69] S. Chatrchyan et al., *JINST* **6** (2011) P11002.
- 2106 [70] CMS Collaboration, *CERN-PH-EP 2011-102* (2011).
- 2107 [71] M. Cacciari, G.P. Salam, and G. Soyez, *JHEP* **0804** (2008) 063.
- 2108 [72] G. Salam, talk given at CERN Theory Institute: SM and BSM Physics at the
2109 LHC (2009).
- 2110 [73] C.W. Fabjan and R. Wigmans, *Rep. Prog. Phys.* **52** (1989) 1519.
- 2111 [74] <http://www-cdf.fnal.gov/physics/new/top/2004/jets/cdfpublic.html>
2112 (visited on 16 January 2011).

- 2113 [75] S. Chatrchyan et al. (CMS Collaboration), *JINST* **6** (2011) P09001.
- 2114 [76] CMS Collaboration, *CMS PAS JME-09-002* (2009).
- 2115 [77] T. Sjöstrand, S. Mrenna, and P. Z. Skands, *Comput. Phys. Commun.* **178** (2008)
2116 852.
- 2117 [78] S. Chatrchyan et al. (CMS Collaboration), *JINST* **5** (2010) T03014.
- 2118 [79] J. P. Chou, S. Eno, S. Kunori, S. Sharma, and J. Wang, *CMS IN-2010/006*
2119 (2010).
- 2120 [80] Y. Chen, talk given at a meeting of the CMS JetMET group (2011).
- 2121 [81] R. Korzekwa et al., *iEEE Trans. Elec. Dev.* **38** (1991) 745.
- 2122 [82] W. Adam, Th. Speer, B. Mangano, and T.Todorov, *CMS NOTE* **2006/041**
2123 (2006).
- 2124 [83] G. Daskalakis, D. Evans, C.S. Hill, J. Jackson, P. Vanlaer, J. Berryhill, J. Haupt,
2125 D. Futyana, C. Seez, C. Timlin, and D. Wardrope, *CMS AN-2007/019* (2007).
- 2126 [84] F. James and M. Roos, *Comput. Phys. Commun.* **10** (1975) 343.
- 2127 [85] W. Verkerke and D.P. Kirkby, *CHEP-2003-MOLT007* (2003).
- 2128 [86] J.E. Gaiser, Ph.D. thesis, Stanford University (1982).
- 2129 [87] A. Askew, S. Arora, Y. Gershtein, S. Thomas, G. Hanson, R. Stringer, W. Flana-
2130 gan, B. Heyburn, U. Nauenberg, S.L. Zang, R. Nandi, D. Elvira, D. Mason, M.
2131 Balazs, B. Cox, B. Francis, A. Ledovskoy, and R. Yohay, *CMS AN* **2010/271**
2132 (2010).
- 2133 [88] Information about all CMS datasets is available from the CMS Data Aggregation
2134 System (DAS), located at the URL <https://cmsweb.cern.ch/das/>.

- 2135 [89] S. Chatrchyan et al., *Phys. Rev. Lett.* **106** (2011) 211802.
- 2136 [90] G. Aad et al. (ATLAS Collaboration), S. Chatrchyan et al. (CMS Collaboration),
2137 and LHC Higgs Combination Group, *CMS-NOTE-2011/005* (2011).
- 2138 [91] A.L. Read, in *Proceedings of the First Workshop on Confidence Limits, Geneva,*
2139 *2000*, edited by L. Lyons, Y. Perrin, and F.E. James (CERN, Geneva, 2000), p.
2140 81.
- 2141 [92] G. Cowan, K. Cranmer, E. Gross, and O. Vitells, *Eur. Phys. J.* **C71** (2011) 1554.
- 2142 [93] J. Neyman and E.S. Pearson, *Phil. Trans. R. Soc. Lond.* **A231** (1933) 289.
- 2143 [94] CMS Collaboration, *CMS PAS EWK-11-001* (2011).
- 2144 [95] S. Alekhin et al. (The PDF4LHC Working Group), arXiv:1101.0536 [hep-ph];
2145 M. Botje et al. (The PDF4LHC Working Group), arXiv:1101.0538 [hep-ph];
2146 <http://www.hep.ucl.ac.uk/pdf4lhc/index.html>.
- 2147 [96] A.D. Martin, W.J. Stirling, R.S. Thorne, and G. Watt, *Eur. Phys. J.* **C63** (2009)
2148 189.
- 2149 [97] P. M. Nadolsky, H.-L. Lai, Q.-H. Cao, J. Huston, J. Pumplin, D. Stump, W.-K.
2150 Tung, and C.-P. Yuan, *Phys. Rev.* **D78** (2008) 013004.
- 2151 [98] R.D. Ball, L. Del Debbio, S. Forte, A. Guffanti, J.I. Latorre, J. Rojo, and M.
2152 Ubiali, *Nucl. Phys.* **B838** (2010) 136.
- 2153 [99] J.M. Campbell, J.W. Huston, and W.J. Stirling, *Rep. Prog. Phys.* **70** (2007) 89.
- 2154 [100] A. Djouadi, J.-L. Kneur, G. Moultaka, arXiv:hep-ph/0211331 (2005).
- 2155 [101] M. Muhlleitner, A. Djouadi, Y. Mambrini, *Comput. Phys. Commun.* **168** (2005)
2156 46.

- ₂₁₅₇ [102] J. Allison et al., *IEEE Trans. Nucl. Sci.* **53**(1) (2006) 270.
- ₂₁₅₈ [103] W. Beenakker, R. Hoepker, M. Spira, [arXiv:hep-ph/9611232](https://arxiv.org/abs/hep-ph/9611232) (1996).
- ₂₁₅₉ [104] R. Field, talk given at LHC Physics Centre at CERN Minimum Bias and Un-
₂₁₆₀ derlying Event Working Group Meeting (2011).
- ₂₁₆₁ [105] T. Sjöstrand, S. Mrenna, and P. Z. Skands, *JHEP* **0605** (2006) 026.
- ₂₁₆₂ [106] dummy
- ₂₁₆₃ [107] dummy